Norwegian Meteorological Institute

MET report

no. 12/2013
Oceanography

BaSIC Technical Report No. 2:

Discussions and conclusions from the pre-production run

Lars Petter Røed, Nils Melsom Kristensen, Arne Melsom, Yvonne Gusdal
Jon Albretsen and Bjørn Ådlandsvik

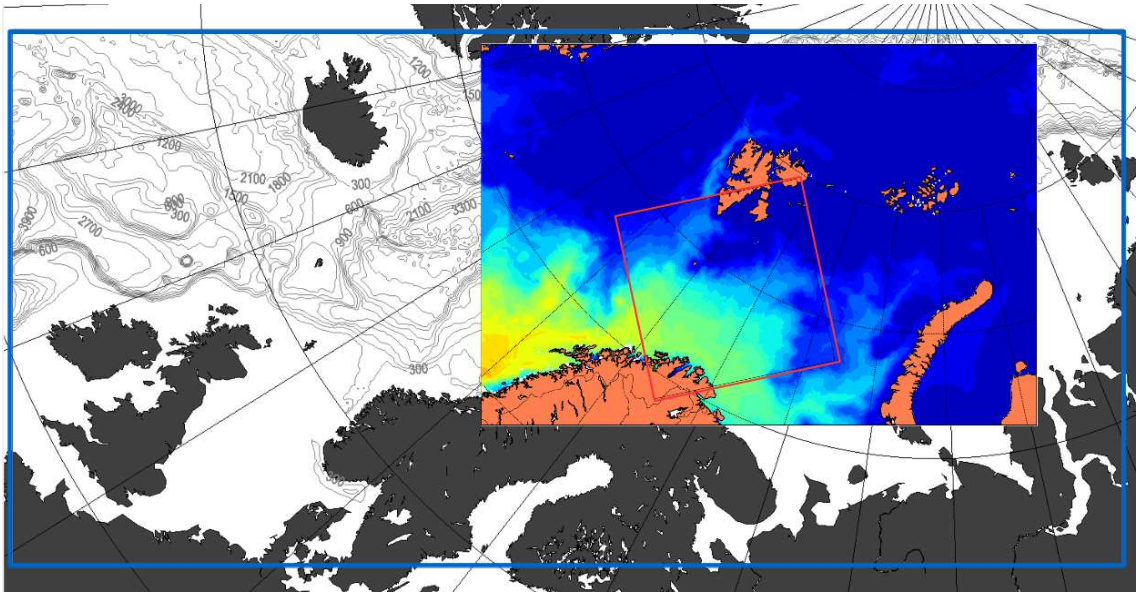

Norwegian Meteorological Institute

MET report

Title	Date
BaSIC Technical Report No. 2: Discussions and conclusions from the pre-production run	June 27, 2013
Section	**Report no.**
Ocean and Ice	12
Author(s)	**Classification**
Lars Petter Røed, Nils Melsom Kristensen, Arne Melsom, Yvonne Gusdal, Jon Albretsen and Bjørn Ådlandsvik	● Free ○ Restricted
Client(s)	**Client's reference**
Statoil	Contract: 4502465983

Abstract

A triply nested model grid configuration focusing on the Barents Sea is developed and run for two two-year long periods. The system is based on the Regional Ocean Model System- ROMS. The innermost child grid has a grid size of 800 m, the middle child 2 km and the parent 4 km (cf. front cover). The model results are evaluated by comparing them to current meter measurements along the Fugløya - Bjørnøya section, remotely sensed sea-ice data (satellite imagery), and a host of in situ CTD data (temperature and salinity). Conclusions are reached regarding how good the model reproduces reality and whether a grid size of 800 m really is needed to capture the mesoscale activity in the Barents Sea.

Keywords

Physical Oceanography, Numerical Modeling, Barents Sea, Sea-ice, Circulation

Disciplinary signature	Responsible signature
Lars Anders Breivik	Øystein Hov

Contents

Abstract

A triply nested model grid configuration focusing on the Barents Sea is developed and run for two two-year long periods. The system is based on the Regional Ocean Model System- ROMS. The innermost child grid has a grid size of 800 m, the middle child 2 km and the parent 4 km (cf. front cover). The model results are evaluated by comparing them to current meter measurements along the Fugløya - Bjørnøya section, remotely sensed sea-ice data (satellite imagery), and a host of in situ CTD data (temperature and salinity). Conclusions are reached regarding how good the model reproduces reality and whether a grid size of 800 m really is needed to capture the mesoscale activity in the Barents Sea.

Meteorologisk institutt
Meteorological Institute
Org.no 971274042
post@met.no

Oslo
P.O. Box 43 Blindern
0313 Oslo, Norway
T. +47 22 96 30 00

Bergen
Allégaten 70
5007 Bergen, Norway
T. +47 55 23 66 00

Tromsø
P.O. Box 6314
9293 Tromsø, Norway
T. +47 77 62 13 00

www.met.no
www.yr.no

1 Purpose and scope

1.1 Background

To prepare for eventual oil and gas exploration in the Kara and Barents Seas it is of general importance to get a good understanding of the environment. In particular, it is of interest to get knowledge of the meteorological and oceanographic variables such as winds, waves, water level (tidal height and storm surge), currents and ice conditions to design offshore structures that are both safe and cost efficient. This requires sufficiently accurate information about long-term cycles and trends of these variables. To this end long term records, say 25 to 50 years duration, are needed. A cost efficient means by which such time series can be provided is by performing long term hindcasts using numerical models. Such long time series have recently been established for atmospheric variables and waves through an earlier joint industry project (JIP) (*Reistad et al.*, 2009, 2011).

Record length may be less of an issue for currents and hydrography (temperature and salinity) than it is for wind and waves because they appear to have less significant year to year variations. On the other hand there is strong inter-annual and inter-decadal climatic variability in the Barents Sea region (*Kvingedal*, 2005), and there are indications that currents responds to these variations. Thus record lengths of at least 25 years or longer are required regarding currents and hydrography in the Barents Sea region. In addition, currents and hydrography have more significant spatial variations than wind and waves because extreme current events are associated with the oceanic "weather", that is, meandering eddies and jets of radii down to 10 kilometers and widths of only a few kilometers. Numerical circulation models of sufficient grid resolution can describe this variability. Hindcasts of currents and hydrography generated by such suitable models therefore yield estimates of extreme values for design of facilities, operating conditions, and local variations of currents and hydrography. Modeled currents and hydrography also give valuable input to measurement campaign strategy.

Ice occurs in most parts of the Barents Sea region. Currents are one of the biggest forces that move ice. High quality current and hydrography data for the entire region are therefore essential for the design of structures that can withstand icebergs, sea ice, and ice ridges. Operability and collision risk analyses must

therefore include modeled current data.

1.2 The BaSIC project

In the project BaSIC we aim to establish such long term time series of currents, hydrography, water level and sea-ice. In this we use the ocean circulation model ROMS[1]. It should be emphasized that since the spatial scale of the extreme current events are so small, and the significant variations in time are so long compared to wind and waves, the suitable ocean models for this purpose push the computers to their limits. Thus in developing a suitable grid configuration for the task at hand we have to balance the need to resolve the oceanic weather against the available computer power and storage capacity. We are therefore, even with todays supercomputers, basically required to decrease the geographical coverage when increasing the grid resolution. To maintain the larger scale patterns and variations the traditional solution is to embed or nest the models that do have a sufficient grid resolution, or so called eddy resolving models, into models of decreased grid resolution, ranging from eddy permitting to non-eddy resolving models. Commonly this is referred to as the downscaling approach (cf. Section 2.1 on page 4).

In BaSIC we use the downscaling approach involving three nested grids one embedded within the other (Figure 1 and front cover). Note that each successive grid has a higher resolution at the cost of covering a smaller domain. However, before embarking on a full multi-decadal production, we first ask two questions:

1. To what extent is the grid configuration used able to reproduce what is observed, or how accurate are the results?

2. What grid resolution is needed to get a handle on the spatial variations of currents?

To answer the first question we need to evaluate model results against observed currents and hydrography. To answer the second question we need to compare

[1]ROMS is a modern community ocean model developed recently by a consortium in the USA (*Shchepetkin and McWilliams*, 2005; *Haidvogel et al.*, 2008). It is also used by many European modeling communities. For instance is ROMS used as the operational ocean model at MET Norway and at IMR. As such it is the basis for all the ocean forecast products available through the web site yr (http://www.yr.no).

results from model various grid configuration for the same geographical area and then evaluate the results against available observations.

Thus BaSIC is split in two phases, a pre-production phase and a production phase. In the pre-production phase we perform a series of shorter term (mostly two-year) trial hindcasts using a triply nested grid configuration. By studying and evaluating the results we are in a position to extract some answers to the above two questions. In the second phase the required long term records of currents and hydrography as well as sea-ice and water level are eventually produced. Note that the second phase is only commenced if Statoil, based on the results of the pre-production phase, elect to continue with the production hindcast.

1.3 Work presented

Below we present and evaluate model results from the trial hindcasts using a triply nested grid configuration. We focus our evaluation on currents and hydrography, but also sea-ice and to some degree sea level anomalies are assessed.

Three two-year long trial hindcasts are prepared, but in time of writing only analyses of the first two, referred to as the Standard hindcast and EXP1 are available (cf. Table 1 on page 30). Note that the Standard hindcast is the only one of the three that so far includes the triply nested grid configuration to its full extent, that is, also includes the innermost, ultra-fine mesh model.

Observations available to us are currents meters records located at the Barents Sea opening, hydrographic data contained in the World Ocean Database *Boyer et al.* (2009), and sea-ice concentrations derived from satellite imagery through the OSI SAF project. We discuss the results and evaluate them by comparing them to measurements. The evaluation gives insight into the extent the model is indeed able to reproduce what is observed. Since we use a triply nested grid configuration with progressevely decreasing mesh size, that is, increasing resolution, we also get insight into what mesh size is required to resolve the smaller spatial scales of the currents, that is, eddies, instabilities and filaments.

1.4 Organization of report

In Section 2 we present the triply nested, grid configuration and give a brief overview of the variuos model versions of ROMS used for the three grids, while Section 3 offers a presentation of the results from the trial hindcast runs. It includes a comparison of the results from the various grid configurations, while the assessment of the model results agains observations follows in Section 5. Finally, in Section 6 we offer a summary and some concluding remarks.

2 The grid configuration and hindcasts performed

2.1 The downscaling approach

A multiple grid configuration, or nested model system, consists of multiple model grids embedded, or nested, one within the other. A common characteristic is that each successive grid, or child, has a higher resolution than its parent. This approach is referred to as downscaling. Downscaling is a one-way process, in that information is passed solely downstream from the parent to the child. Thus each parent grid configuration is run independent of its child, a procedure referred to as offline nesting. The outermost parent is run first and the results passed on to its child, and so on. The downscaling approach therefore yields realistic higher-resolution solutions permitting study of local problems associated with a particular area, e.g. the Barents Sea. The outermost parent provides the large-scale mean circulation and its associated variability, thatis, mesoscale, seasonal, inter-annual and inter-decadal contributions. This solution is then passed down to its children, which then generates the mesoscale to submesoscale circulation such as eddies, instabilities and filaments.

We emphasize that downscaling offers a practical solution to the problem of resolving wide-ranging spatial and temporal scales under the constraint of finite computing power and storage. Thus the increased resolution of the child is at the cost of the child's geographical coverage. We also note that the offline nesting is not a perfect solution. As a result of mismatches between the boundary forcing passed on from the parent and the evolving child solution false solutions may appear at the boundaries between the parent and child, sometimes referred to

as rim currents (*Mason et al.*, 2010). These rim currents may arise if there are differences between the parent and the child surface forcings, e.g., switching from one wind product to another, and also if volume conservation is not enforced in the boundary velocities.

An indication of a model grid's ability to capture the mesoscale and submesoscale circulation is often defined as the ratio of the twice the grid size to 2π times the Rossby radius of deformation. Thus if we let L_R denote the Rossby radius and let Δs denote the grid size then the resolution ratio, say R, is defined as $R = \Delta s/\pi L_R$. If $R > 1$ the model is commonly referred to as non-eddy resolving. For a model grid to be truly eddy-resolving $R \lesssim 0.1$. If $0.1 < R < 0.5$ the the model is referred to as an eddy-permitting model. Finally, if $0.5 < R < 1$ the model is sometimes referred to as eddy-recognizing.

2.2 The BaSIC triply nested grid configuration

To be in a position to possibly answer the two question asked in Section 1.2 we have used the downscaling approch. Consequently we use the triply nested grid configuration depicted in Figure 1. It is developed particularly for use in BaSIC, and consists of three grids one embedded within the other as shown. Each grid has a progressively increased resolution (smaller grid size) at the cost of a smaller geographical coverage. We note that it differs slightly from the one reported earlier (*Røed et al.*, 2013) as detailed in Section 2.2.2. The outermost parent model is henceforth referred to as SVIM4. The first child, or second parent, is referred to as BaSIC2, while the innermost child is referred to as BaSIC0.8.

We note that in the Barents Sea region the Rossby radius is in the range 5-10 km. Consequently, and with reference to the resolution ratio, a model that claims to be truly eddy-resolving for the whole area must employ a grid of size smaller than about 1-2 km.

All grids use versions of the Regional Ocean Model System - ROMS. The essential features and characteristics of the ROMS versions we use for the various grids, and the nesting conditions we use to pass on the results from the parent to the child, are described in detail in Section 3 of *Røed et al.* (2013). It is therefore not recapitulated in detail here. Nevertheless, a summary of the various model version's key characteristics is provided in Table 1 on page 30.

2.2.1 The SVIM4 grid

The geographical coverage of SVIM4 is outlined by the blue rectangle in Figure 1 and has a grid size of 4 km. We note that it covers the entire Nordic Seas including the Greenland, Iceland and Norwegian Seas as well as the adjacent Barents, Kara and North Seas.

We note that the resolution ratio is in the range $0.13 < R < 0.25$, and hence SVIM4 is eddy-permitting. Hence we do not expect SVIM4 to accurately reproduce the mesoscale to submesoscale circulation and the dynamic instabilities. However, we do expect SVIM4 to reproduce the temporal scales, ranging from weekly to inter-decadal variations, and the larger spatial scales and patterns, that is, scales on the order of the Rossby radius and larger. Moreover, once an eddy is formed we expect it to resolve it as well.

We emphasize that SVIM4 is run independently from its children. In fact a long term hindcast, covering the years 1958-2007, was derived prior to BaSIC within the SVIM[2] project funded by the Research Council of Norway. Within BaSIC the period was extended to cover also the years up to and incuding 2011. In addition we note that SVIM4 employs an earlier version of ROMS than its children.

2.2.2 The BaSIC2 grid

The colored area displayed in Figure 1 conforms to the BaSIC2 model grid, and shows its embedded orientation within its parent SVIM4 grid. Its topography is shown separately in Figure 2 on page 37. As is evident it covers the Barents Sea as well as parts of the Kara Sea. More importantly it includes a good portion of the areas west and north of the Svalbard Archipelago and Franz Josef Land, and areas well south of the Lofoten Archipelago. The major topographic features of the BaSIC2 area are the Mid-Atlantic Ridge, the steep shelf slope in the Lofoten area continuing northward toward's the Arctic Ocean, the Yermak Plateu north of Svalbard and the east-west oriented steep shelf slope north of Franz Josef Land. Worth mentioning is also the various banks in the Barents Sea itself.

As alluded to the geographical area covered by BaSIC2 is different from the one reported in *Røed et al.* (2013). The rationale is that the results of the test

[2]Spatiotemporal Variability In Mortality and growth of fish larvae and zooplankton in the Lofoten-Barents Sea ecosystem

hindcasts indicated that we needed to extend the area northwestward north of Svalbard to properly include the topography associated with the Yermak Plateu. Furthermore, the test cases also revealed that we needed to cover an extended area south of Lofoten so that the entire Lofoten Basin was covered within the BaSIC2 grid. Finally to balance the increased computer load of the extensions we decided to orient the grid to be parallell to the SVIM4 grid orientation, and to cut off the southeastern part of the Barents Sea. Thus the modified domain features an additional open boundary located in the southeastern part of the Barents Sea.

Finally we note that BaSIC2 grid has a mesh size of 2 km. Hence the resolution ratio is in the range $0.06 < R < 0.13$. Thus BaSIC2 is classified as an eddy-resolving model grid. We add that going from 4 to 2 km grid size entails a doubling of the resolution at the cost of a decrease in the geographical area covered compared to SVIM4 area. Moreover, doubling the grid resolution roughly implies a factor of 8 (=2^3) increase in computer time for the same geographical area. Similarly another doubling would mean a factor of 64 (=4^3) increase in computer time. This nicely illustrates why we have to balance resolution against computer power and storage, and why we have to use the downscaling approach.

2.2.3 The BaSIC0.8 grid

The BaSIC0.8 grid is the innermost child. Its orientation and position within the BaSIC2 grid is nicely illustrated in Figure 1 by the red square. As is evident it is the smallest of the three grids in geographical terms. It stretches from Nordkapp to the tip of Spitsbergen, and covers the central Barents Sea including the Barents Sea opening and Bear Island. Its grid size is 0.8 km (800 m), that is, a factor of 2.5 increase in resolution compared to the BaSIC2 grid. Despite this increase the differences in the topography between the BaSIC2 grid (Figure 2) and that of the BaSIC0.8 grid (Figure 2) are almost negligible.

Regarding the resolution ratio we observe that the 2.5 increase in grid resolution entails that the resolution ratio for the BaSIC0.8 grid is in the range $0.03 < R < 0.05$, and hence that the BaSIC0.8 model grid is truly eddy resolving, but again at the cost of a much smaller geographical area covered. We also note that decreasing the grid size form 2 km to 0.8 km gives a factor of $15.5 = 2.5^3$) increase in computer time and storage.

One of the guidelines when choosing the BaSIC0.8 grid domain is to cover areas where measurements of currents are available to us. Thus it includes the two main sections traversed by IMR each year, namely the Fugløya - Bjørnøya section and the Vardø- Nord section, as well as the fixed current meter moorings along the Fugløya - Bjørnøya section (Figure 31 on page 66). As expected we note that the only differences between the topographies are associated with some finer structures as we increase the resolution (decreases the mesh size). The larger scale topography patterns remain the same.

2.3 Trial hindcasts

To possibly answer the two questions asked in Section 1.2 we have targeted three trial hindcasts as outlined Table 1 on page 30. The abbreviation used are STD (Standard hindcast), EXP1 and EXP2. At the time of writing two trial hindcasts are completed (STD and EXP1) while EXP2 is in the pipeline.

We note that while the STD hindcast is for the period 2000-2001, the EXP1 hindcast is for the two years 2010 and 2011. These latter years were chosen since we would like to to cover a time slice somewhat separated from the STD hindcast to assess whether there are any substantial differences between the two two-year time slices. At the same time we would like to cover a period for which current measurements from Skrugard oil field was available. Since the hindcast of the parent grid SVIM4 covers the period 1958-2011 we were in parctice limited to the two years 2010 and 2011. Thus EXP1 covers two and a half months of the period for which current measurements are available from the Skrugard oil field. The main difference between the Standard and EXP1 hindcasts is therefore the atmospheric forcing. It may be used to reveal if trends in the observations are also picked up by the hindcasts. The third trial hindcast, EXP2, is a rerun for the Standard period, but employing a different parameterization of the vertical mixing. The rationale of EXP2 is to assess to what degree the vertical mixing impacts the tendency of the models to have a cold bias, a tendency revealed by the evaluation of the Standard and EXP1 hindcasts (cf. Section 5).

We note that the ROMS model version we use for the BaSIC2 and BaSIC0.8 grids is version 3.5 of the so called "Kate branch". An outline of this version is found in *Røed et al.* (2013). As alluded to the SVIM4 grid was decided in an

earlier project. Hence a slightly earlier model version of ROMS, namely version 3.2 of the "Kate branch", is used.

Note that of the three runs only the standard experiment, utilizes the full triply nested grid configuration. The remaining two are with a doubly nested grid configuration only, that is, with the BaSIC2 grid as the only child of the SVIM4 parent. The rationale is that the BaSIC0.8 model nested into BaSIC2 provided results similar to the BaSIC2model.

3 Results

All the results shown below are based on output in the form of daily means. Thus tidal fluctuations are mostly filtered out, although not completely due aliasing. The results are shown as two-yearly means, yearly means and 30 day (monthly) means. The latter is mostly used for time series, while yearly and tw-yearly means are mostly used for fields. Also most of the time series are shown as spatial means over the BaSIC2 area and BaSIC0.8, respectively. Besides showing results in term of individual variables (currents, temperature, salinity, sea ice and sea level), we also include derived variables such as kinetic energy (mean and eddy) and relative vorticity. The latter often reveals mismathces on the boundaries between parent and child (cf. Section 2.1).

3.1 Currents

3.1.1 Yearly means

We start by showing the yearly mean surface currents from the year 2000 STD hindcast as displayed in Figure 3 on page 38. We note that the most of the currents in the BaSIC2 grid, shown in the upper panel, are about 10 cms^{-1} or smaller, but more eyecatching are the many distinct bands or filaments of enhanced currents. These structures conform with common knowledge. For instance we recognize the Norwegian Coastal Current (NCC) south of Lofoten veering off to form the band of strong currents, about 50 cms^{-1}, along the shelf break west of Lofoten. North of Lofoten it splits up into two bands, one following the Norwegian coast into the Barents Sea and the other continuing along the shelbreak toward's

Svalbard. Along the west coast of Svalbard we recognize the well known West Spitsbergen Current (WSC). We also note the eastward directed filaments of enhanced currents along the shelf break north of Frans Josef's land towards Svalbard, and the complex current structures around the Yermak Plateau north of Svalbard. Finally we note the southward directed band of enhanced currents along the Mid Atlantic Ridge, and along the shelf break east of Greenland known as the East Greenland Current (EGC). Finally we observe the filament of strong, norhtward's directed currents along the west coast of Nova Zemlya, and the enhanced currents around Bear Island. The latter are probabaly due to strong tides in the area.

We note with particular interest the strong anticyclonic eddy off Lofoten located approximately at 69.5^{o}N, 9^{o}E clearly visible even in the yearly mean. A similar eddy is also seen further west in the Lofoten Basin at approximately 69.5^{o}N, 4^{o}N. This area is well known for its many eddies both from observations (e.g., *Koszalka and LaCasce*, 2010; *Koszalka et al.*, 2011) and from modeling (e.g., *Köhl*, 2007; *Røed and Kristensen*, 2013), and was noted by *Røed and Kristensen* (2010) in their report from the LOVECUR project.

Looking at the yearly mean surface currents from the year 2001, as depicted in Figure 4 on page 39, we recognize many of the same structures. The main differences are found in the eddy area off Lofoten, in that the eddies are there, but located in slightly other positions. This is in line with the observations reported in *Koszalka et al.* (2011). Finally, we note with satisfaction that the latter enhanced currents are replicated in the BaSIC0.8 grid. In particular we notice the currents around Bear Island, and the currents into the Barents Sea along the Norwegian coast, that is, the continuation of the NCC into the Barents Sea.

3.1.2 Vorticity

Another way of studying the current patterns is by calculating the relative vorticity. In Figures 6 through 9 on pages 41 through 44 we have chosen to calculate the relative vorticity of the depth integrated current, that is,

$$\omega = \mathbf{k} \cdot \nabla \times \hat{\mathbf{u}}, \tag{1}$$

where $\hat{\mathbf{u}}$ is the depth integrated current. We immediately recognize that the relative vorticity is enhanced along the current filaments shown in Figures 3 through

5. The relative vorticity, however, more clearly reveals the many smaller scale eddy structures of less enhanced currents that are not so easily detected in pictures of the yearly mean currents.

The relative vorticity is also better in detecting rim currents (cf. Section 2.1), that is, mismatches at the boundaries between the parent and the child due to the downscaling approach. For this purpose we have plotted the relative vorticity from the BaSIC0.8 grid superimposed on the relative vorticity of the BaSIC2 grid (Figure 9 on page 44). As is evident the nesting works, but there are also clear signs of mismatches along the boundaries. We note that these mismatches are not necessarily a failure of the boundary condition used in the downscaling approach. In the one-way nesting used here the parent solution is not aware of the child solution. Thus mismatches are to be expected, particularly at regions of outflow conditions since the child can resolve eddy scales that are unresolved by the parent leading to unavoidable differences at the boundaries.

3.1.3 Energetics

To get an indication of how much we gain by downscaling from SVIM4 (4 km grid size) to the child BaSIC2 (2 km grid size) and then to the innermost child grid BaSIC0.8 (800 m grid size), we calculate the mean (MKE) and eddy (EKE) kinetic energy. In this we follow *Røed* (1999) and derive MKE from the formula

$$MKE = \frac{1}{2}\overline{\mathbf{u}}^2, \tag{2}$$

where $\mathbf{u}$ is the horizontal velocity component. The overline indicates a time average in which the average period is longer than the typical eddy temporal scale (commonly 30 days or longer), so that the deviation of the current from the mean, say $\mathbf{u}' = \mathbf{u} - \overline{\mathbf{u}}$ is associated with the eddy motion, and such that $\overline{\mathbf{u}'} = 0$. Thus MKE is the kinetic energy associated with the mean motion. We also note that MKE differs from the average kinetic energy defined by

$$AKE = \frac{1}{2}\overline{\mathbf{u}^2}. \tag{3}$$

Since $\overline{\mathbf{u}'} = 0$ we may therefore calculate the EKE simply by the formula (*Røed*, 1999)

$$EKE = AKE - MKE = \frac{1}{2}\overline{\mathbf{u}'^2}. \tag{4}$$

The EKE is thus the energy associated with the eddy motion, and as such is a measure of the variability of the currents.

We have calculated depth integrated MKE and EKE based on current fields from the SVIM4, BaSIC2 and BaSIC0.8 grids for a domain encompassing the BaSIC0.8 grid both for the STD case and the EXP1 case, as presented in Figures 10 through 15. Regarding the STD hindcast the plotted domain includes the area from Lofoten to the central Barents Sea and the southern part of Spitsbergen as depicted in Figure 10 on page 45, while a slighly differnt plotting area is chosen for EXP1 (Figure 14) covering most of the BaSIC2 grid. The fields are averaged over the entire two years STD and EXP1 trial hindcast periods, respectively. We observe that the pattern of enhanced MKE in all grids are very much in line with the filaments and bands of enhanced currents shown in Figures 3 and 4, and thus the three grids at first glance appears to produce a similar pattern for all three model grids. However, on close inspection we observe major differences in the eddy area off Lofoten and into the Lofoten Basin between them and from year to year. However, a more detailed picture is depicted in the BaSIC0.8 model grid than the BaSIC2 model grid, and further, the MKE pattern in SVIM4 model grid is even smoother.

Of particular interest is that the large eddy in the Lofoten Basin described above (cf. Section 3.1.1) is more evident in the BaSIC2 model grid than in the SVIM4 model grid. Although this is considered a mesoscale phenomenon that should be regarded as eddy motion, its occurrence in the model is persistent enough to generate a clear pattern in the MKE.

The EKE maps are shown in Figure 11, and for all models the highest values of EKE are associated with the main current systems, i.e., the North Atlantic Current, the Norwegian Coastal Current and the Bear Island Current. Then, within the BaSIC0.8 domain the patterns and values of both MKE and EKE are comparable between the three models. We also see this in the spatial averaged time series of MKE and EKE for an area that is limited to the extension of the BaSIC0.8 grid (cf. Figure 12). All three models show comparable magnitude in kinetic energy, although BaSIC0.8 indicate about 10% higher MKE than SVIM4 and BaSIC2 most of the period. We also note that this area encompassing the Barents Sea opening almost misses the seasonal signal in MKE. The time evolution in EKE shows a much stronger seasonal signal with the highest values during winter.

When comparing the time evolution of the spatial averaged kinetic energy for the area identical to the BaSIC2 grid, we see a clear seasonal signal in both MKE and EKE (cf. Figure 13). In addition, covering a larger part of the NAC, we discover that both MKE and EKE increase by around 15 and 30%, respectively, when moving from a 4 to 2km grid.

Interestingly we do see an apperant increase in the EKE as we move from the parent grid SVIM4 to its children BaSIC2 and BaSIC0.8, although the MKE is more or less the same in the three models.

3.2 Temperature and salinity

3.2.1 Yearly means

Similar picture are also derived showing yearly mean sea surface temperature (SST) from the STD hindcast (Figures 16 and 17 on page 51 and 52 respectively), and from the EXP1 hindcast (Figure 18 on page 53).

As is evident from these figures there are only small changes in the yearly mean SST from year 2000 to year 2001. However, we note that the SST appears to be slightly warmer along the shelf break toward's Svalbard and in the West Spitsbergen Current (WSC) and slightly cooler in the southeastern Barents Sea in year 2001 compared to 2000. This is also true when when looking at year 2010 compared to 2011 (Figure 18). Thus it may appear that the BaSIC2 model is still in a kind of spin-up when doing two-year time slices. When comapring the two two-year time slices though, it appears that there is cooling trend.

We also nopte that these remarks are valid when inspecting the similar solutions with regard to salinity (Figures 19 - 21 on page 54 - 56).

3.3 Sea ice and water level

We also present sea ice concentration (SIC) and sea ice thickness (SIT) results in a similar manner as depicted in Figures 22 - 27 on page 57 - 62. Finally, we present results in terms of sea surface anomaly in Figures 28 - 30 on page 63 - 65.

4 Observations

4.1 Currents

The applied current meter data are hourly measurements from the Fugløya-Bjørnøya section, located at the western entrance to the Barents Sea (IMR data, *Ingvaldsen et al.* (2004)). The observation sites, labeled CM1, CM2, CM3, CM4 and CM5, are depicted in Figure 31. The data set covers the period August 1997 to December 2011 and is applied to study all hindcast experiments. A second data set (SKG1, SKG2 and SKG3), covering the period October 2011 to December 2012, is applied to validate the last three months of the EXP1 hindcast trial. The hindcasted model results are in terms of daily means of direction and speed. To fascilitate a model-observation comparison we have therefore first averaged the hourly current meter measurements to obtain daily mean values. We then compare them with the hindcasted daily averages corresponding to the date, location and depth of the current meter data.

For each observation site, measurements from 50m depth are used to examine the modeled velocity fields. In addition, at station CM1, CM2, CM3, CM4, CM5, SKG1, SKG2 and SKG3 bottom currents are validated at 212m, 310m, 373m, 401m and 464m, 393m, 344m and 374m, respectively. Note that at CM2, CM5, SKG1 and SKG2 the model depths are shallower than the current meter data. Here we simply use the deepest model result in the evaluation. For each position, we calculate current roses for direction and speed in addition to frequency diagrams (PDFs) of the *difference* between hindcasted and observed current speed. The results are shown in Figure 32 - 40.

4.2 Hydrography

The hydrography data we have used are extracted from the World Ocean Database 2009 (WOD09) (*Boyer et al.*, 2009). WOD09 includes all the IMR data, as well as additional data from other sources as detailed in *Boyer et al.* (2009). After its release in 2009, WOD09 are updated with profile data from 2010–2012. However, the most recent data that have been included in WOD09 from the BaSIC2 domain are from 2010.

Data in WOD09 have been subjected to a rigorous quality control, which includes data range checks, excessive gradient checks, checks of duplicity of reported profiles, and depth inversion checks. For the present analysis, no data which were flagged by any of the quality control procedures have been used.

WOD09 contains data which have been recorded by various instruments: the database includes Conductivity-Temperature-Depth (CTD) data, Expendable Bathythermograph data, data from profiling floats and data from gliders. Here, we restrict the analysis to include CTD data only.

The Standard hindcast is for the two year period 2000-2001. During this period, a total of 3,664 CTD profiles are available from the BaSIC2 domain. Nearly exactly half of these (1,834) are also inside the BaSIC0.8 domain. A total of 1,183 CTD profiles are available from 2010, i.e., during the EXP1 hindcast. There were 468 profiles available from the BaSIC0.8 domain during 2010. Details are provided in Table 3. Note that the vertical resolution of the data varies between profiles.

The target region in the present study is the Barents Sea. The SVIM4 model and the BaSIC2 model both cover the entire Barents Sea. Hence, result from these simulations will be compared with the observations from the Barents Sea subdomain. The Barents Sea region is displayed in blue in Figure 41.

4.3 Sea ice

Sea ice concentration observations are available form the Ocean and Sea Ice Satellite Application Facility (OSI-SAF) High Latitude Processing Center. The observations are derived from Special Sensor Microwave/Imager (SSM/I) data, and have been gridded onto a polar stereographic projection with a horizontal resolution of 10 km. Details about the data processing are given by *Andersen et al.* (2012) and *Eastwood et al.* (2011).

Sea ice concentrations have been interpolated/extrapolated onto regions where observations have originally been discarded due to cloud contamination. Thus, daily sea ice concentration values that covers the present model domain are available for the Standard hindcast experiment period[3].

[3]Due to operational issues, no SSM/I observations exist for the northern hemisphere from 2000-12-01, so this day is discarded from the analysis.

The present analysis takes advantage of a product that is post-processed so that the masking is time-invariant. Unfortunately, this product is not yet available for years later than 2009.

5 Analysis

Hereafter we will compare the model results from the trial hindcasts to observations. Since the model simulations are pure hindcasts no data assimilation is applied. Thus the focus is on the working of each of the models in the triply nested model grid configuration.

It should be emphasized that because of time constraints model results from the EXP2 hindcast are not available yet, and hence no analyses of these results are presented. Also EXP1 was late in its completion, and hence the analysis of these results are more rudimentary.

We focus on a *statistical* comparison, as we find this as the most sensible approach when performing the evaluation. In this we use probability distribution function (pdf) for offsets between model results and observations as exemplified in Figure 42 on page 77. The function values have been normalized by computing n_i/N where n_i is the count of occurrences inside an interval Δ_i, and N is the total sample size.

5.1 Currents

5.1.1 Standard hindcast trials 2000 - 2001

The Fugløya-Bjørnøya section covers the core of Atlantic inflow. This inflow is most evident at the two "inner" stations CM1 and CM2 both at the surface and at the bottom (Figures 32 on page 67 and 33 on page 68). At the northmost station CM5 there is a clear tendency for the polar water to leave the Barents Sea through the opening south of Bear Island at the bottom, while at the surface it is more variable in direction. At the two stations CM3 and CM4, located in a more flat terrain (Figure 31), the currents appears to be more variable in direction. In particular this is true at the surface, but for CM4 this also seems to be true for the bottom measurements. This is more or less reflected by the hindcasted results in

all model grids at station CM1, and also at station CM2 for the higher resolution model grids BaSIC2 and BaSIC0.8. Here the hindcasted currents from SVIM4 tends to be slightly offset to be more eastward than observed.

At station CM3, CM4 and CM5 the currents at 50m are more or less dominated by frequent variation in current direction. Also the modeled hindcast results, clearly describes the inflow of Atlantic Water at the inner stations. However, the currents are mainly aligned with the topography, especially in the co-located SVIM4 currents. BaSIC2 and BaSIC0.8 are eddy resolving model grids and are expected to provide a more comprehensive picture of the currents. This appears to be true, except at station CM5 where BaSIC2 and BaSIC0.8 gives a clear south-westerly current where the Arctic water is leaving the Barents sea. This is not seen in the observations at 50m depth. Examining similar results for the bottom depths (Figure 33), the distribution is very much alike the 50m current direction, except at station CM3 and CM5. At station CM5, the outflow of Arctic Water is more clearly seen in the current meter data. At station CM3, the observed velocity filed is dominated by a west/east current direction. We are not sure if this is an artifact in the dataset or a description of the actual current directions. However, it seems like BaSIC2 and BaSIC0.8 are more dominated by east/west current directions than SVIM4 at station CM3.

In Figure 34 on page 69, examining the difference between observed and co-located model velocities, all three model grids hindcast has lower current speeds than observed at the offshore stations CM3 - CM5. This is particularly seen in the BaSIC0.8 results showing a reduction in mean speed compared to SVIM4 and BaSIC2. At the inner stations CM1 and CM2, the three hindcast simulations behaves more or less in the same manner, but with an overestimation of the mean speed. Comparing the three models, we find BaSIC2 do give a better description of the observed currents than SVIM4 and BaSIC0.8.

5.1.2 EXP1 hindcast 2010 - 2011

Figure 35 and 36 on page 71 depicts the same plots as shown in Figure 32 and 33, but for the period 2010 - 2011. The results are more or less the same as shown for the standard hindcast trial over the period 2000 - 2001. However, by examining the current speed, BaSIC2 appears to underestimate the current

speeds even more than over the period 2000 - 2001. This can also be seen by the frequency diagrams in Figure 37 on page 72, showing the difference in current speed between the models and observation. From these results we can clearly see a reduction in velocity in BaSIC2 compared to SVIM4.

5.1.3 Skrugard

The Skrugard observation sites are located a few kilometers east of station CM3. The Atlantic inflow is clearly seen at all three stations at the surface and at the bottom (Figure 38 and 39 on pages 73 and 74, respectively). At the surface, the inflow is dominated by south-eastward flows, while at the bottom the direction is more north-east. Since the Skrugard period only covers the winter months October to December 2011, the overall current velocity is higher than seen in previous plots. Also the SVIM4 hindcast results, clearly describes the Atlantic inflow, but is more eastward at the surface than observed. The BaSIC2 hindcast results are also showing the inflow of Atlantic water at the surface but is more dominated by frequent variation in current direction. At the bottom SVIM4 has a fairly well description of the currents, but BaSIC2 tends to have a bigger offset with more west/east current than observed and is more variable in direction. In Figure 40, examining the difference between observed an co-located model velocities, both models simulates lower current speeds than observed at all stations from surface to bottom. This is particularly seen in the BaSIC2 results. For this comparison, we find SVIM to give a better description of the observed currents than BaSIC2.

5.2 Temperature and salinity

5.2.1 Integral properties

We start the analysis of model results for temperature and salinity by comparing vertical mean values from CTD profile observations and the various models. As described in Section 4.2, a total of 4,847 CTD profiles are available for this purpose.

The biases[4] and standard deviations for temperature and salinity are listed in

[4]Biases are overall differences between model results and observations, which are positive when the model value is larger than the observation.

Table 4 on page 32. Note that these results are not necessarily representative statistics for the model fields, since the observational data are irregular in time and space.

From the results listed in Table 4, we note that the BaSIC2 and SVIM4 results from the Standard hindcast experiement are quite similar, although the standard deviation in model-observation differences for salinity are somewhat larger for the BaSIC2 model. The SVIM4 results for temperature for the EXP1 hindcast are slightly closer to observations than the BaSIC2 model.

The BaSIC0.8 results for salinity are similar to the other two models. However, BaSIC0.8 is substantially colder then both of the other simulations.

5.2.2 Distribution

In order to examine the origin of the biases and the differences between the models in some detail, we first investigate the distribution properties based on the observations and the results from the three simulations. The normalized probability distribution function (pdf) for offsets between model results and observations are displayed in Figure 42.

The pdfs for temperature differences based on model-observations offset from BaSIC2 and the corresponding pdf from SVIM4 for the Standard hindcast are similar, although the BaSIC2 pdf is shifted slightly toward's negative values. The pdf for temperature differences based on results from BaSIC0.8 has a low peak value, and also quite large probabilities for offset in the range -2 - -6 K.

The corresponding pdfs for the EXP1 hindcast reveal that while the differences in the SVIM4 case are somewhat more constrained near a small negative bias, while the pdf for differences based on the BaSIC2 results is shifted towards lower values when compared to the Standard hindcast.

The pdfs for salinity differences from the Standard hindcast are similar. Further, due to the skewness of the pdf, all difference distributions peak at negative offsets even though the bias values in Table 4 are all positive, albeit very small.

The correponding pdfs for salinity differences from the EXP1 hindcast is again indicative of similar quality in the SVIM4 and the BaSIC2 models.

The scatter plots for temperature, Figure 43, reveal that the main discrepancy which leads to the cold bias, occurs for intermediate temperatures in the saltiest

(Atlantic) water. Moreover, the BaSIC0.8 results are generally shifted downward, i.e., the increasing cold bias is observed in all water masses.

From Table 4, we note that there is an increased cold bias in BaSIC2 from the Standard hindcast to the EXP1 hindcast. This is manifested by a shift towards larger discrepancies for warm and salty water masses (right panels in Figure 43 and Figure 44). We also note that more of the saltiest ($S > 35.1$) water masses were sampled in 2010 than during 2000-2001. However, this change has not lead to a change in the bias for the BaSIC2 model, and the contrasts between the experiments that were small during the Standard hindcast experiment (top row panels in Figure 43) become pronounces during the EXP1 hindcast experiement (Figure 44).

The results for salinity are fairly similar between the models, so in Figure 45, only the depiction of the scatter diagram for the SVIM4 *vs.* observations is shown. We note that in the majority of the profiles, the observed salinity is higher than 34.9. For this water mass, the model results exhibit a negative (fresh) offset. However, as revealed in Table 4, there is an overall positive (salty) bias in the simulations. This is due to the much larger discrepancies for water masses with low salinity. Thus, the differences in the salinity between the various water masses is underestimated in the simulations.

Temperature-salinity diagrams from the Standard hindcast experiment are displayed in Figure 46. Note that as the BaSIC2 results are very similar to SVIM4, they are omitted. The lack of model profiles with salinities above 35 is again notable, as well as the cold bias in BaSIC0.8. While the densities are in general reproduced well by the models, the lightest water masses are somewhat too dense.

5.2.3 Spatial variability

Next we examine the spatial properties of the validation of model results. In the depictions here we plot full circles on maps, positioned at the locations from which observations were available. The circle area is scaled by the number of available observations in the corresponding BaSIC0.8 grid cell. We restrict this presentation to the BaSIC0.8 model domain.

In all Standard hindcast simulations, the cold anomaly in the Norwegian Sea

is reduced inside the Barents Sea (Figure 47). In SVIM4, the model/observation differences are not of a clear sign in the central Barents Sea. BaSIC0.8 appears to be more or less uniformely colder in space when compared to the other two model grids.

From Figure 48, for the Standard hindcast, we observe that all models have a salt bias in the regions of coastal water in the south, and polar water in the northern Barents Sea. Further, the waters that have its origin in the Norwegian Atlantic Current have a negative (fresh) bias. Hence, the horizontal salinity gradients are underestimated in the model results. This is in line with other results presented above, e.g., the relatively flat salinity distribution that is apparent in Figure 45.

The results for salinity is similar in all three models and both hindcast experiments. The only general diffreence is that, in the nort-western Barents Sea, the offsets from observed salinities are somewhat larger for BaSIC0.8 and BaSIC2 results than for results from SVIM4.

The differences in the domain-wide temperature and salinity biases from the upper 100 m to the water masses below, are given in Table 5, for the Standard hindcast experiment and from the EXP1 hindcast.

Since the ocean is generally warmer near the surface than at depth, one may be tempted to conclude from these results that the colder bias in the lower waters corresponds to larger vertical temperature gradients. However, a closer examination reveals that this is not the case: there is a regional warm bias in the polar waters in the north-western Barents Sea. In a large part of this region, the ocean depth is $\lesssim 100$ m, and there is consequently no contribution here to the 100-500 m/bottom bias. Also, we find that the vertical temperature gradient in the Vardø-North section along the 31°E meridian is smaller in the model than in the observations.

Furthermore, since the ocean generally becomes saltier with increasing depth in the present region, the vertical salinity gradient is somewhat underestimated in all models. We can thus conclude that the stratification in the model results is too low. This is most likely due to too intense vertical mixing in the simulations.

5.2.4 Temporal variability

Due to the limited simulation period, it is difficult to evaluate the model performance with respect to temporal variability. Nevertheless, by inspecting how the temperature varies over a period of one year, some relevant statistics can be produced.

We restrict ourselves to observations in the BaSIC0.8 domain. Furthermore, we require that observations for the same BaSIC2 grid cell is available for the same month in different years, and that neither the uppermost observation level nor the lowermost level changes by $>$10 m.

First consider the changes from 2000 to 2001. There are a total of 275 pairs of observations that satisfy the criteria listed above. We examine the confusion matrix for cases where the observations and model results became colder and warmer from 2000 to 2001. The results from this analysis is presented in Table 6**a**.

If the model results and observations were uncorrelated, the probability of arriving at the distribution, or larger assymetry, between diagonal and off-diagonal elements in Table 6**a** is $<$6% in the case of SVIM4 results, and $\lesssim$0.2% for the BaSIC2 and BaSIC0.8 results. Hence, we conclude that it is very likely that the models have skill in reproducing changes from 2000 to 2001.

We find that there is a slight cooling trend from 2000 to 2001 in the observations. The cooling trend is stronger in all models when compared to the observed trend. Once more, results from BaSIC2 and SVIM4 are of similar quality. While the observed cooling trend appears to be captured slightly more precisely in the SVIM4, the accuracy as given by the percent of correct changes is somewhat higher in BaSIC2.

The large over-representation of the cooling trend in BaSIC0.8 suggests that the cold bias revealed by e.g. Table 4 is an evolving feature, indicating that BaSIC0.8 temperatures take at least some months to stabilize.

Next, consider the changes from 2000/2001 to 2010. Here, common grids, months were identified by looping through the 2010 observations, and searching for a match in the 2000-2001 period. If multiple matching profiles are found, data from the first (in time) are used. We find a total of 164 pairs of observations by this method. The results for the warmer/colder confusion matrix are given in Table 6**b**.

The probability of arriving randomly at the distribution, or larger assymetry,

between diagonal and off-diagonal elements in Table 6**b** is $<$4% in the case of SVIM4 results, *i.e.*, about the same as for the changes reported for Table 6**a**. However, the corresponding probability for the BaSIC2 results become vastly inflated, to 30%. Thus, the results for SVIM4 appear to be robust, while changes in the BaSIC2 results depends significantly on the period under consideration.

We find no significant warming (or cooling) trend from 2000/2001 to 2010 in the observations. The SVIM4 results exhibit a similar evolution, while there is a significant cooling trend in the BaSIC2 results.

The two BaSIC2 experiments were initialized by SVIM4 results on 200-01-01 and 2010-01-01, respectively. Hence, the trend in between the experiment periods is described by the SVIM4 model only. It is therefor difficult to attribute the differences in the results for temporal variability in the BaSIC2 model to a particular cause.

5.3 Sea ice

5.3.1 Integral properties

When examining sea ice results, we project all results on the coarsest resolution, which is here the 10 km grid of the OSI-SAF product.

Next, we set the sea ice concentration (SIC) at the ice edge to be SIC_{edge}=0.15, and define the gridded ice edge as the grid cells where SIC $> SIC_{edge}$, and which has at least one neighbor node where SIC $< SIC_{edge}$. The resulting root-mean-square position offsets between the observed ice edge and the models' ice edges are given in Table 7.

The full time series of differences in the Barents Sea domain exhibited very noisy behavior during the summer months. This is mostly due to sporadic occurrence of a sea ice edge near Novaya Zemlya. When this took place in either the model or the observations, but not in both, the RMS distance soared to 200-400 km. We decided to ignore these events in the present analysis. This was accomplished by disregarding days when the length of either sea ice edge in the Barents Sea dropped beneath 100 grid cells, which occurs during summer only.

We find that, while all models give results for the ice edge that are of similar quality, SVIM4 results are somewhat closer to the observations than the results from the other two models.

Next, we examine the sea ice area and the sea ice extent. The sea ice area is defined as the integral of the SIC (multiplied by the area), while the sea ice extent is the area where the SIC exceeds the limit that defines the ice edge.

As revealed by the results from the model-observation comparisons of sea ice area and sea ice extent in Table 8, the two-year averages of these quantities are captured well by all models. While results are somewhat improved by BaSIC0.8 in the BaSIC0.8-domain, the BaSIC2 results for the Barents Sea domain are convincing. And in the Barents Sea domain, the observed quantities are reproduced nearly flawlessly by SVIM4.

5.3.2 Distribution

Table 9 reveals that the main shortcoming of the model results for SIC is a problem related to correctly describe low SIC values. The models have about 5% of the region covered with the 0-4% SIC category, and around 60% is covered with the 4-10% category. The distribution between these two categories is reversed in the observations.

Otherwise, the simulations perform well, with higher values along the diagonal and in near-diagonal elements in the matrix than in the elements that are further off the diagonal. The category which corresponds to a near-continous ice cover (80-100%) occupies 12-16% of the region in the various models, and 12% of the area in the observational product.

5.3.3 Temporal variability

Finally, we examine the temporal evolution of sea ice in the observations and in the model results. We restrict this presentation to results for the domain of the BaSIC0.8 grid, but the results from BaSIC2 and SVIM4 in the Barents Sea region are analogous to our findings below.

Unsurprisingly, all models describe the seasonal cycle very well. A more detailed examination bolsters our conclusion that the model reproduce the temporal variability of sea ice area and extent: The shorter duration and higher values for sea ice maximum in 2001 compared to 2000 is reproduced well by the models. The episodic maximum in November 2001 observations does not have a counterpart in the observations from November 2000. This contrasting evolution during

the freezing season is reproduced well by the models. Similar high-frequency variability in observations and models is also seen during other episodes.

The only significant shortcoming is that the sea ice area and extent during the melting season of 2001 is over-estimated by the models. It is particularly BaSIC2 which exhibits a delayed melting during spring and summer of 2001.

6 Summary and conclusions

As part of the project BaSIC we have run three trial hindcasts using the multiple grid configuration shown in Figure 1. We note that each successive grid, or child, has a higher resolution than its parent. This approach is commonly referred to as downscaling. We emphasize that downscaling offers a practical solution to the problem of resolving wide-ranging spatial and temporal scales under the constraint of finite computing power and storage.

The three grids are SVIM4, BaSIC2 and BaSIC0.8. SVIM4 is the outermost parent and has a grid size of 4 km. The next, BaSIC2, has a grid size of 2 km, while the innermost child, BaSIC0.8, has a grid size of 0.8 km. Dynamically this entails that SVIM4 is eddy permitting, BaSIC2 is about eddy resolving while BaSIC0.8 is a true eddy resolving model grid. Each grid is run independently and the information passed on to its child. We note that it is impossible to obtain a perfect solution, in that there will always be small mismatches between the parent and child solution at the boundary between the two (*Mason et al.*, 2010). This is particularly important to keep in mind when when analysing results from long-term hindcasts longer than two years).

Regarding currents there it appears that results from the BaSIC2 child grid yields the best results overall. We are however puzzled by the results when comparing currents from the BaSIC2 grid with the observations at Skrugard (Section 5.1.3).

Regarding hydrography we note that the BaSIC2 and SVIM4 results from the STD hindcast experiment are quite similar, although the standard deviation in model-observation differences for salinity are somewhat larger for the BaSIC2 model. The SVIM4 results for temperature for the EXP1 hindcast are slightly closer to observations than the BaSIC2 model. The BaSIC0.8 results for salinity

are similar to the other two models. However, we note that BaSIC0.8 is substantially colder then both of the other two. Although the densities are in general reproduced well by the models, the lightest water masses are somewhat too dense.

We also find there is a regional warm bias in the polar waters in the northwestern Barents Sea. In a large part of this region, the ocean depth is $\lesssim 100$ m, and there is consequently no contribution here to the 100-500 m/bottom bias. Also, we find that the vertical temperature gradient in the Vardø-North section along the 31°E meridian is smaller in the model than in the observations. Furthermore, since the ocean generally becomes saltier with increasing depth in the present region, the vertical salinity gradient is somewhat underestimated in all models. We can thus conclude that the stratification in the model results is too low. This is most likely due to too intense vertical mixing in the hindcasts. We note that because of this fact we are now performing and EXP2 hindcast with a different vertical mixing parameterization, and thus we will come back to the stratifaction issue.

We find no significant warming (or cooling) trend from 2000/2001 to 2010 in the observations. The SVIM4 results exhibit a similar evolution, while there is a significant cooling trend in the BaSIC2 results. The two BaSIC2 experiments were initialized by SVIM4 results on 200-01-01 and 2010-01-01, respectively. Hence, the trend in between the experiment periods is described by the SVIM4 model only. It is therefore difficult to attribute the differences in the results for temporal variability in the BaSIC2 model to a particular cause at this stage.

Regarding sea ice the two-year averages of these quantities are captured well by all models. While results are somewhat improved by BaSIC0.8 in the BaSIC0.8-domain, the BaSIC2 results for the Barents Sea domain are convincing. And in the Barents Sea domain, the observed quantities are reproduced nearly flawlessly by SVIM4. Unsurprisingly, all models describe the seasonal cycle of sea ice very well. This fact is underscored by a more detailed examination in that the shorter duration and higher values for sea ice maximum in 2001 compared to 2000 is reproduced well by the models. The models also capture well high-frequency variability in observations.

The analyses made also gives some insight into the answer to the questions posed in the inroductory section. To address the first question to which extent the grid configuration is able to reproduce what is observed we find that the models

in terms of currents, hydrography and sea ice perform reasonably well, but that BaSIC2 fairs better than BaSIC0.8.

To address the second question of what resolution is needed to capture the variability in the currents the analyses so far indicate that there is very little to gain in going from the BaSIC2 model grid to the ultra-fine BaSIC0.8 grid.

Finally we note that more analyses are underway, which may or may not support these conclusions. It should also be emphasized that the trial hindcast are for two year time slices only, and that there are indications that the BaSIC2 and BaSIC0.8 models may not have enough time to stabilize from the initial conditions given to them by their parent SVIM4 model.

Acknowledgement

Acknowledgment

This research was supported by Statoil Petroleum AS, Contract No. 4502465983, the Institute of Marine Research, Norway and the Norwegian Meteorological Institute. Most of the SVIM4 hindcast was performed under grant 196685/S40 from the Norwegian Research Council. All the computations were performed at the Norwegian Supercomputer facilities (the computers Vilje and Hexagon).

References

Andersen, S., L.-A. Breivik, S. Eastwood, and et al. (2012), OSI SAF Sea Ice Product Manual, *Tech. Rep. SAF/OSI/met.no/TEC/MA/125*, EUMETSAT OSI SAF - Ocean and Sea Ice Satellite Application Facility.

Boyer, T. P., J. I. Antonov, O. K. Baranova, H. E. Garcia, D. R. Johnson, R. A. Locarnini, A. V. Mishonov, T. D. OBrien, D. Seidov, I. V. Smolyar, and M. M. Zweng (2009), World Ocean Database, NOAA Atlas NESDIS 66 - U.S. Gov. Printing Office - Wash. - D.C. - 216 pp., DVDs.

Eastwood, S., K. R. Larsen, T. Lavergne, E. Nielsen, and R. Tonboe (2011), OSI SAF Global Sea Ice Concentration Reprocessing, User Manual, *Tech.*

Rep. SAF/OSI/met.no/TEC/MA/138, EUMETSAT OSI SAF - Ocean and Sea Ice Satellite Application Facility.

Haidvogel, D. B., H. Arango, P. W. Budgell, B. D. Cornuelle, E. Curchitser, E. D. Lorenzo, K. Fennel, W. R. Geyer, A. J. Hermann, L. Lanerolle, J. Levin, J. C. McWilliams, A. J. Miller, A. M. Moore, T. M. Powell, A. F. Shchepetkin, C. R. Sherwood, R. P. Signell, J. C. Warner, and J. Wilkin (2008), Ocean forecasting in terrain-following coordinates: Formulation and skill assessment of the regional ocean modeling system, *J. Comput. Phys.*, *227*(7), 3595–3624, doi: http://dx.doi.org/10.1016/j.jcp.2007.06.016.

Ingvaldsen, R. B., L. Asplin, and H. Loeng (2004), Velocity field of the western entrance to the Barents Sea, *J. Geophys. Res.*, *109*, doi:10.1029/2003JC001811.

Köhl, A. (2007), Generation and stability of a quasi-permanent vortex in the Lofoten Basin, *J. Phys. Oceanogr.*, *37*, 2637–2651, doi:10.1175/2007/JPO3694.1.

Koszalka, I. M., and J. H. LaCasce (2010), Lagrangian analysis by clustering, *Ocean Dyn.*, *60*, 957–972, doi:10.1007/s10236-010-0306-2.

Koszalka, I. M., J. H. LaCasce, M. Andersson, K. A. Orvik, and C. Mauritzen (2011), Surface circulation in the Nordic Seas from clustered drifters, *Deep Sea Res. I*, *58(4)*, 468–485, doi:10.1016/j.dsr.2011.01.007.

Kvingedal, B. (2005), Sea-ice extent and variability in the Nordic Seas, 1967-2002, in *The Nordic Seas: An Integrated Perspective, Geophysical Monograph Series Vol. 158*, edited by H. Drange, T. Dokken, T. Furevik, R. Gerdes, and W. Berger, American Geophysical Union, Washington, DC.

Large, W. G., J. C. McWilliams, and S. C. Doney (1994), Oceanic vertical mixing: A review and a model with a vertical k-profile boundary layer parameterization., *Rev. Geophys.*, *32*, 363–403.

Mason, E., J. Molemaker, A. F. Shchepetkin, F. Colas, and J. McWilliams (2010), Procedures for offline grid nesting in regional ocean models, *Ocean Mod.*, *35*, 1–15, doi:10.1016/j.ocemod.2010.05.007.

Reistad, M., Ø. Breivik, H. Haakenstad, O. J. Aarnes, and B. R. Furevik (2009), A high-resolution hindcast of wind and waves for the North Sea, the Norwegian

Sea and the Barents Sea, *met.no Report 14/2009*, Norwegian Meteorological Institute, Postboks 43 Blindern, N-0313 Oslo, Norway.

Reistad, M., Ø. Breivik, H. Haakenstad, O. J. Aarnes, B. Furevik, and J.-R. Bidlot (2011), A high-resolution hindcast of wind and waves for the north sea, the norwegian sea, and the barents sea, *J. Geophys. Res.*, *116*(C5), n/a–n/a, doi: 10.1029/2010JC006402.

Røed, L. P. (1999), A pointwise energy diagnostic scheme for multilayer, non-isopycnic, primitive equation ocean models, *Mon. Weath. Rev.*, *127*, 1897–1911.

Røed, L. P., and N. M. Kristensen (2010), LOVECUR Final Report: Description of model and discussion of the model results, *met.no Report 21/2010*, Norwegian Meteorological Institute, P.O. Box 43 Blindern, 0313 Oslo, Norway, [Available at http://met.no/Forskning/Publikasjoner/Publikasjoner_2010/].

Røed, L. P., and N. M. Kristensen (2013), Eddy generation and cross shelf mixing off Lofoten, Norway, *Manuscript in preparation*.

Røed, L. P., N. M. Kristensen, J. Albretsen, and B. Ådlandsvik (2013), BaSIC Technical Report no. 1: The triply nested model system, *met.no Report 1/2013*, Norwegian Meteorological Institute, Postboks 43 Blindern, N-0313 Oslo, Norway.

Shchepetkin, A. F., and J. C. McWilliams (2005), The Regional Ocean Modeling System (ROMS): A split-explicit, free-surface, topography-following coordinate ocean model, *Ocean Modelling*, *9*, 347–404.

Umlauf, L., and H. Burchard (2003), A generic length-scale equation for geophysical turbulence models, *J. Marine Res.*, *61*, 235–265.

7 Tables

Table 1: Trial hindcasts performed

Trial hindcast	Period covered	No. of grids	Vertical mixing scheme[1,2] SVIM4	BaSIC2	BaSIC0.8
STD	2000/2001	3	GLS	GLS	GLS
EXP1	2010/2011	2	GLS	GLS	-
EXP2	2000/2001	2	GLS	KPP	-

[1]GLS: General Length Scale (*Umlauf and Burchard*, 2003)

[2]KPP: K-Profile Parameterization (*Large et al.*, 1994)

Table 2: Brief summary of model facts

Item	Model grid SVIM4	BaSIC2	BaSIC0.8
ROMS version no.	3.2	3.5	3.5
Grid size	4 km	2 km	0.8 km
No. vertical levels	35	35	35

	2000		2001		2010	
	BaSIC2	BaSIC0.8	BaSIC2	BaSIC0.8	BaSIC2	BaSIC0.8
Jan-Mar	357	198	493	263	328	145
Apr-Jun	454	144	583	110	223	40
Jul-Sep	885	637	604	406	551	249
Oct-Dec	84	28	204	48	81	34

Table 3: Number of available CTD profiles during the experiments, as a function of model domain, year and quarter.

	Standard hindcast				**EXP1 hindcast (2010 only)**			
	Temperature		**Salinity**		**Temperature**		**Salinity**	
	Bias	St.d.	Bias	St.d.	Bias	St.d.	Bias	St.d.
Region: *BaSIC2*								
BaSIC2	-1.0	1.4	0.05	0.37	-1.3	1.3	0.07	0.35
SVIM4	-0.9	1.4	0.06	0.31	-0.9	1.2	0.07	0.29
Region: *Barents Sea*								
BaSIC2	-0.4	0.8	0.01	0.22	-1.1	1.0	-0.00	0.20
SVIM4	-0.4	0.8	0.01	0.18	-0.6	0.6	-0.02	0.13
Region: *BaSIC0.8*								
BaSIC0.8	-1.6	1.4	0.01	0.21				
BaSIC2	-1.0	1.2	0.02	0.25	-1.3	1.0	-0.04	0.21
SVIM4	-0.8	1.2	0.01	0.19	-0.9	0.9	-0.05	0.13

Table 4: Bias and standard deviation of the experiment results, for potential temperature and salinity. Results are for the upper 500 m of the water column (surface to bottom in regions where the ocean depth is $<$500 m). The *BaSIC2* and the *BaSIC0.8* domains correspond to the full simulation domains, while the *Barents Sea* domain in displayed in Figure 41.

	Temperature		**Salinity**	
	0-100 m	100-500 m/btm	0-100 m	100-500 m/btm
Standard hindcast Region: *BaSIC0.8*				
BaSIC0.8	-1.4	-1.7	0.02	-0.09
BaSIC2	-0.8	-1.2	0.01	-0.09
SVIM4	-0.7	-0.9	0.04	-0.08
EXP1 hindcast (2010 only) Region: *BaSIC0.8*				
BaSIC2	-1.3	-1.6	-0.02	-0.12
SVIM4	-0.9	-1.0	-0.02	-0.10

Table 5: Temperature and salinity biases from the Standard hindcast experiment. Results have been calculated for the depth range from the surface to the 100 m level, and between 100 m and 500 m (to the bottom in regions where the ocean depth is $<$500 m).

a. From 2000 to 2001		Observations colder	Observations warmer	Model sum
BaSIC0.8	colder	0.50	0.35	0.85
	warmer	0.05	0.09	0.15
BaSIC2	colder	0.41	0.27	0.68
	warmer	0.14	0.18	0.32
SVIM4	colder	0.37	0.26	0.63
	warmer	0.19	0.18	0.37
Observations	sum	0.55	0.45	1.00

b. From 2000/1 to 2010		Observations colder	Observations warmer	Model sum
BaSIC2	colder	0.37	0.35	0.72
	warmer	0.12	0.16	0.28
SVIM4	colder	0.30	0.24	0.55
	warmer	0.18	0.27	0.45
Observations	sum	0.49	0.51	1.00

Table 6: Relative frequency of occurrence for local change in temperature. **a.** from 2000 to 2001, **b.** from 2000/2001 to 2010. See the text for details.

Model	Domain	
	Barents Sea	BaSIC0.8
BaSIC0.8		76
BaSIC2	63	76
SVIM4	57	68

Table 7: Root-mean square distance between the ice edge in the observations and in the model results, in km. The ice edge detection algorithm is described in the text. Results for the Barents Sea domain (domain depicted in Figure 41) were discarded when the sea ice edge consisted of fewer than 100 grid cells, as explained in the text.

Model	Domain		Domain	
	Barents Sea	BaSIC0.8	Barents Sea	BaSIC0.8
	Sea ice area		Sea ice extent	
OSI-SAF	203	72	264	92
BaSIC0.8		64		93
BaSIC2	189	60	265	89
SVIM4	202	70	266	98

Table 8: Mean sea ice area and mean sea ice extent in 2000-2001, both in units of 1000 km^2. OSI-SAF is the product derived from satellite data, as described in Section 4.3. The Barents Sea domain is depicted in Figure 41.

		Observations						Model
		0-4%	4-10%	10-30%	30-50%	50-80%	80-100%	sum
BaSIC0.8	0-4%		0.537	0.076	0.014	0.007	0.000	0.63
	4-10%	0.014	0.011	0.007	0.004	0.003	0.000	0.04
	10-30%	0.017	0.014	0.012	0.008	0.007	0.002	0.06
	30-50%	0.009	0.009	0.009	0.009	0.011	0.004	0.05
	50-80%	0.007	0.007	0.009	0.013	0.029	0.018	0.08
	80-100%	0.004	0.001	0.003	0.005	0.027	0.092	0.13
BaSIC2	0-4%		0.531	0.077	0.016	0.010	0.001	0.64
	4-10%	0.016	0.013	0.008	0.004	0.003	0.000	0.04
	10-30%	0.022	0.018	0.014	0.009	0.010	0.003	0.08
	30-50%	0.007	0.007	0.007	0.008	0.012	0.006	0.05
	50-80%	0.006	0.004	0.006	0.009	0.024	0.022	0.07
	80-100%	0.006	0.002	0.003	0.006	0.024	0.083	0.12
SVIM4	0-4%		0.543	0.069	0.010	0.004	0.000	0.63
	4-10%	0.010	0.009	0.007	0.003	0.001	0.000	0.03
	10-30%	0.015	0.013	0.013	0.007	0.005	0.000	0.05
	30-50%	0.010	0.010	0.012	0.008	0.008	0.001	0.05
	50-80%	0.007	0.006	0.013	0.016	0.028	0.010	0.08
	80-100%	0.003	0.001	0.004	0.008	0.039	0.106	0.16
Observations	sum	0.05	0.58	0.12	0.05	0.08	0.12	1.00

Table 9: Confusion matrix for six categories of daily sea ice concentrations during 2000-2001. Values are fraction of relative occurence, after discarding grids where concentrations in both model and observations were $<$4%. For all three models, this corresponds to removal of 53% of all wet grids. Note that the aggregated results for each observation category differs slightly between models. This is due to the fact that the discarded ("common ice free") area is not identical for the various models.

8 Figures

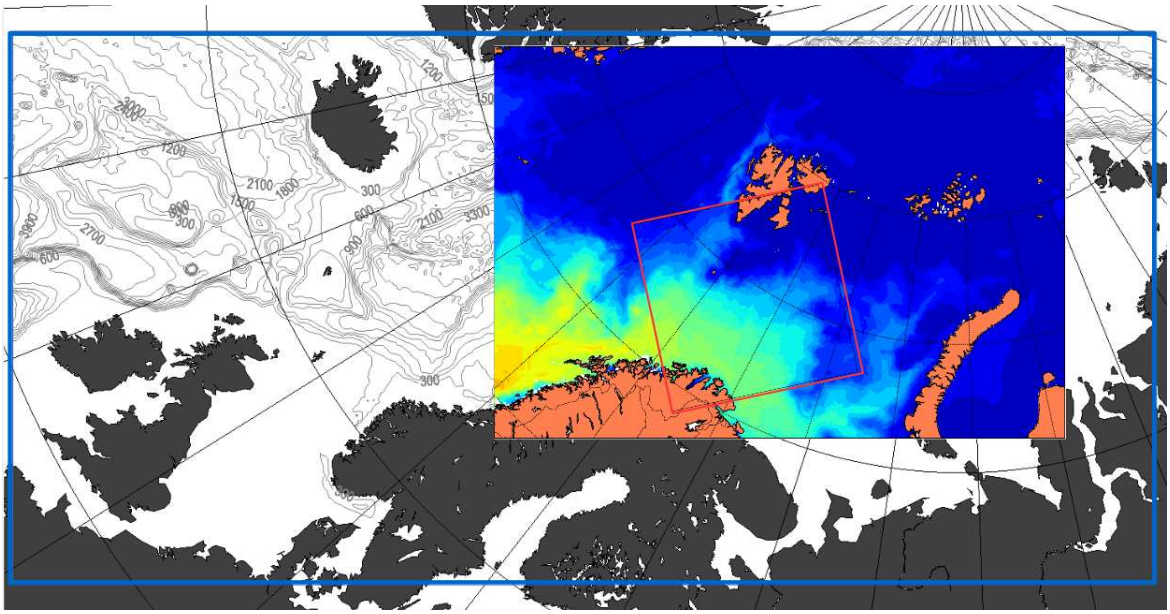

Figure 1: Outlined is the geographical coverage of the three grids included in the triply nested grid configuration used in BaSIC. The outermost parent, referred to as SVIM4, has boundaries outlined by the blue rectangle. Its child, referred to as BaSIC2, is embedded wholy within SVIM4, and its boundaries are depicted as the boundaries of the colored frame. The boundaries of the innermost child, or the ultra-fine mesh model grid referred to as BaSIC0.8, is outlined by the red rotated rectangle. Shown in black curves within the SVIM4 domain is its topography. The colors shown for the BaSIC2 grid is temperature with warmer water (yellowish colors) along the Norwegian coast.

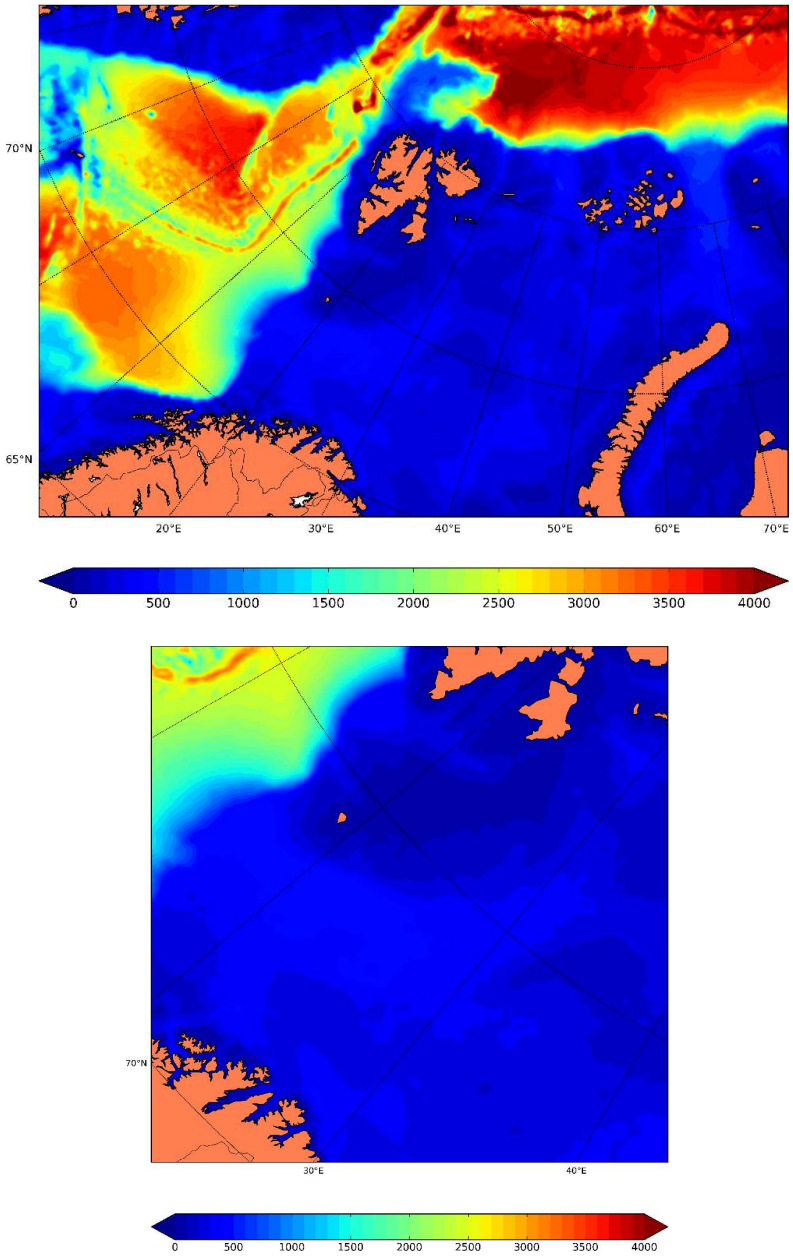

Figure 2: The topography of the BaSIC2 (upper) and the BaSIC0.8 (bottom) grids. The color scale indicates the depth in intervals of 100 m in the range 0 to 4000 m.

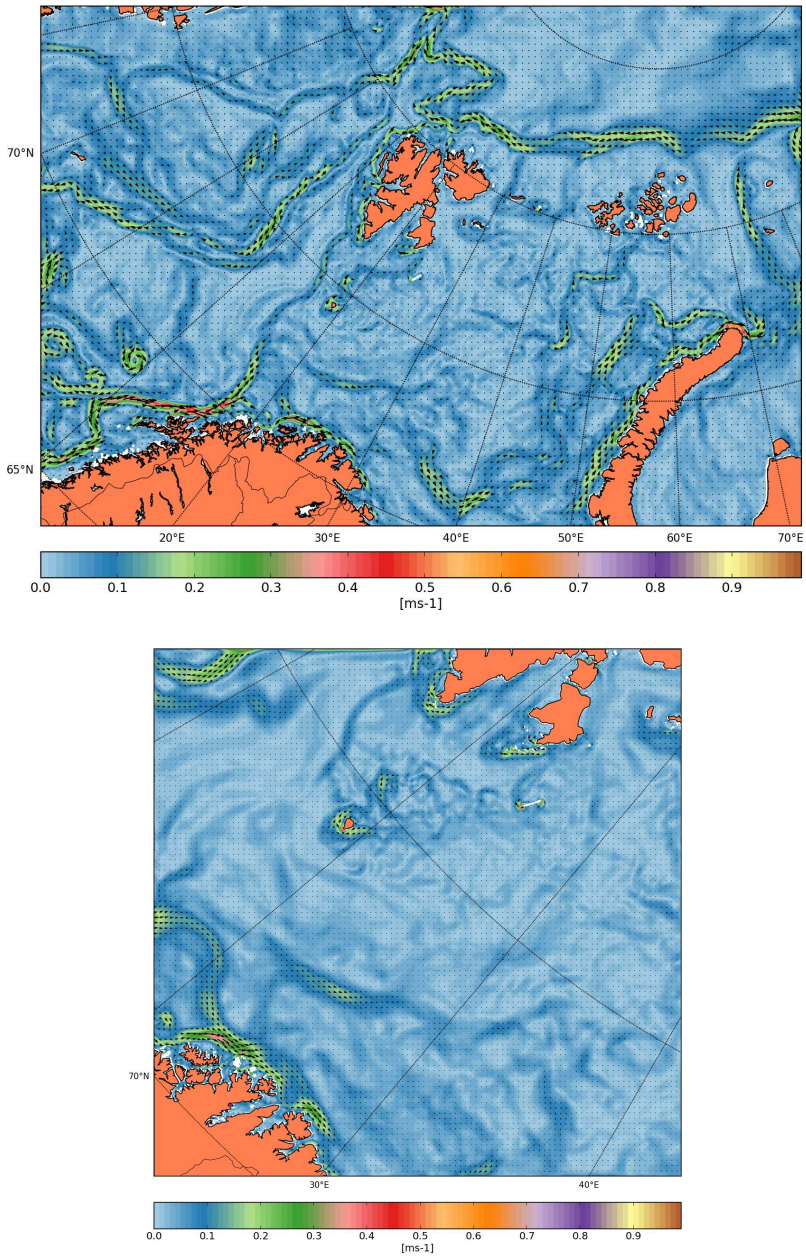

Figure 3: Average surface currents for the year 2000 from the STD hindcast. Upper panel is from the BaSIC2 grid, while the lower panel is from the BaSIC0.8 grid. The contour interval is 0.01 ms^{-1} and range from 0 cms^{-1} to 1 ms^{-1}.

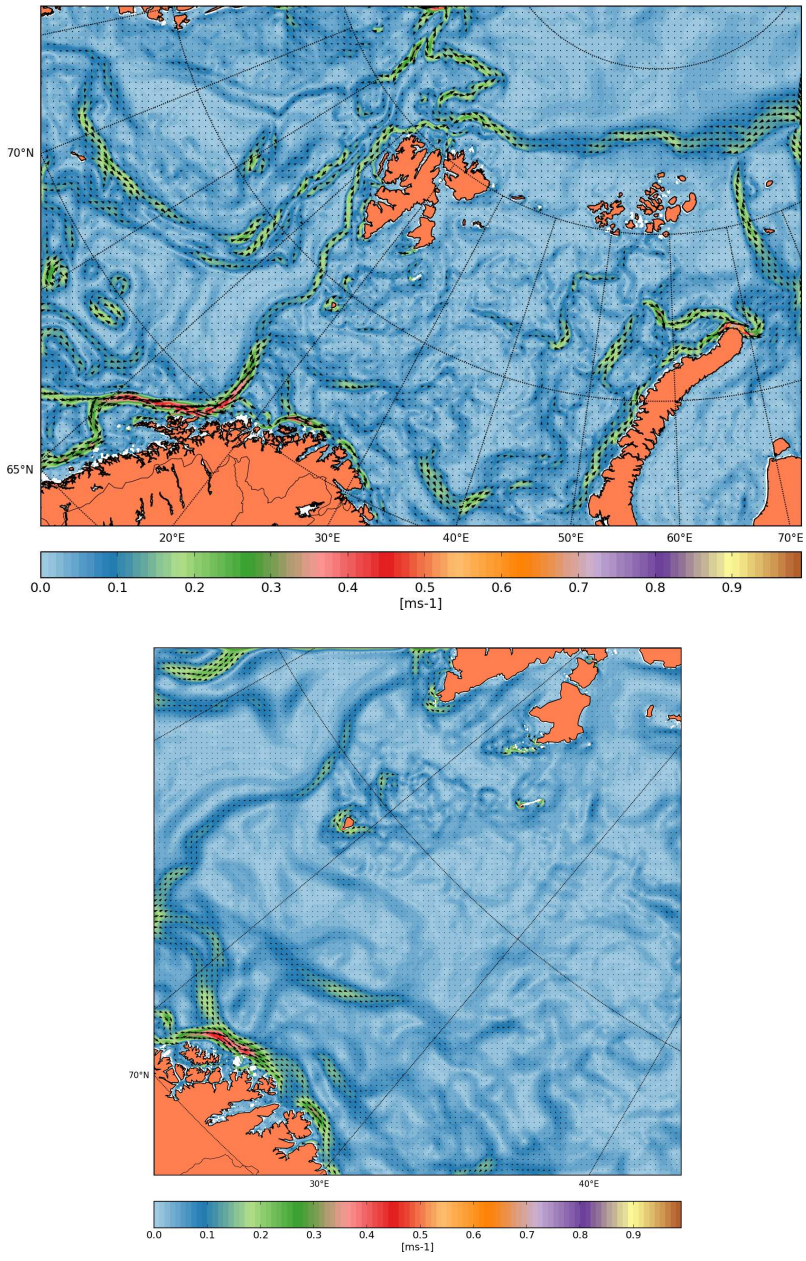

Figure 4: As Figure 3 except for the year 2001.

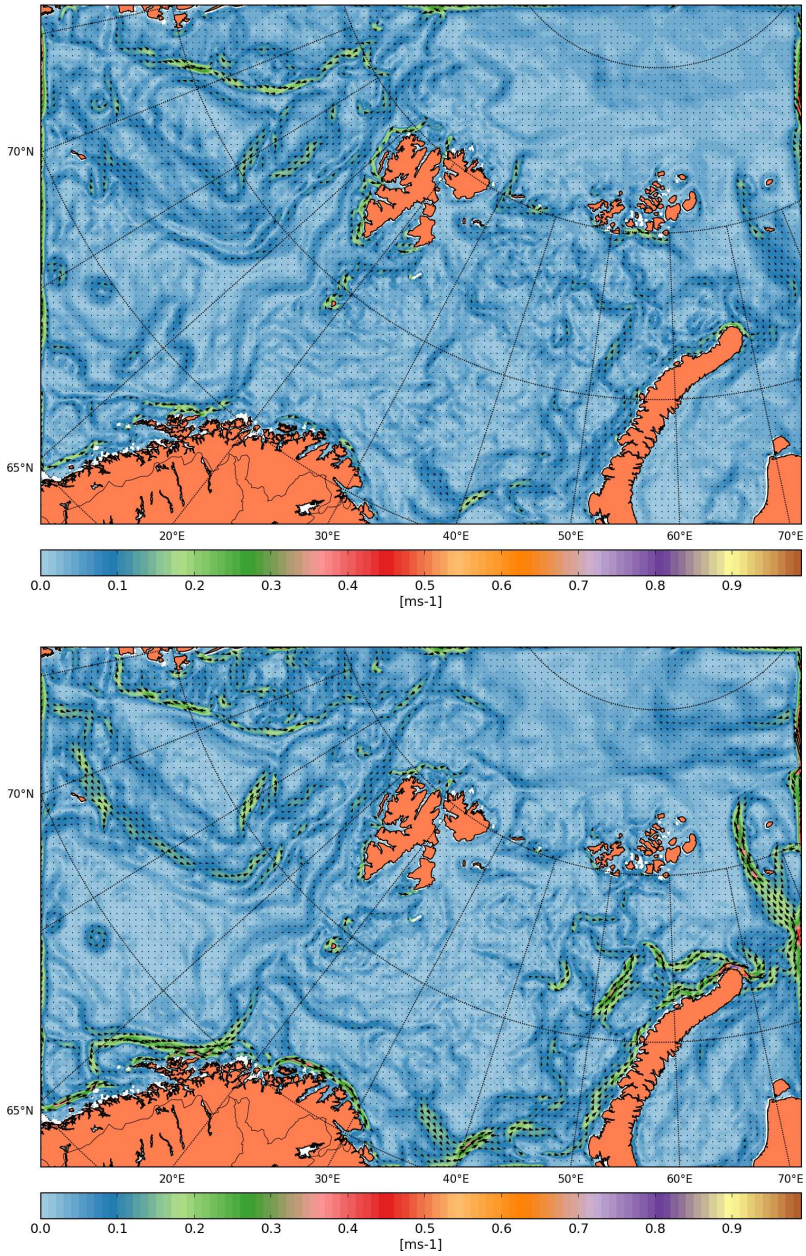

Figure 5: As Figure 3, but for the years 2010 (upper) and 2011 (bottom), respectively, that is, from the EXP1 hindcast.

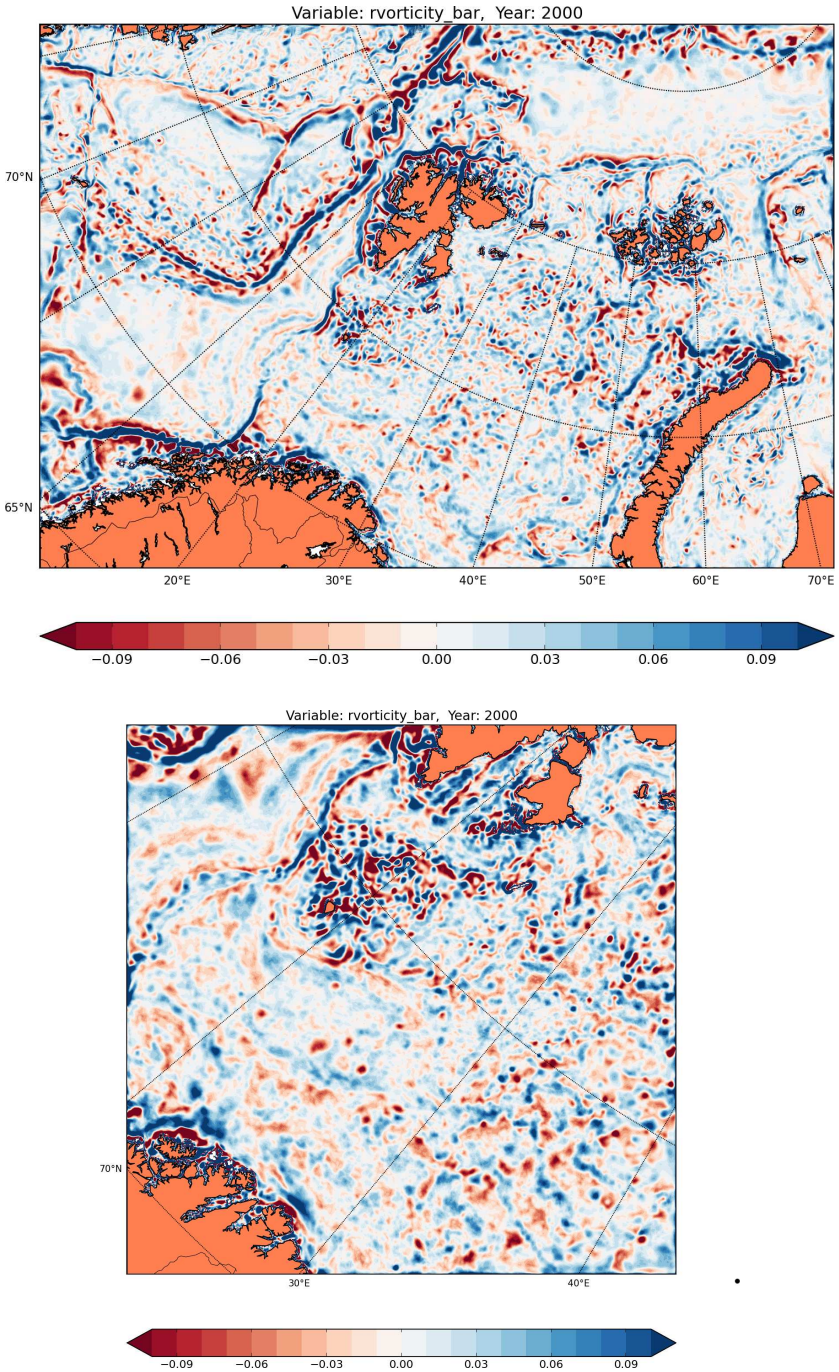

Figure 6: Yearly mean relative vorticity of the depth integrated currents for the year 2000 (upper) and year 2001 (bottom) for the STD hindcast from the BaSIC2 grid. The vorticity is normalized by the Coriolis parameter. The range is -0.1 to +0.1. Contour interval is 0.01.

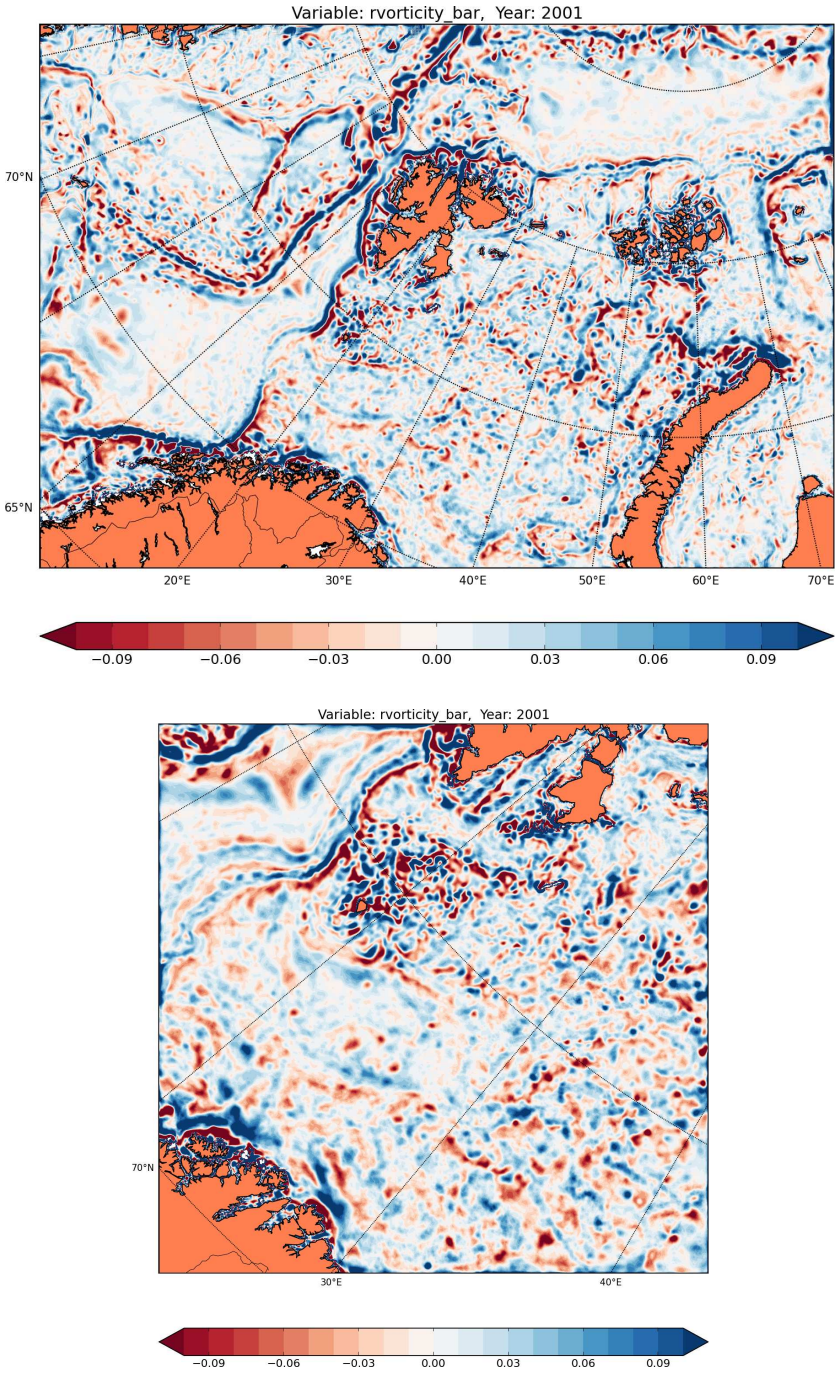

Figure 7: As Figure 6 except for the year 2001.

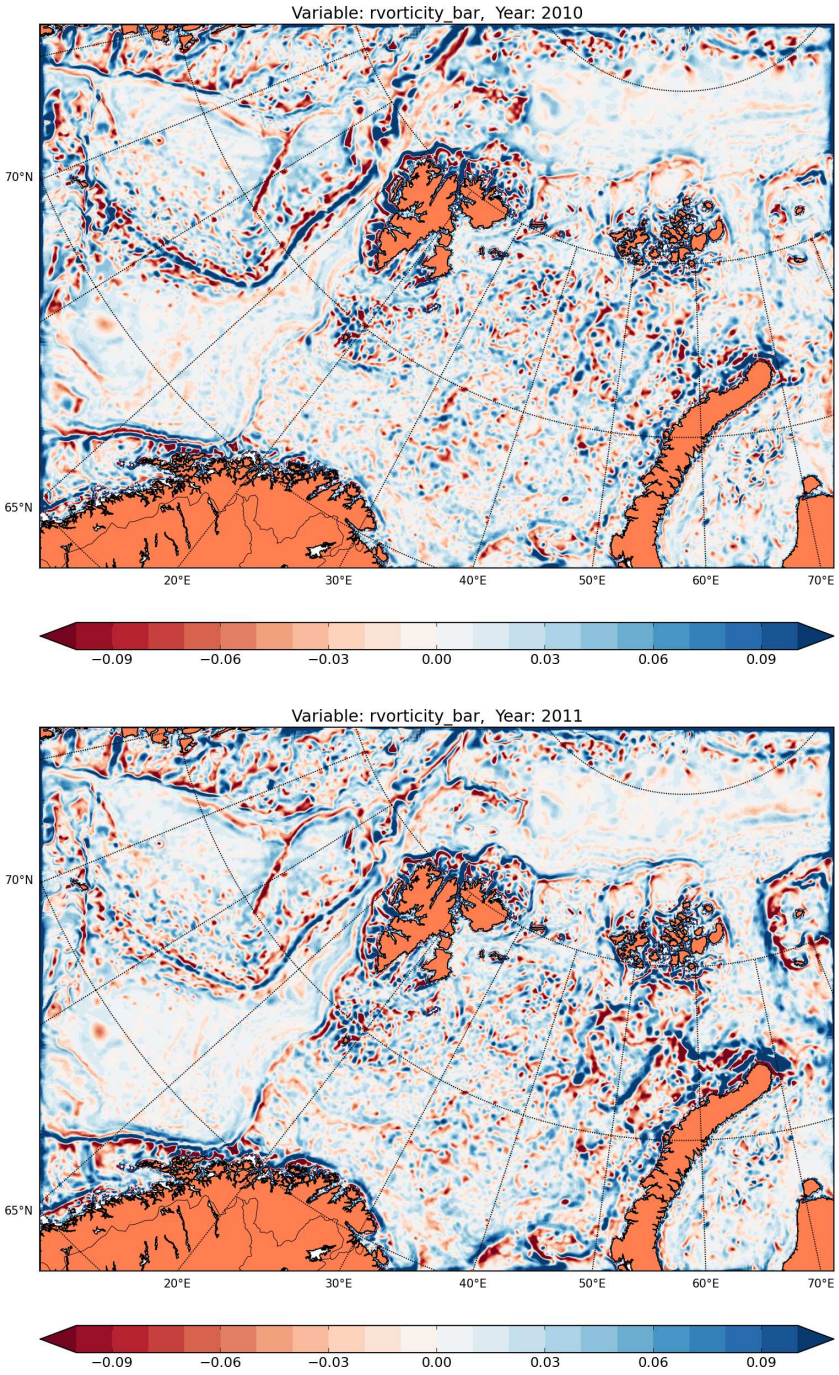

Figure 8: As Figure 6, but for the years 2010 (upper) and 2011 (bottom), respectively, that is, from the EXP1 hindcast.

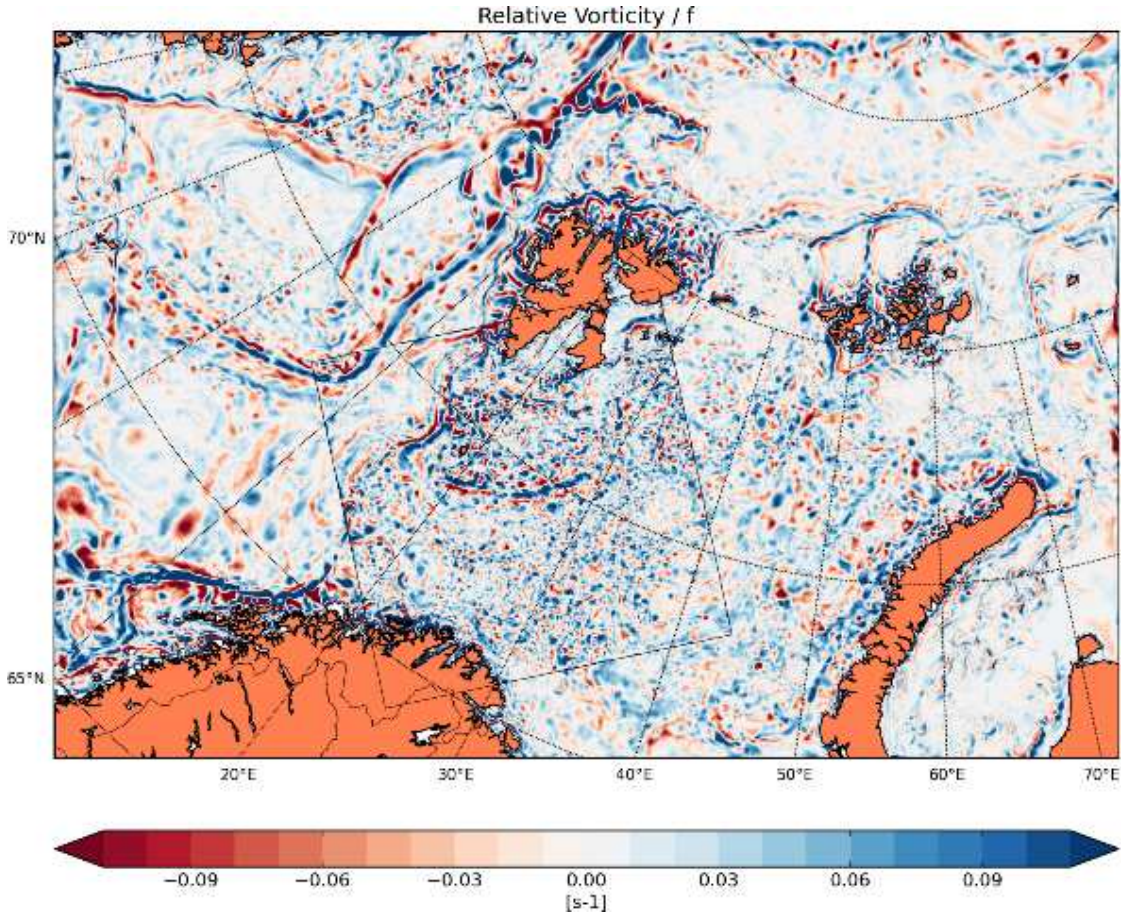

Figure 9: Monthly mean relative vorticity of the depth integrated currents for the month of March 2000 for the STD hindcast. Note that the vorticity from the the BaSIC0.8 grid is superimposed on the vorticity of the BaSIC2 grid. The vorticity is normalized by the Coriolis parameter. The range is -0.1 to +0.1. Contour interval is 0.005.

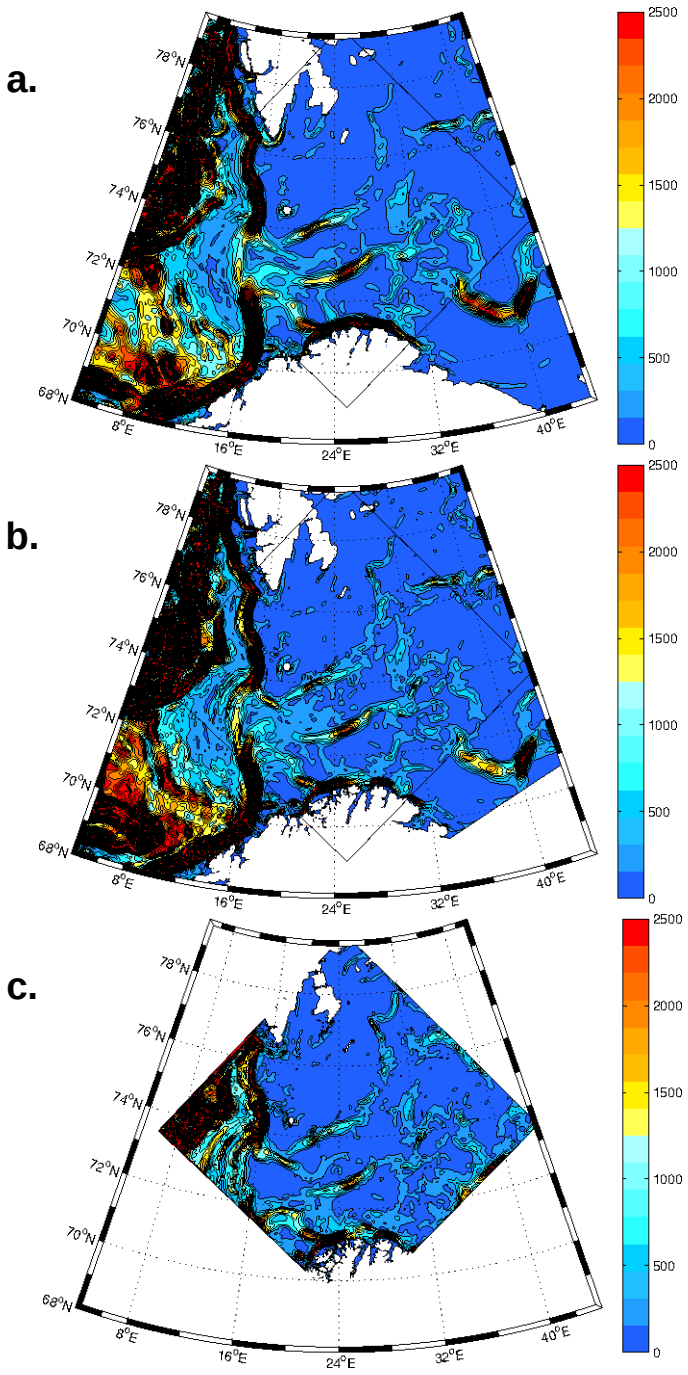

Figure 10: Depicted is the depth integrated, two-year mean kinetic energy component (MKE) extracted from the SVIM4 grid (a), the BaSIC2 grid (b) and the BaSIC0.8 grid (c) for the STD hindcast. The contour lines denote energy in Jm^{-2} and the colors are truncated with red at 2500 Jm^{-2}. The black square outlines the domain of the BaSIC0.8 grid.

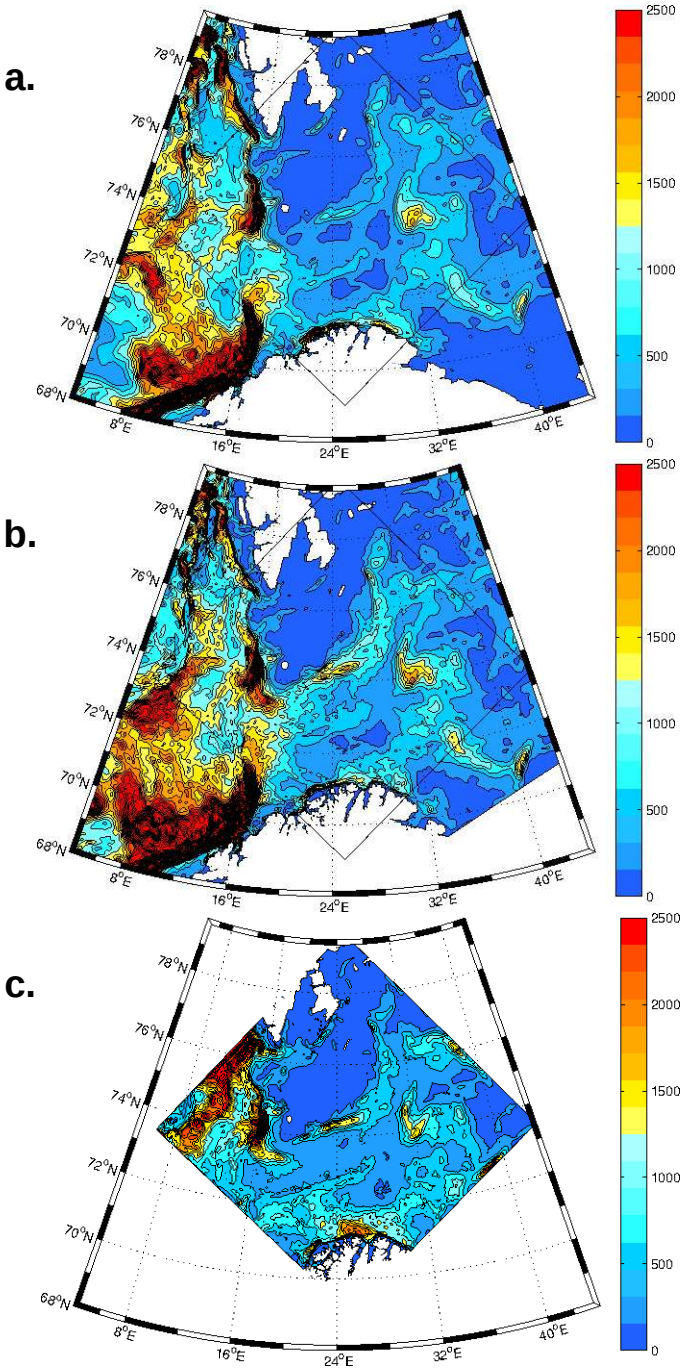

Figure 11: As Figure 10, but showing the two-year mean of the eddy kinetic energy (EKE) for the STD hindcast.

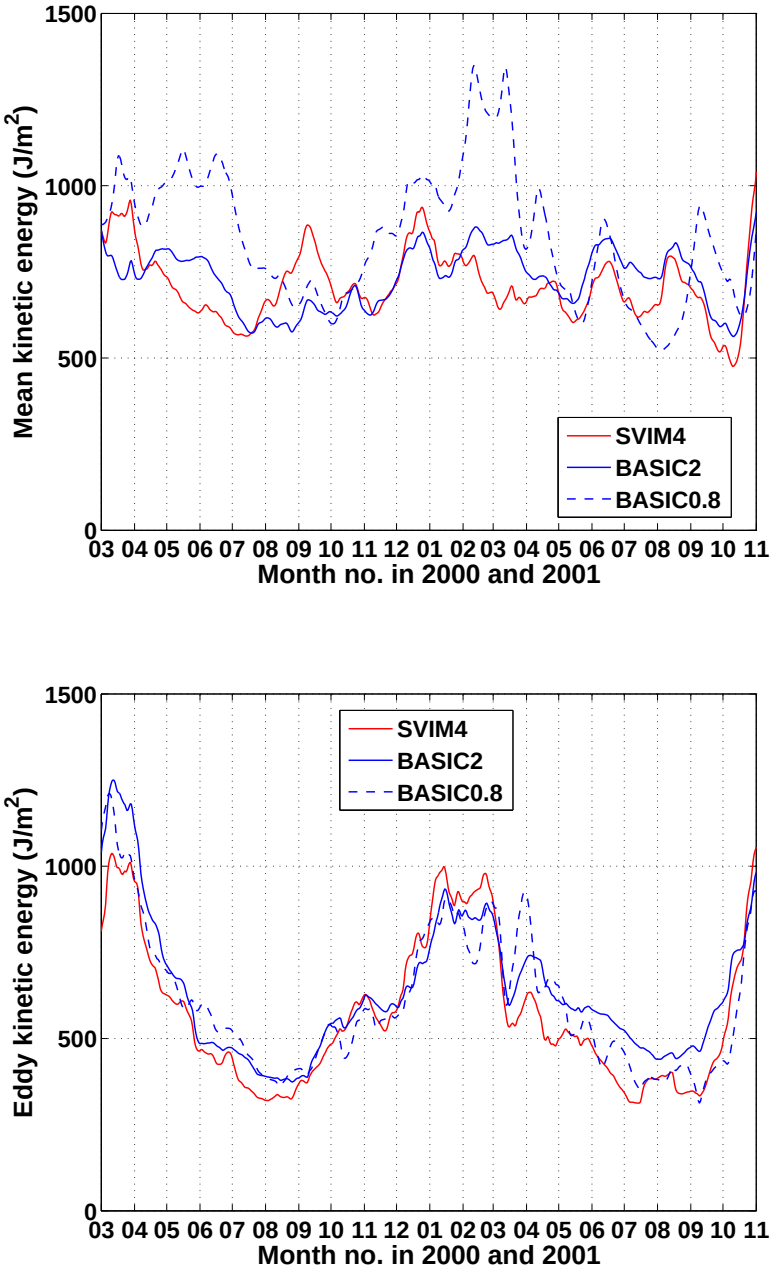

Figure 12: Time series of running 30 day means of MKE (upper) and EKE (bottom) based on current fields from SVIM4, BaSIC2 and BaSIC0.8 for an area limited to the extension of the BaSIC0.8 grid.

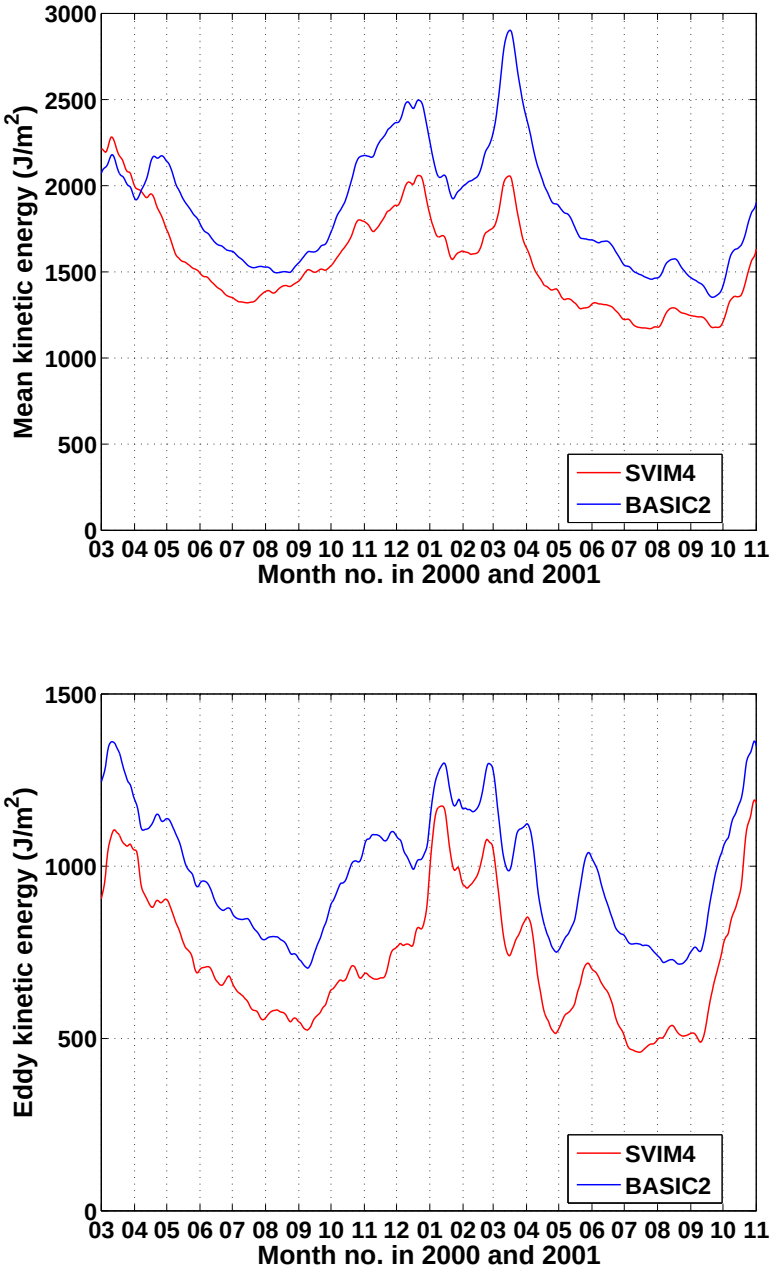

Figure 13: Time series of running 30 day means of MKE (upper) and EKE (bottom) based on current fields from SVIM4, BaSIC2 and BaSIC0.8 for an area limited to the extension of the BaSIC2 grid.

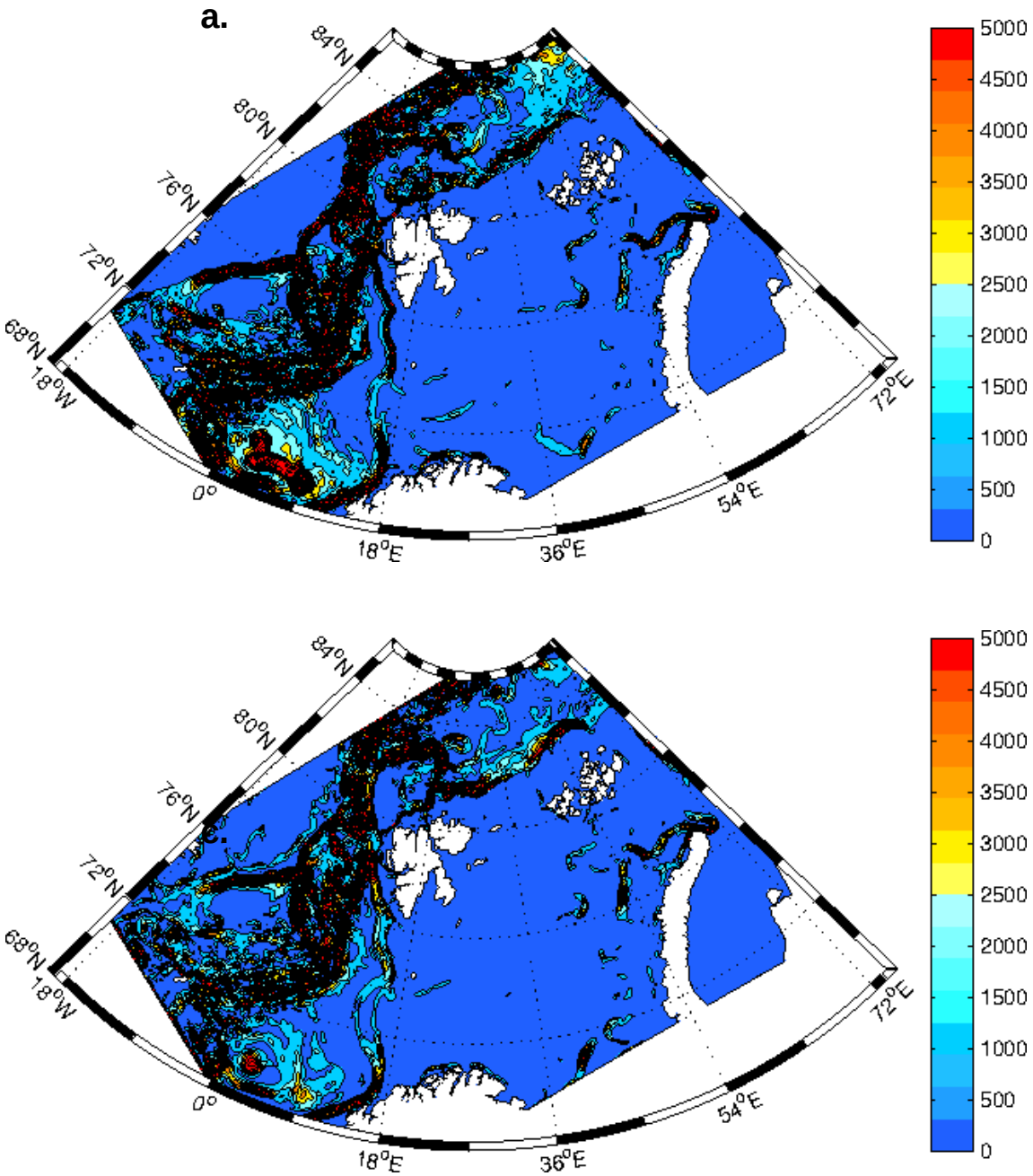

Figure 14: Depicted is the depth integrated, two-year mean kinetic energy component (MKE) extracted from the BaSIC2 grid for the STD hindcast (upper) and the EXP1 hindcast (bottom). The contour lines denote energy in Jm^{-2} and the colors are truncated with red at 5000 Jm^{-2}.

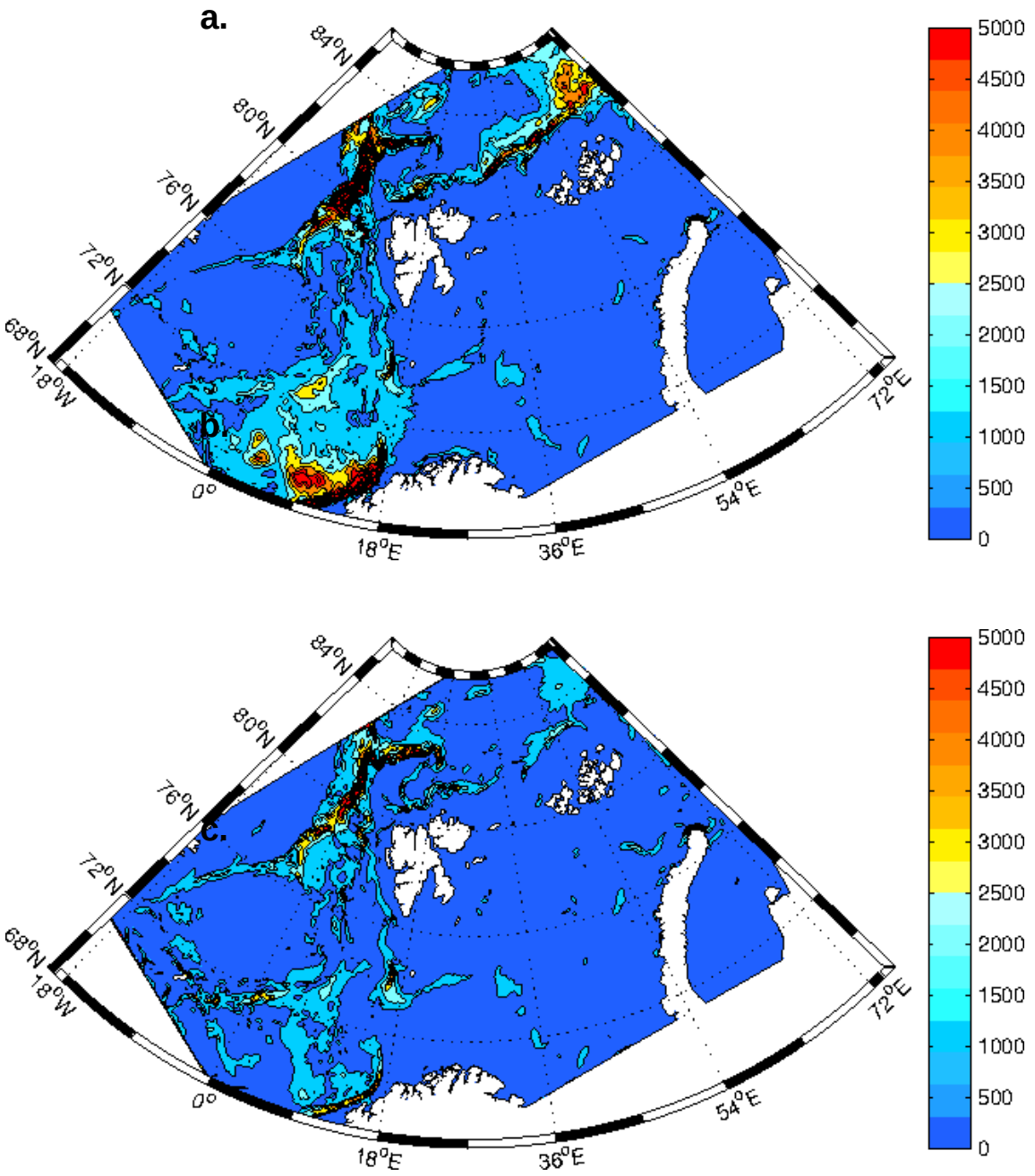

Figure 15: As Figure 14, but showing the two-year mean of the eddy kinetic energy (EKE).

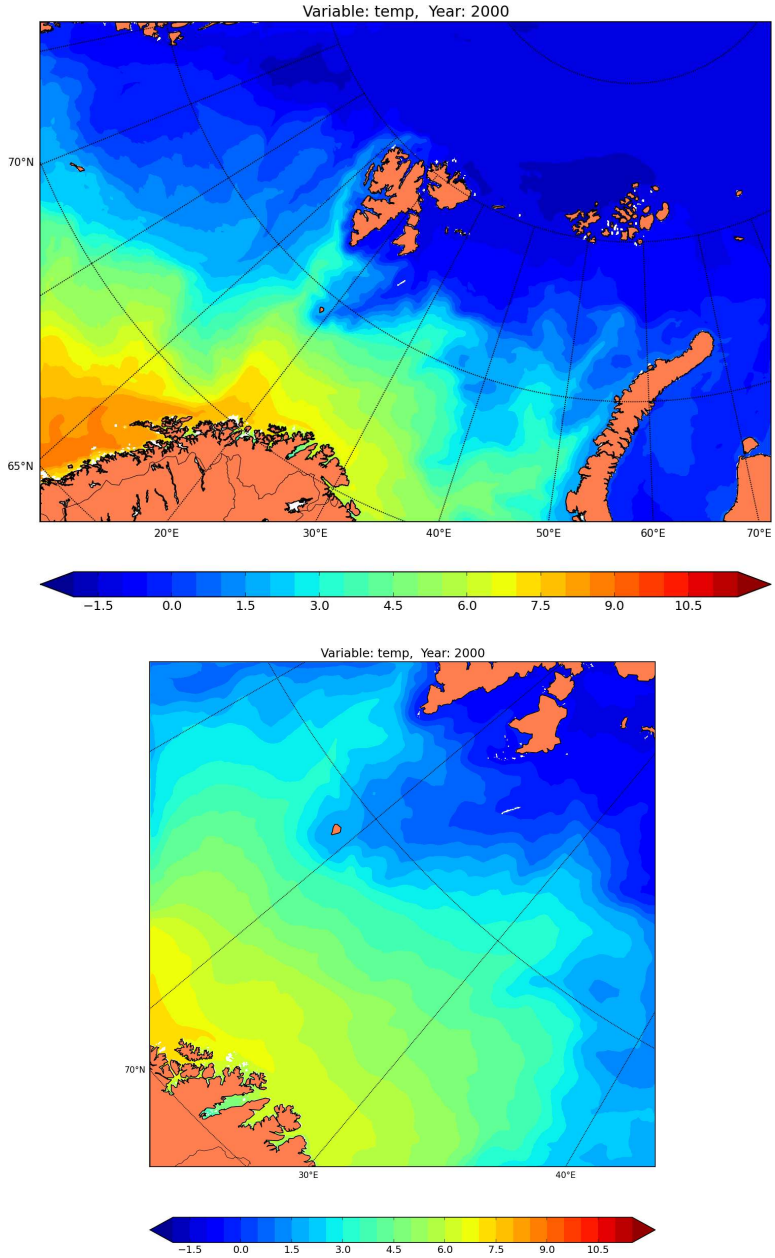

Figure 16: Average sea surface temperature (SST) for the year 2000 from the STD hindcast. Upper panel is from the BaSIC2 grid, while the lower panel is from the BaSIC0.8 grid. The contour interval is 0.5^{o}C and range from -2^{o}C to 11.5^{o}C.

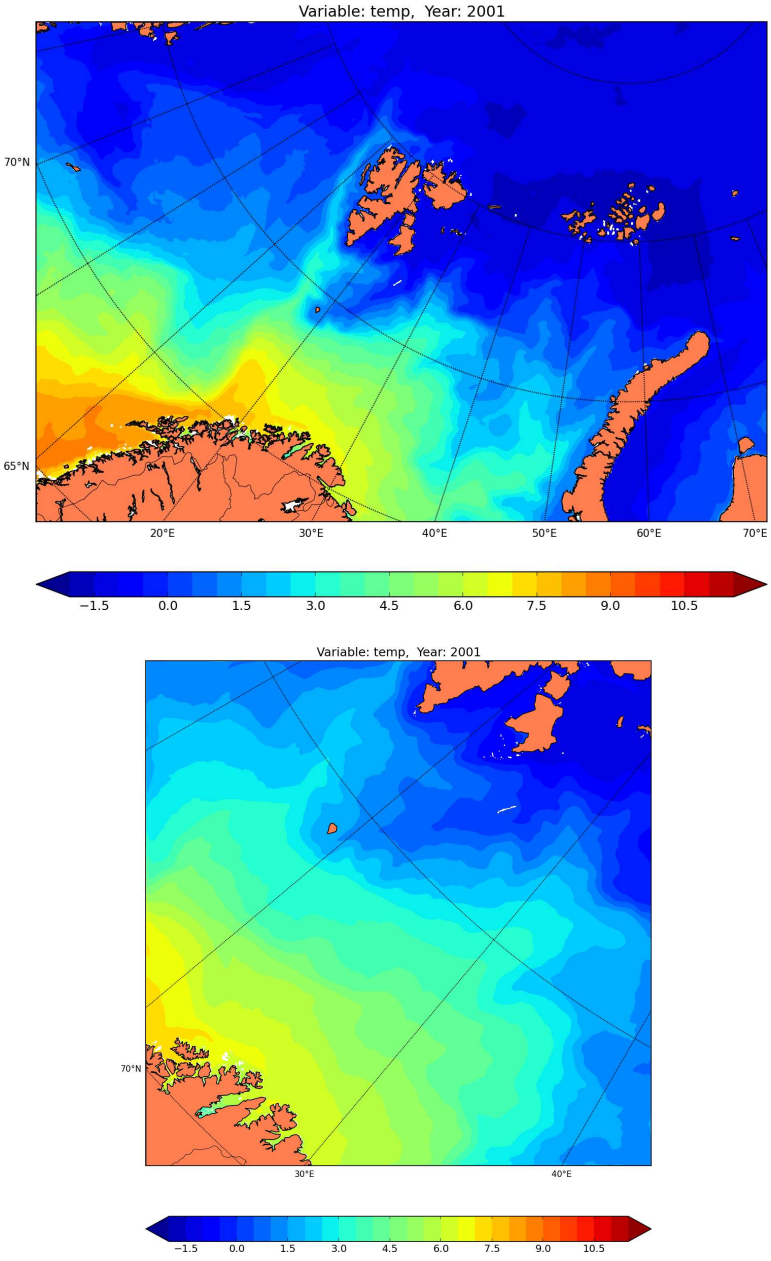

Figure 17: As Figure 16 except for the year 2001.

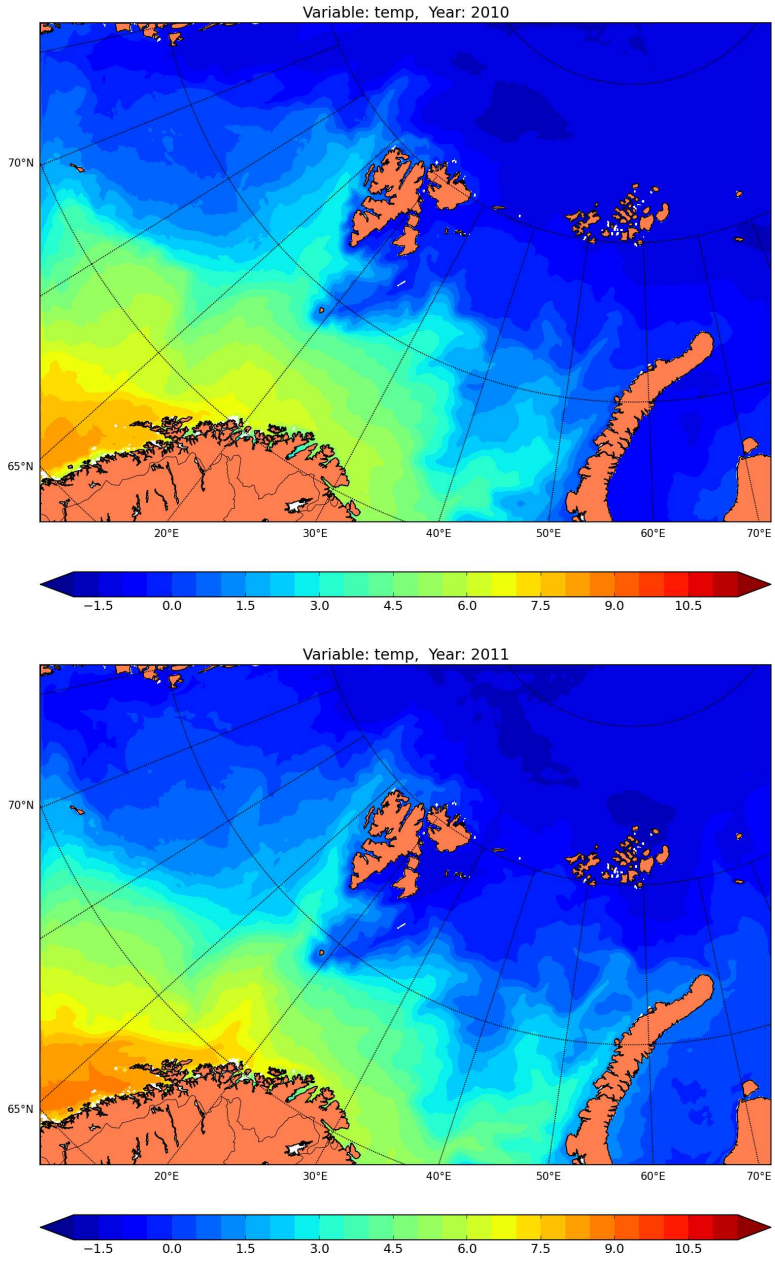

Figure 18: As Figure 16, but for the years 2010 (upper) and 2011 (bottom), respectively, that is, from the EXP1 hindcast.

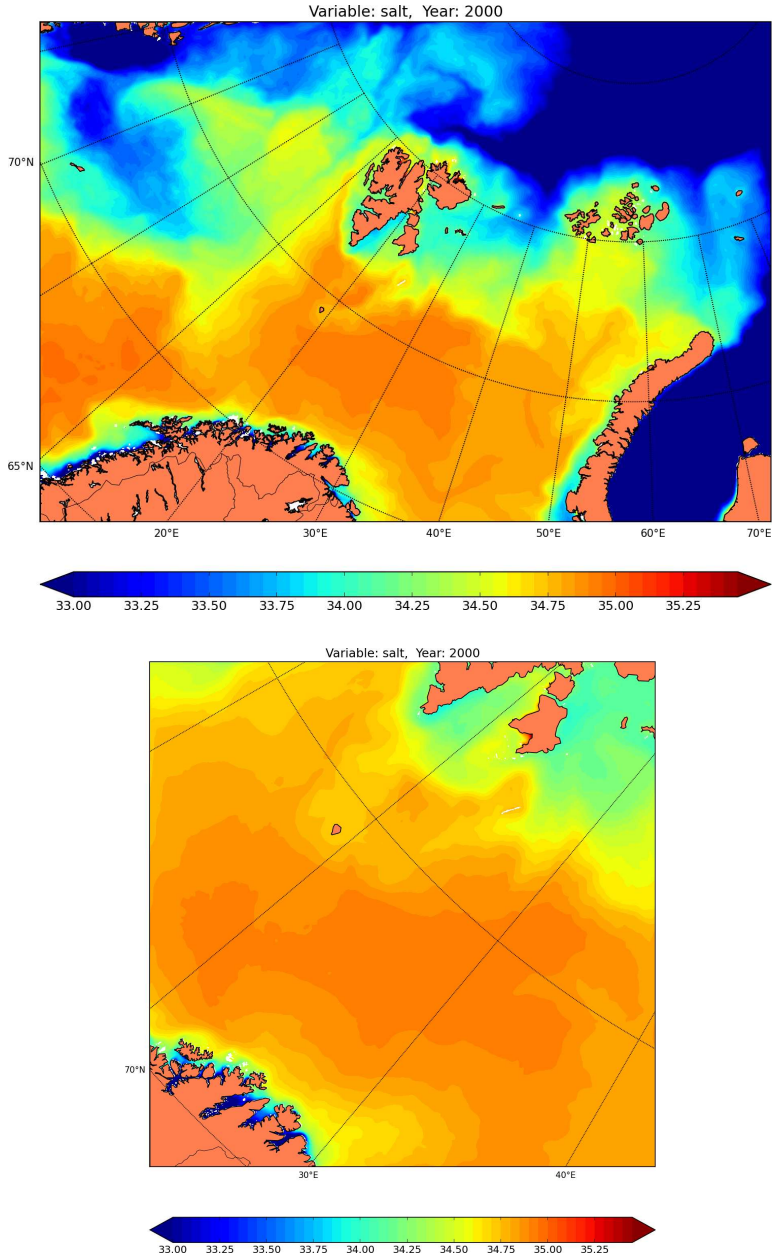

Figure 19: Average sea surface salinity (SSS) for the year 2000 from the STD hindcast. Upper panel is from the BaSIC2 grid, while the lower panel is from the BaSIC0.8 grid. The contour interval is 0.5^{o}C and range from -2^{o}C to 11.5^{o}C.

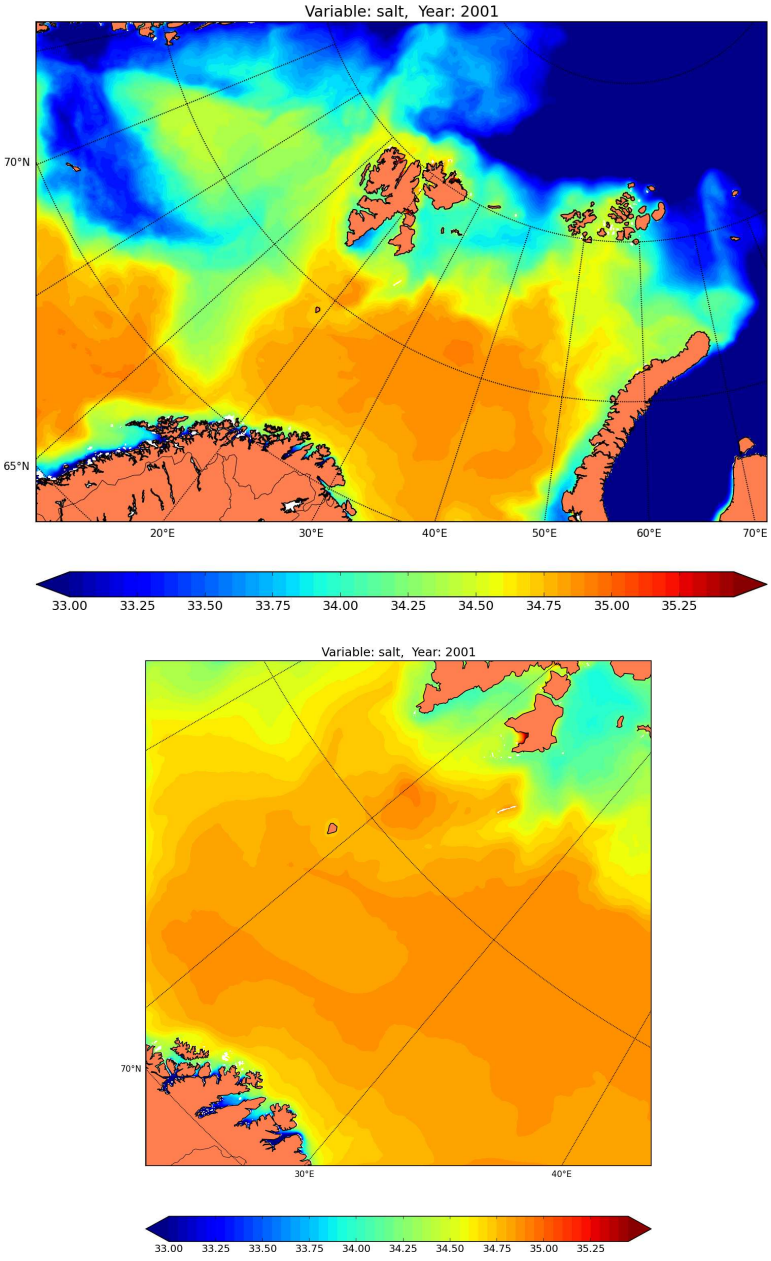

Figure 20: As Figure 19 except for the year 2001.

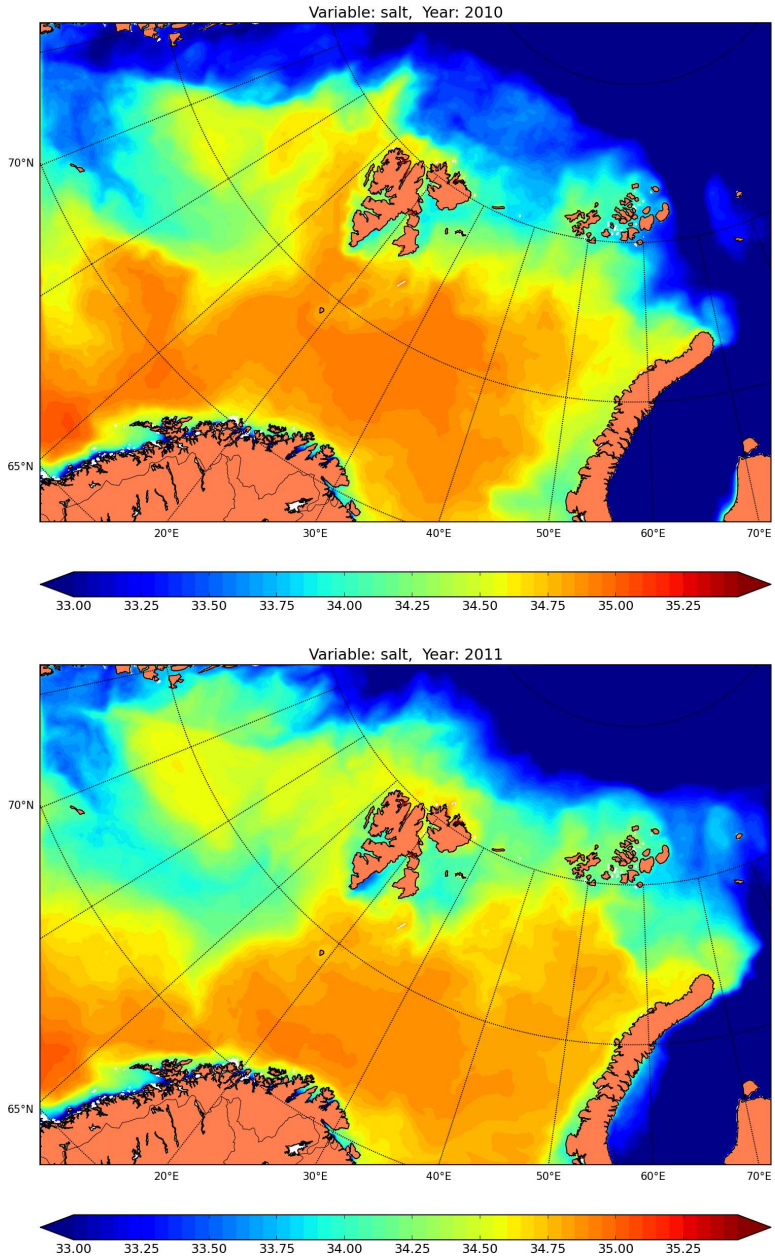

Figure 21: As Figure 19, but for the years 2010 (upper) and 2011 (bottom), respectively, that is, from the EXP1 hindcast.

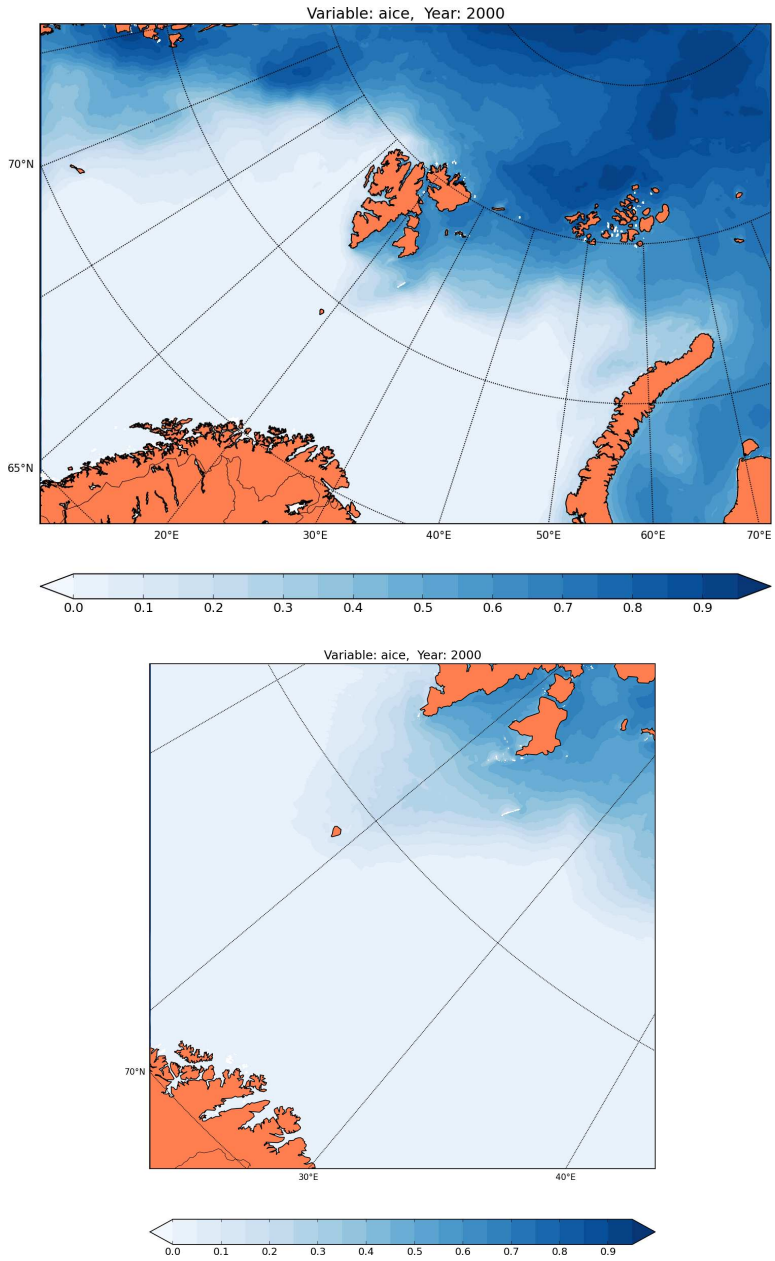

Figure 22: Yearly mean sea ice concentration (SIC) for the year 2000 from the STD hindcast. Upper panel is from the BaSIC2 grid, while the lower panel is from the BaSIC0.8 grid. Ice concentration is here measured in fraction in the range from 0 to 1. The contour interval is 0.05.

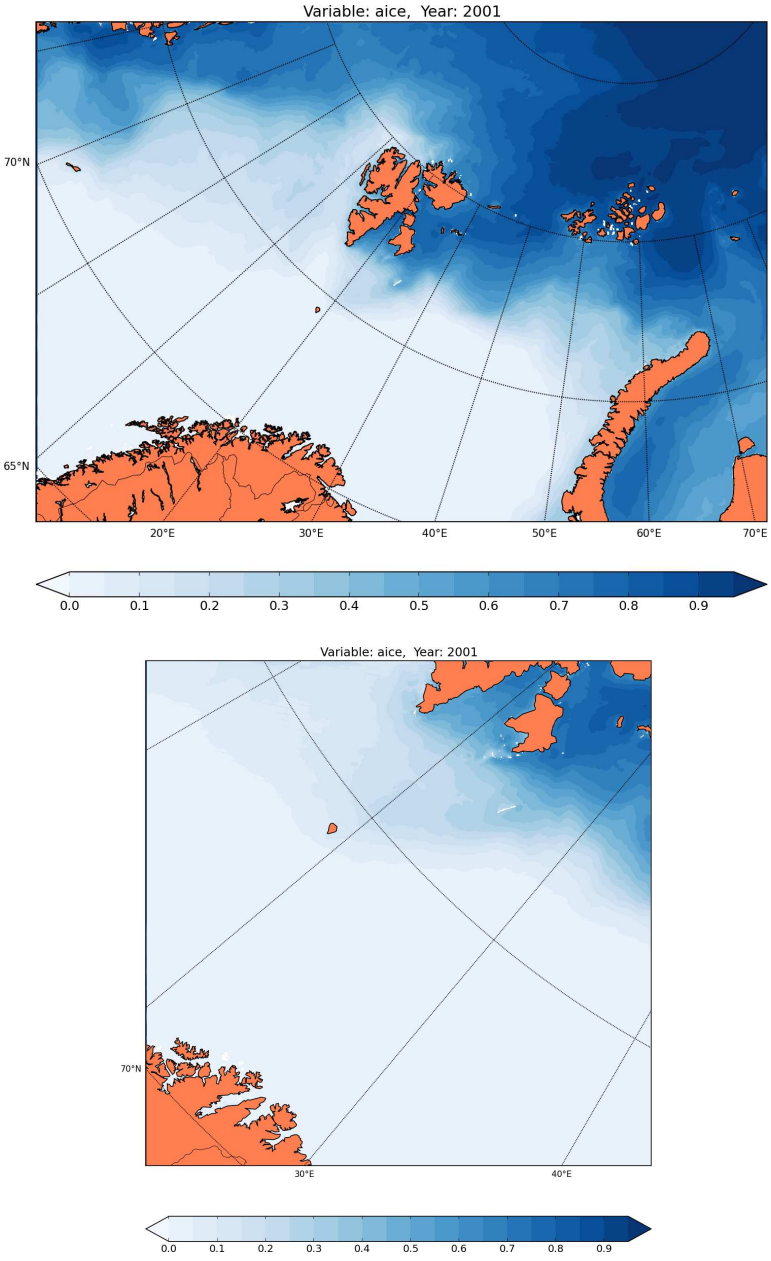

Figure 23: As Figure 22 except for the year 2001.

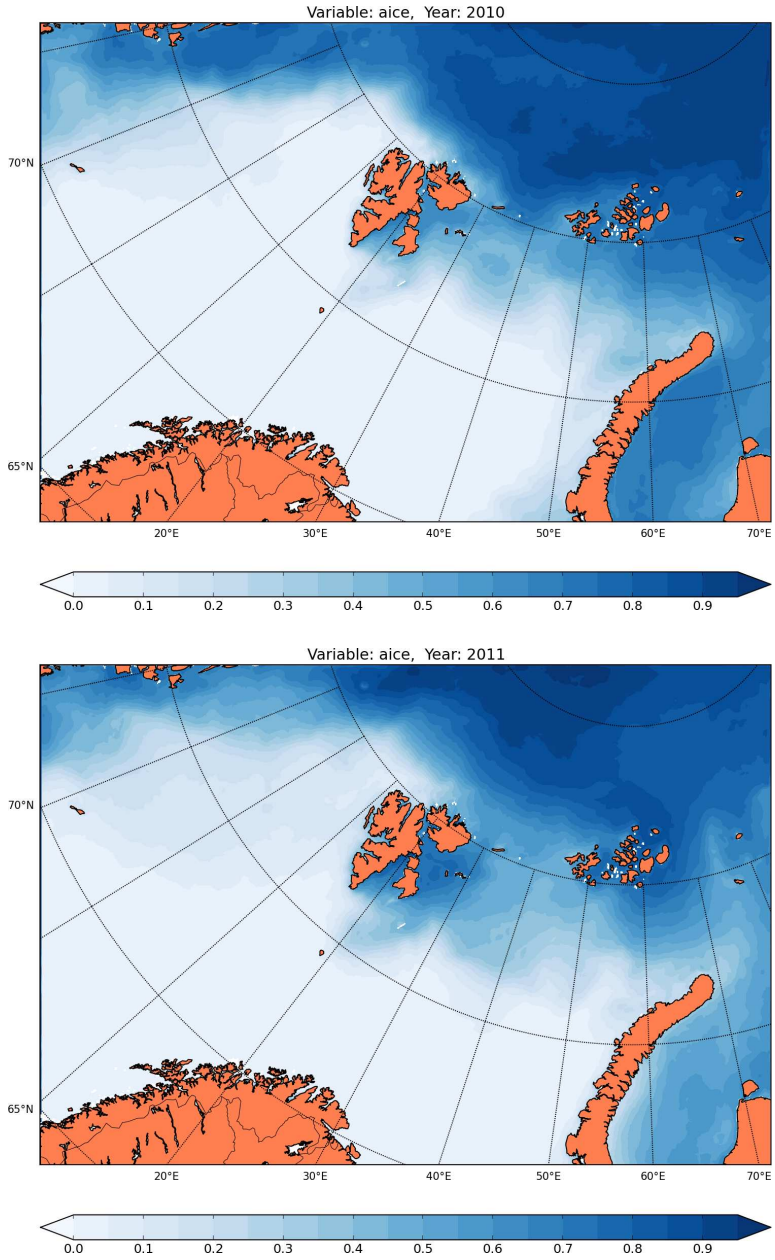

Figure 24: As Figure 22, but for the years 2010 (upper) and 2011 (bottom), respectively, that is, from the EXP1 hindcast.

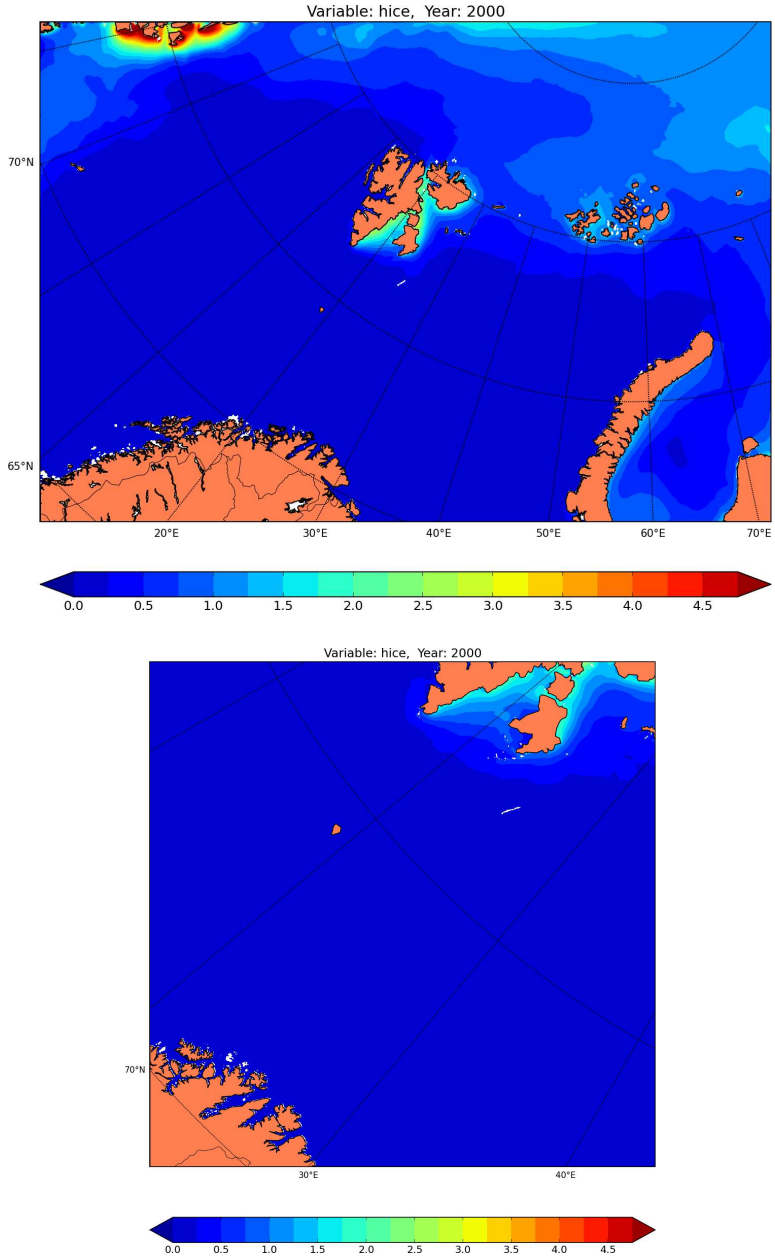

Figure 25: Yearly mean sea ice thickness (SIT) for the year 2000 from the STD hindcast. Upper panel is from the BaSIC2 grid, while the lower panel is from the BaSIC0.8 grid. The contour interval is 0.25 m and thickness is shown in the range 0 m to 4.75 m.

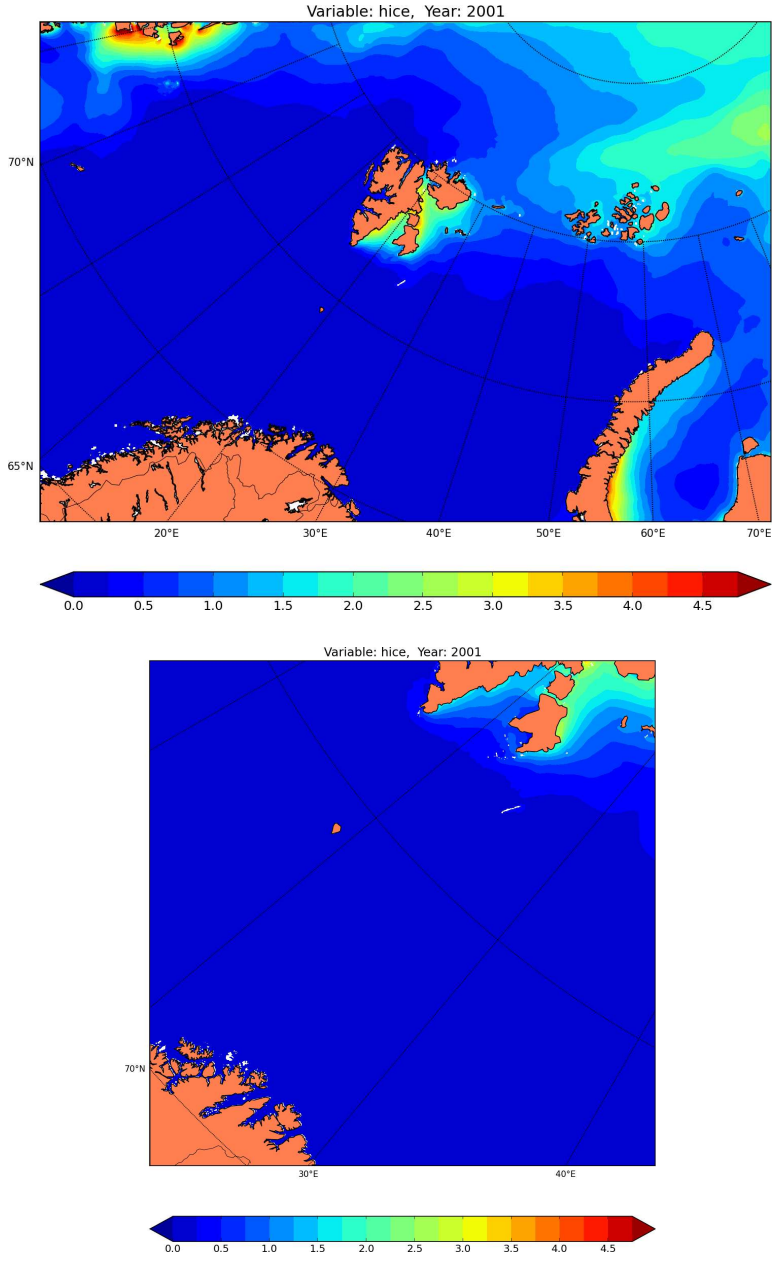

Figure 26: As Figure 25 except for the year 2001.

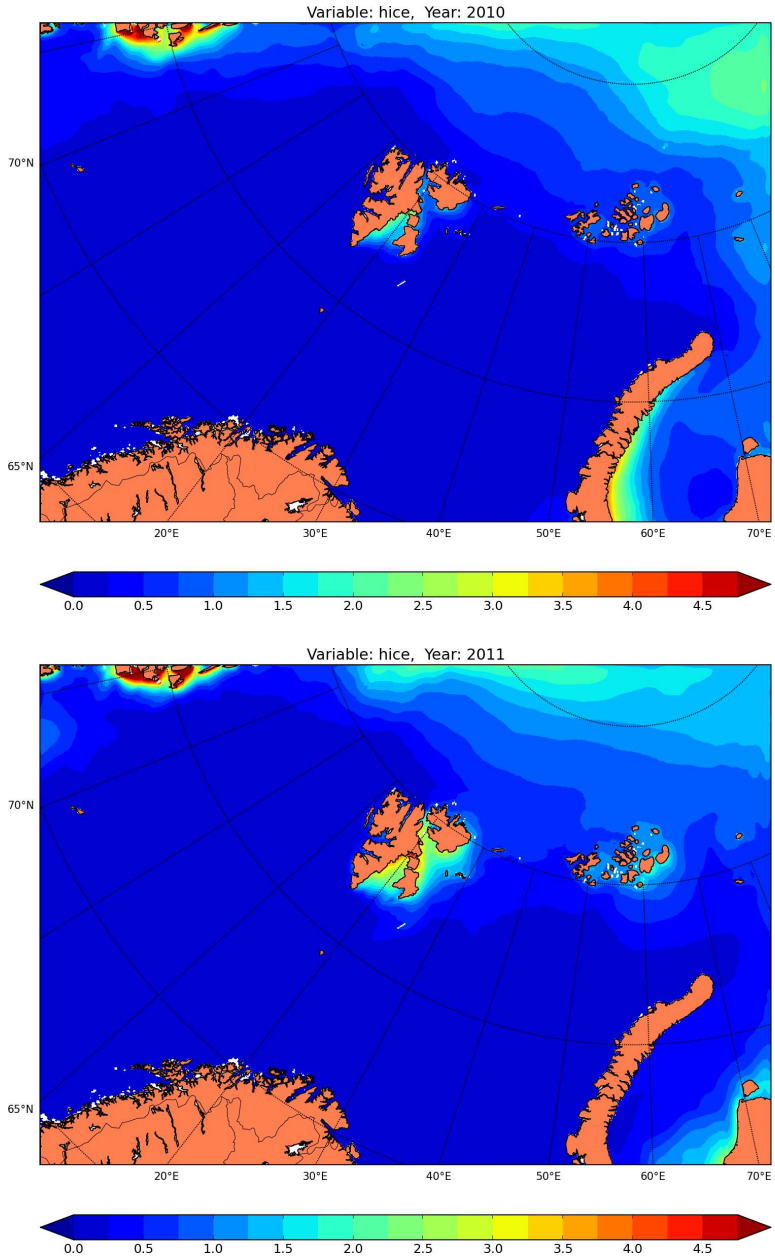

Figure 27: As Figure 25, but for the years 2010 (upper) and 2011 (bottom), respectively, that is, from the EXP1 hindcast.

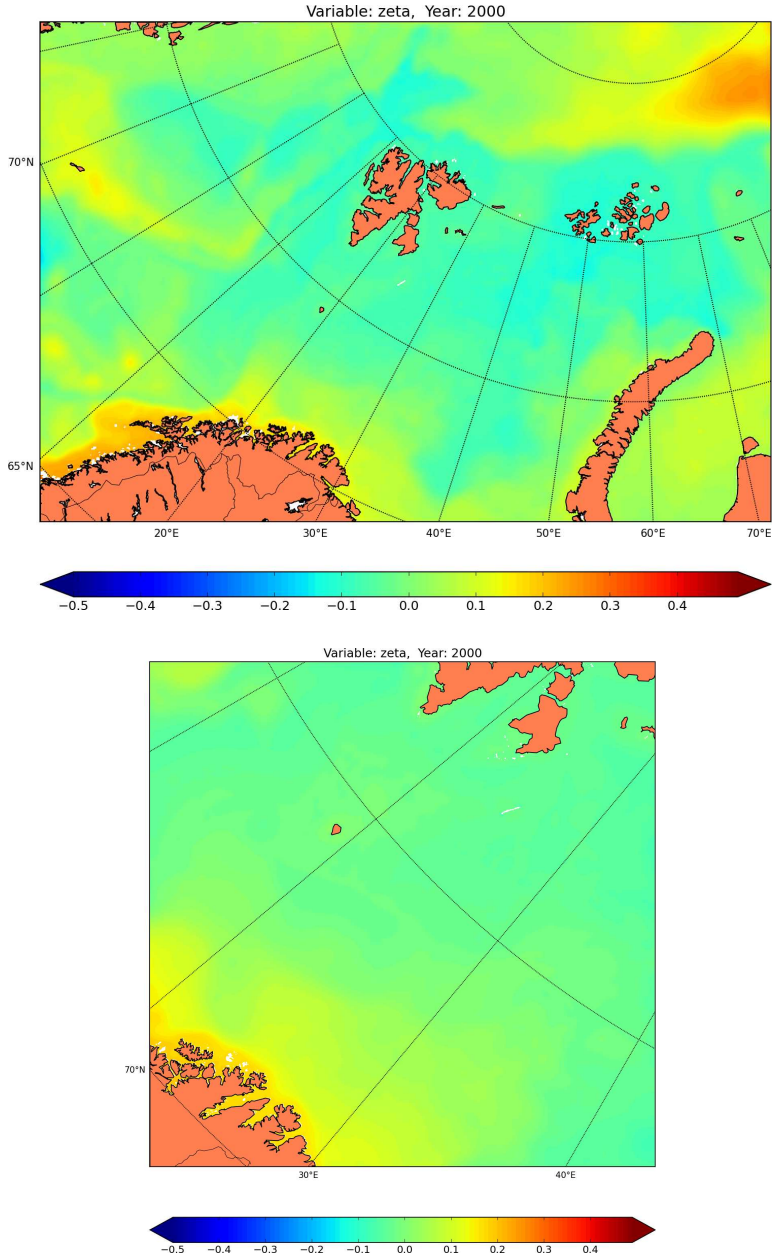

Figure 28: Yearly mean sea surface height anomaly (SSH) for the year 2000 from the STD hindcast. Upper panel is from the BaSIC2 grid, while the lower panel is from the BaSIC0.8 grid. The contour interval is 0.01 m and is shown in the range -0.5 m to +0.5 m.

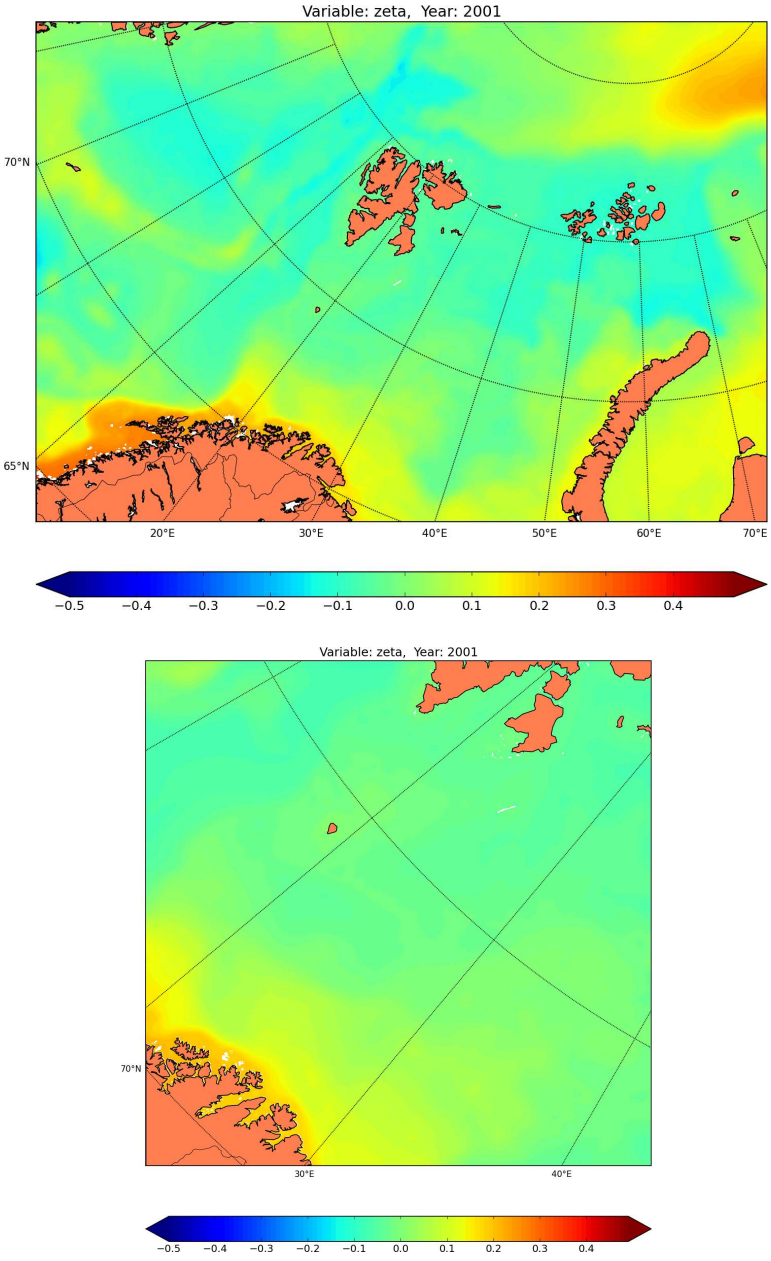

Figure 29: As Figure 28 except for the year 2001.

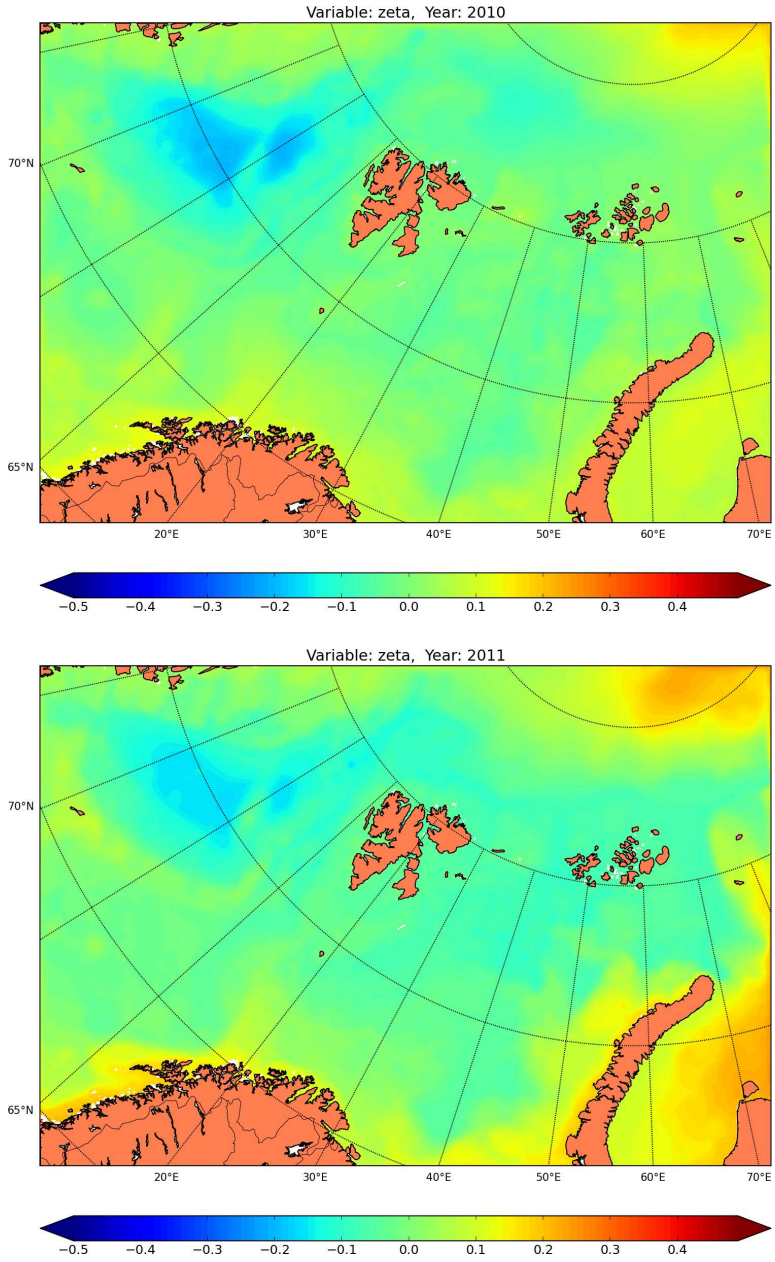

Figure 30: As Figure 28, but for the years 2010 (upper) and 2011 (bottom), respectively, that is, from the EXP1 hindcast.

clearpage

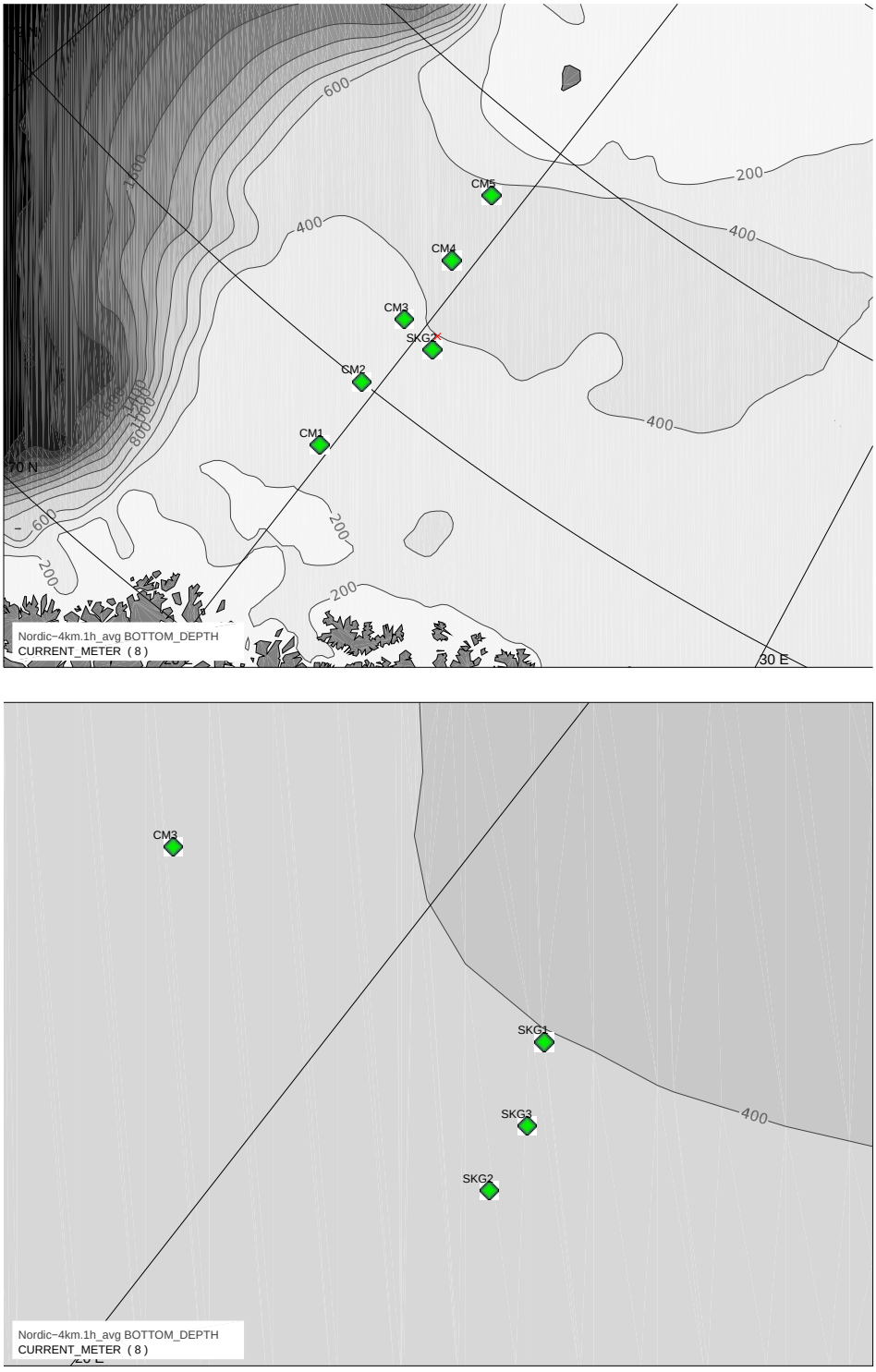

Figure 31: Observation sites of the current meters between Fugløya to the south and Bjørnøya to the north (CM1 - CM5) and the Skrugard Observations (SKG1 - SKG3).

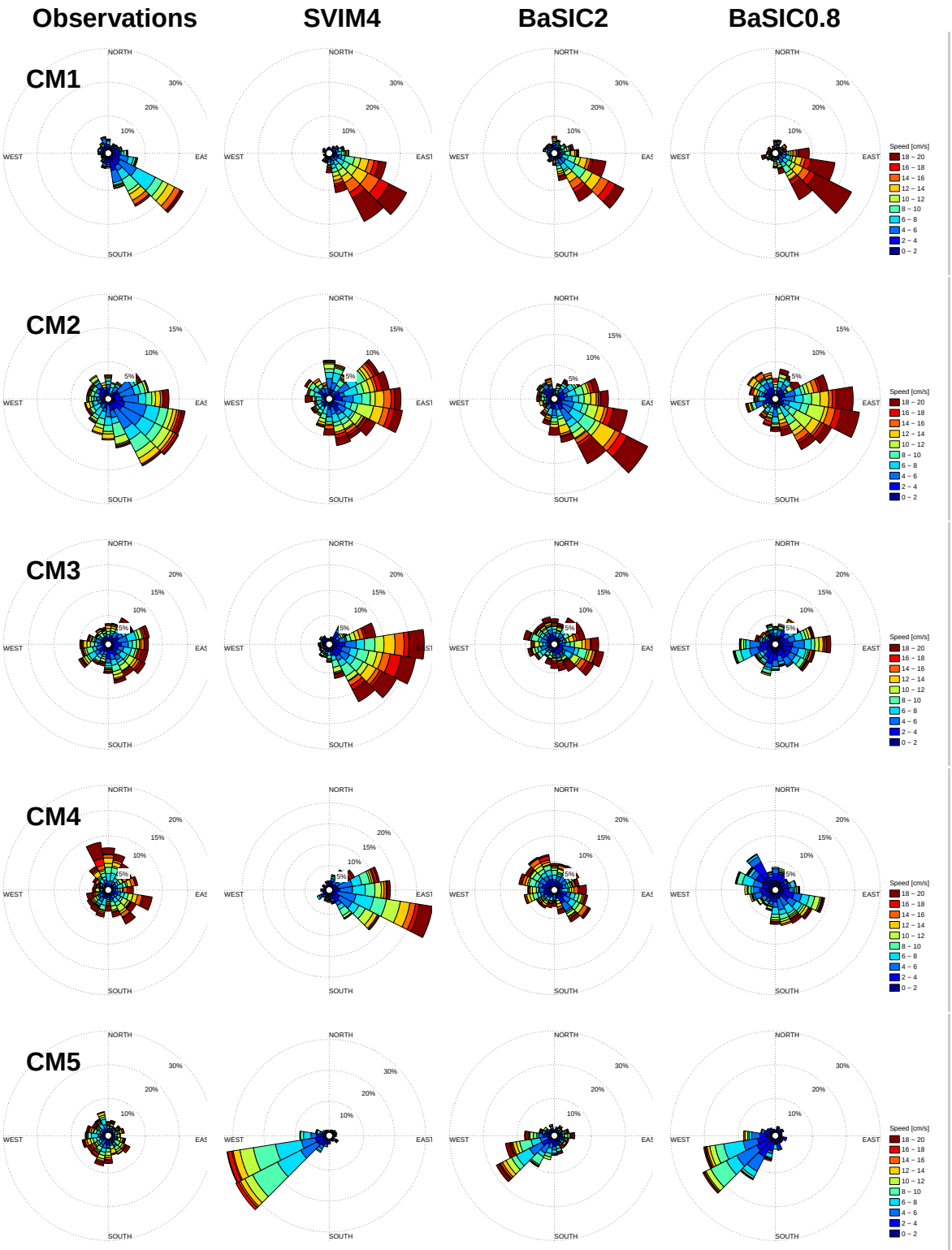

Figure 32: Distribution of current direction together with current speed for the period 2000 - 2001 in the Fugløya-Bjørnøya section at 50m depth at station CM1 through CM5 shown in Figure 31. The first column shows results for the current meter data, second column: SVIM4, third column: BaSIC2 and last column: BaSIC0.8. The color scale indicate current speed in intervals of 2 cms-1, ranging from 0 to 20 cms-1. Dark red color indicates current speeds higher than or equal to 18 cms-1. The direction notation is such that the current is directed towards's the sector, e.g., the observed current at CM1 is dominated by currents toward's southeast.

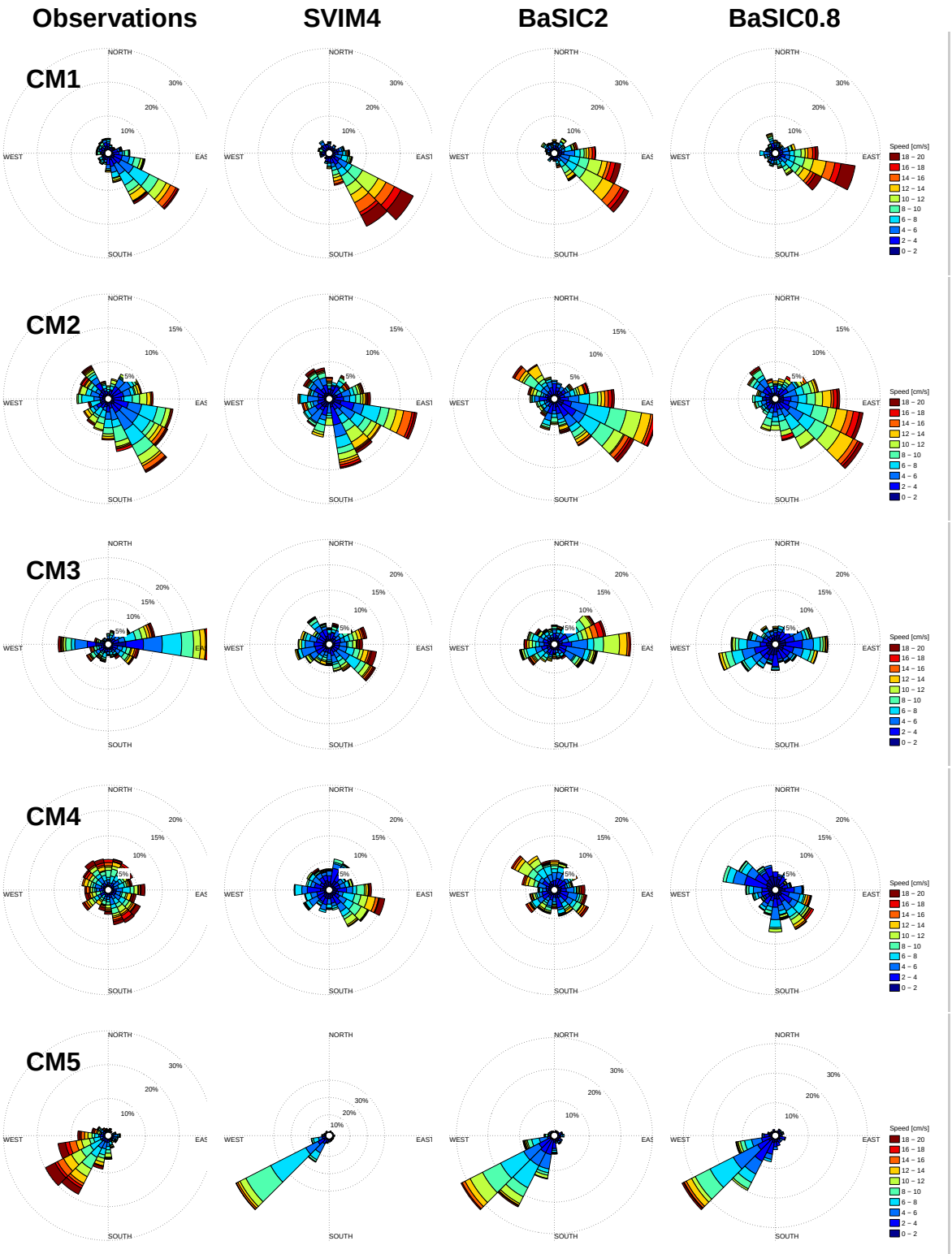

Figure 33: As Figure 32 but for the deepest depth at each station.

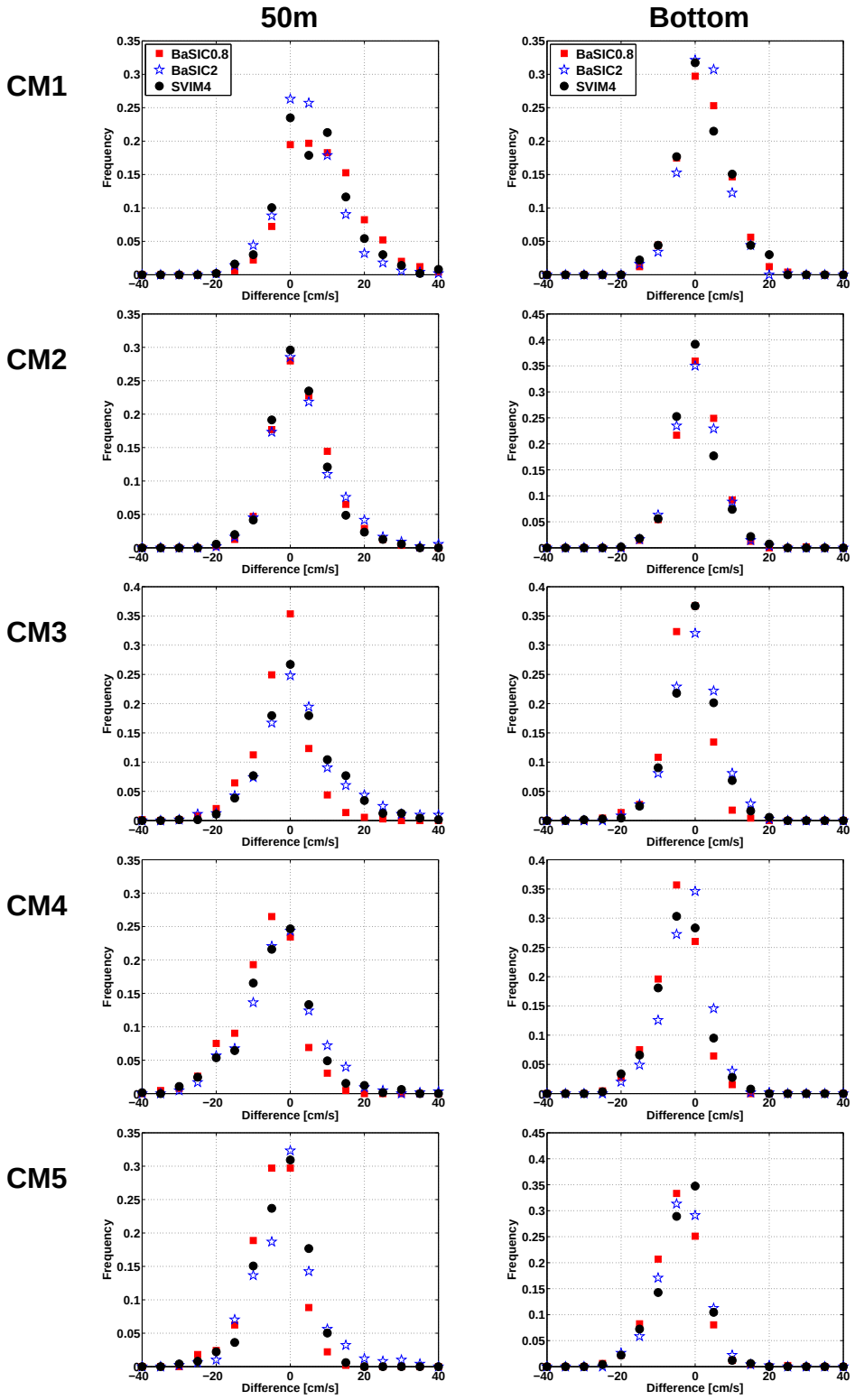

Figure 34: Frequency diagrams of the difference in current speed (in cm/s) between modeled results and observations for the period 2000 - 2001 in the Fugløya-Bjørnøya section at each station (CM1 - CM5). The left column shows results at 50m depth and the right column shows results for the bottom depths. Red squared markers are results from BaSIC0.8, blue stars: BaSIC2 and black circles: SVIM4.

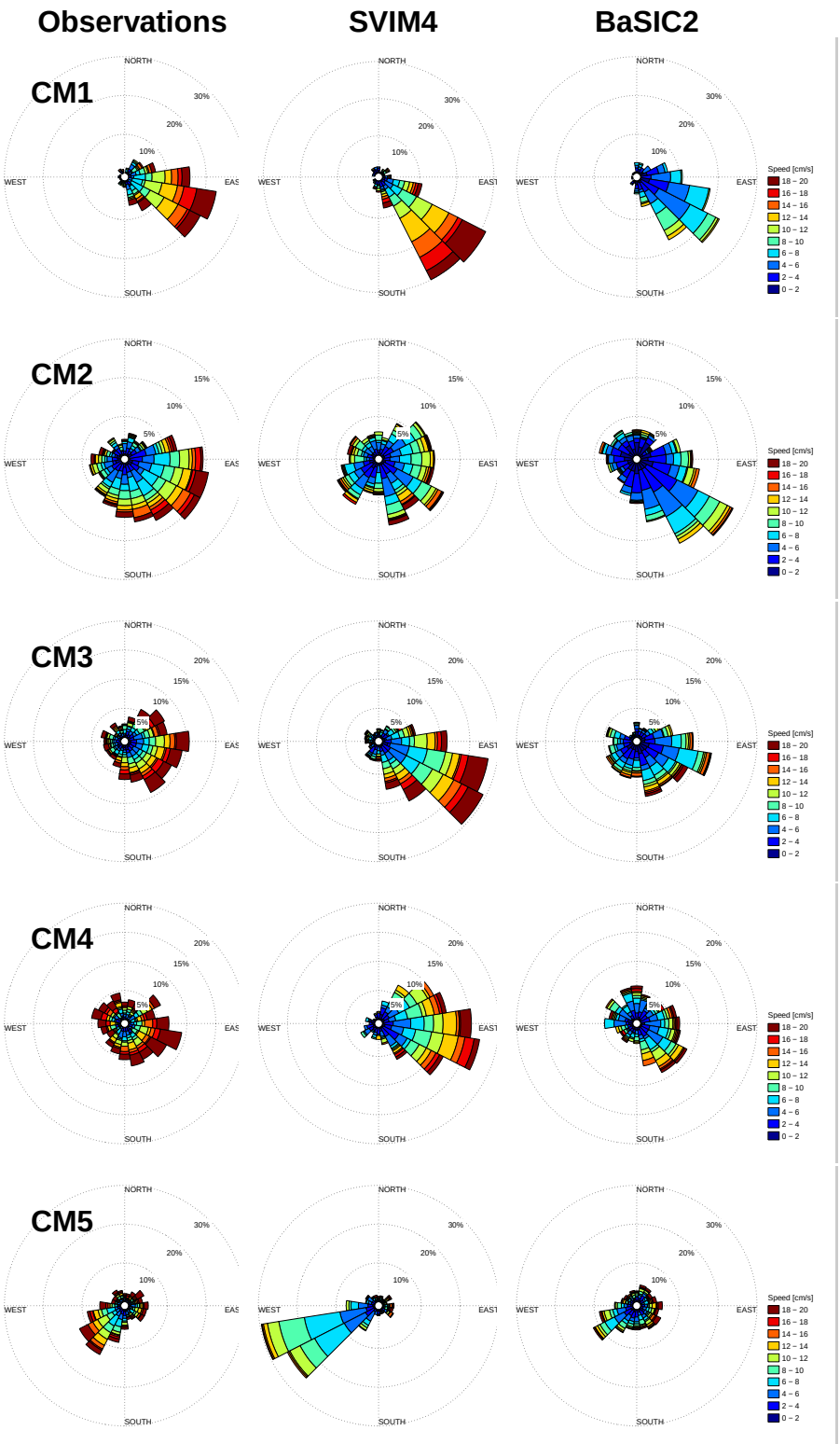

Figure 35: Distribution of current direction together with current speed for the period 2010 to 2011 in the Fugløya-Bjørnøya section at 50m depth at station CM1 through CM5 shown in Figure 31. The first column shows results for the current meter data, second column: SVIM4, and last column: BaSIC2. The color scale indicate current speed in intervals of 2 cms-1, ranging from 0 to 20 cms-1. Dark red color indicates current speeds higher than or equal to 18 cms-1. The direction notation is such that the current is directed towards's the sector, e.g., the observed current at CM1 is dominated by currents toward's southeast.

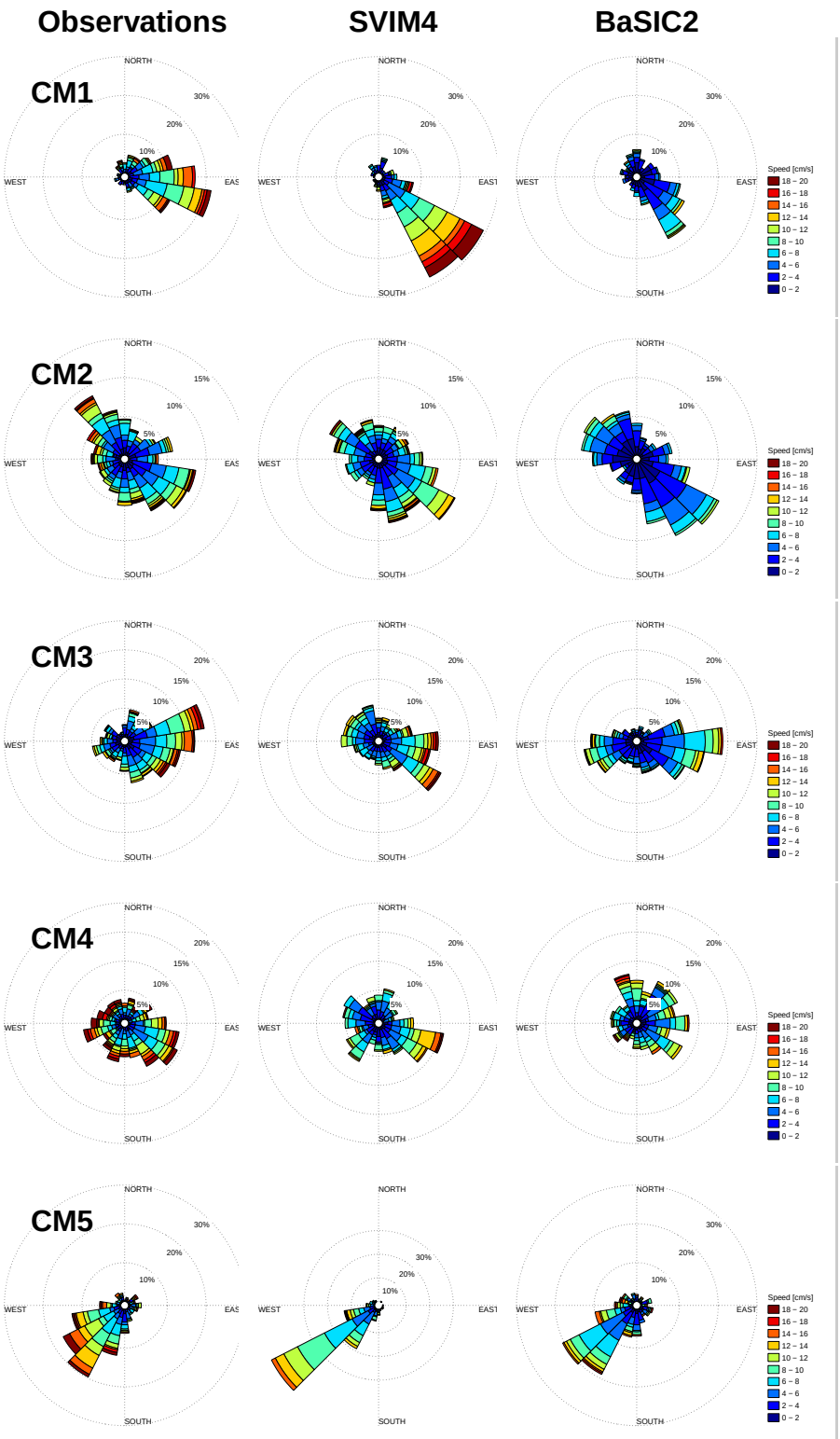

Figure 36: As Figure 35 but for the deepest depth at each station.

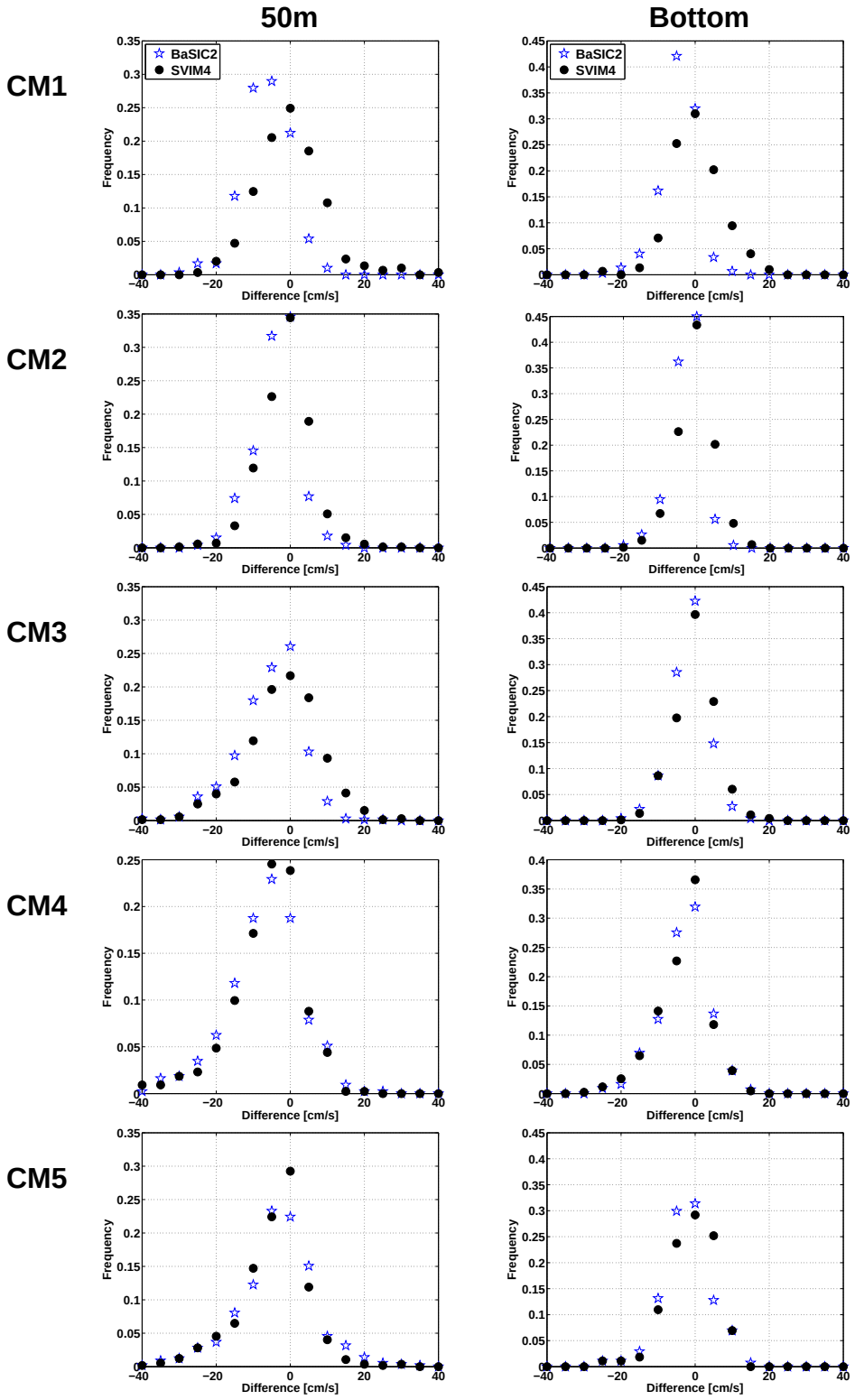

Figure 37: Frequency diagrams of the difference in current speed (in cm/s) between modeled results and observations for the period 2010 - 2011 in the Fugløya-Bjørnøya section at each station (CM1 - CM5). The left column shows results at 50m depth and the right column shows results for the bottom depths. Blue stars are results from BaSIC2 and black circles: SVIM4.

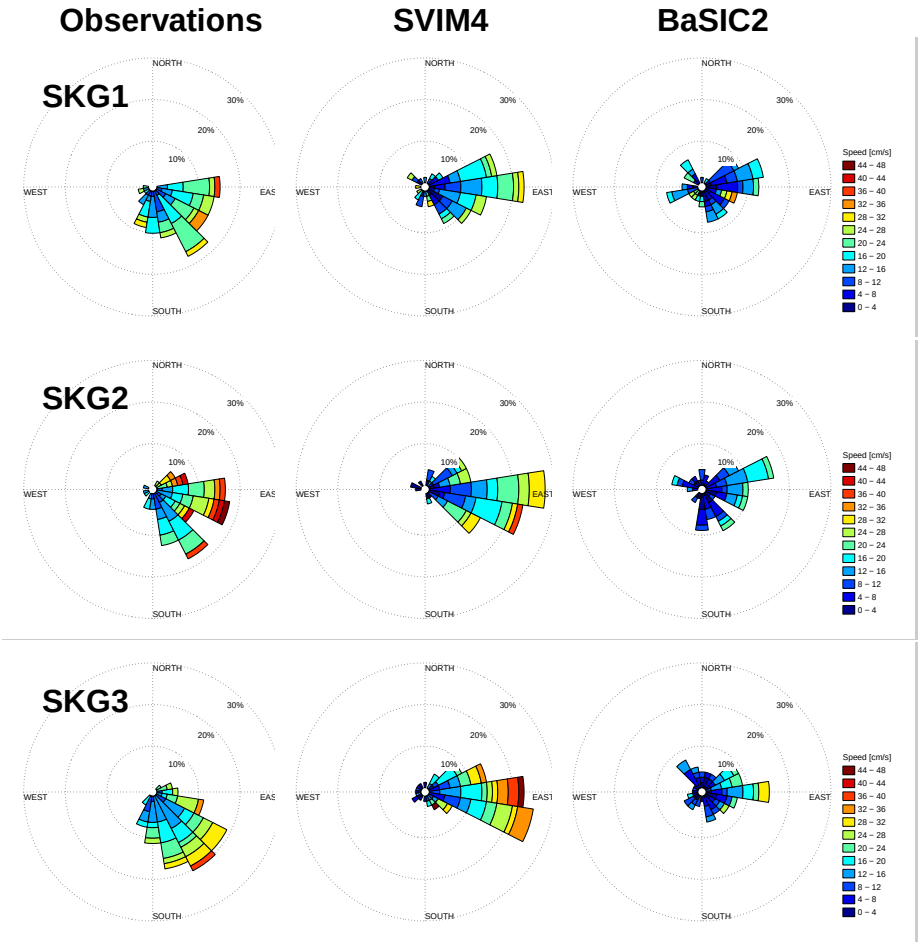

Figure 38: Distribution of current direction together with current speed for the period October,14 2011 to December,31 2011 in three positions (SKG1 - SKG3) at Skrugard at 50m depth shown in Figure 31. The first column shows results for the current meter data, second column: SVIM4 and last column: BaSIC2. The color scale indicate current speed in intervals of 4 cms-1, ranging from 0 to 48 cms-1. Dark red color indicates current speeds higher than or equal to 44 cms-1. The direction notation is such that the current is directed towards's the sector, e.g., the observed current at SKG1 is dominated by currents toward's southeast.

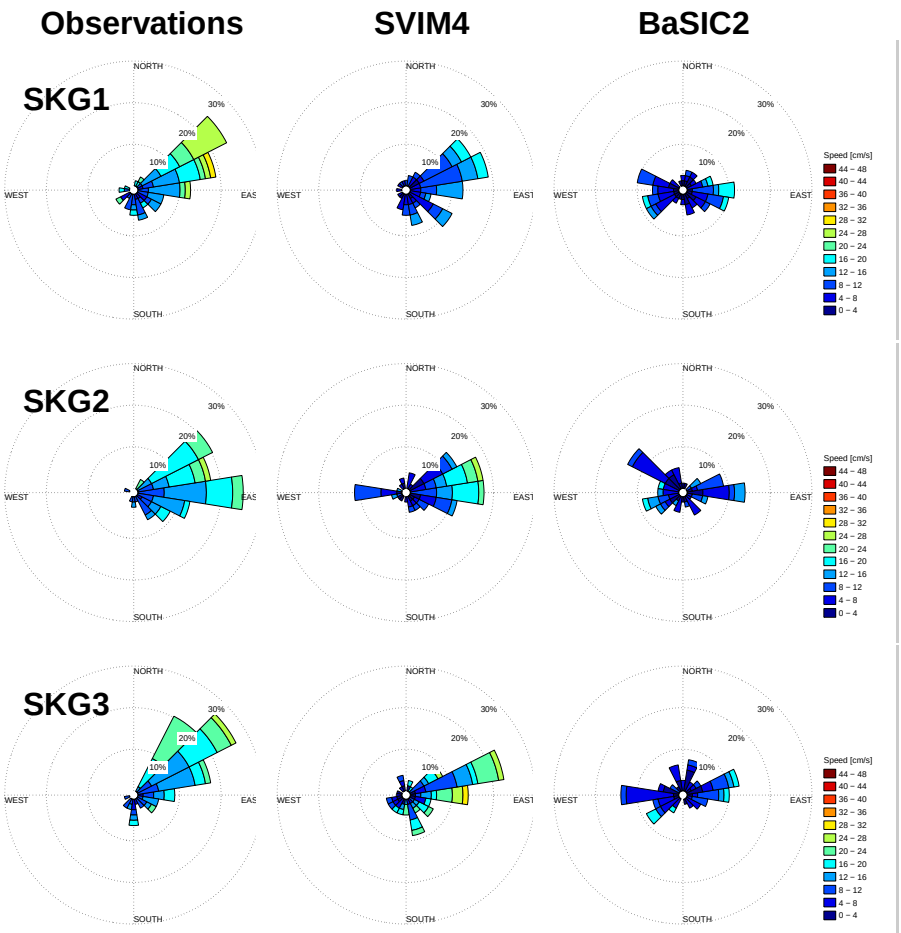

Figure 39: As Figure 38 but for the deepest depth at each station.

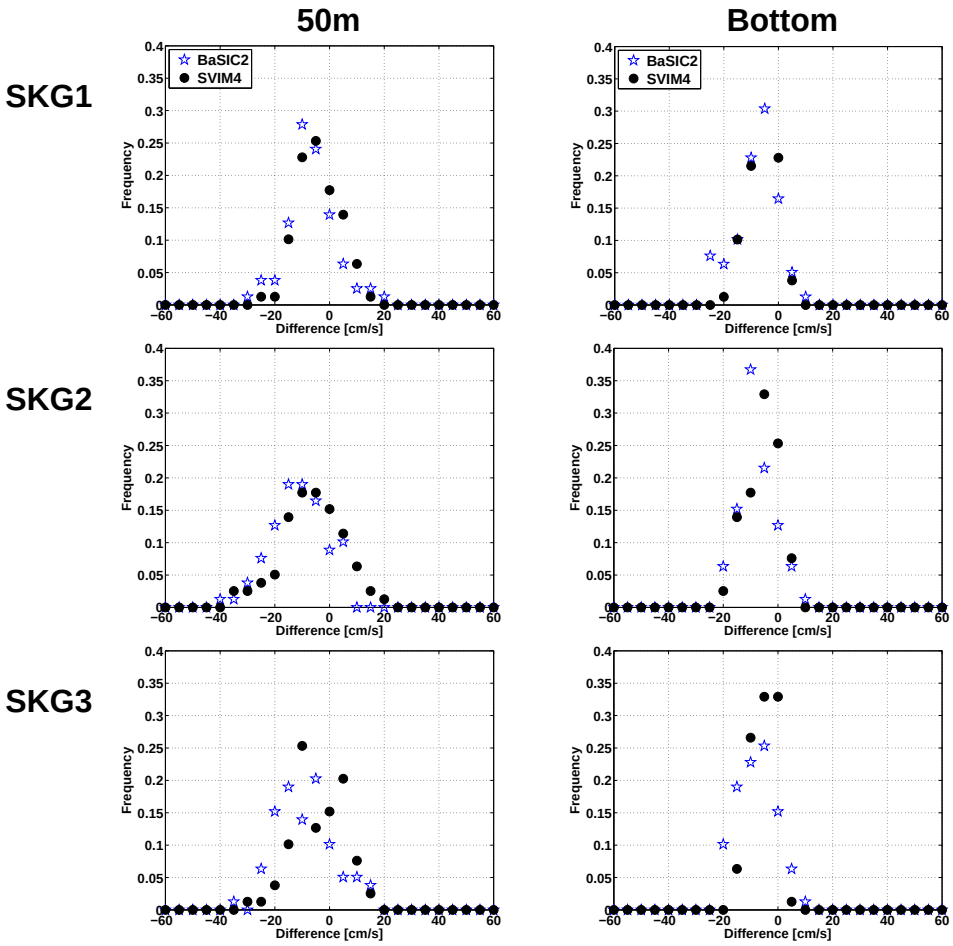

Figure 40: Frequency diagrams of the difference in current speed (in cm/s) between modeled results and observations over the period October, 14 2011 to December,31 2011 at Skrugard at each station (SKG1 - SKG3). The left column shows results at 50m depth and the right column shows results for the bottom depths. Blue are results from BaSIC2 and black circles: SVIM4.

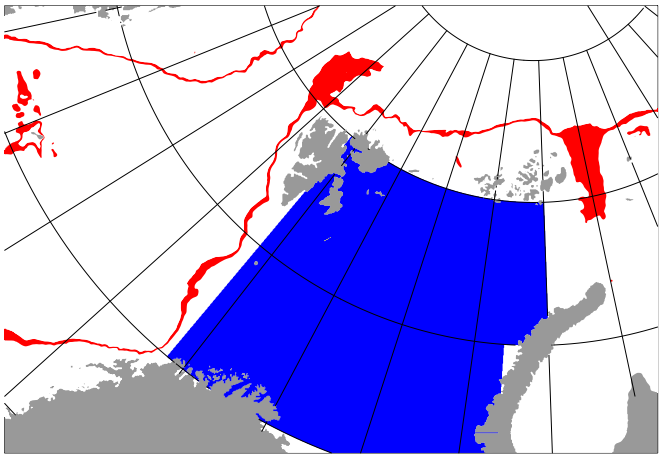

Figure 41: Barents Sea domain. Shown here is the Barents Sea domain (blue), inside the BaSIC2 model domain. The shelf break, displayed in red, is here defined as the region where the bottom depth is between 500 m and 1000 m.

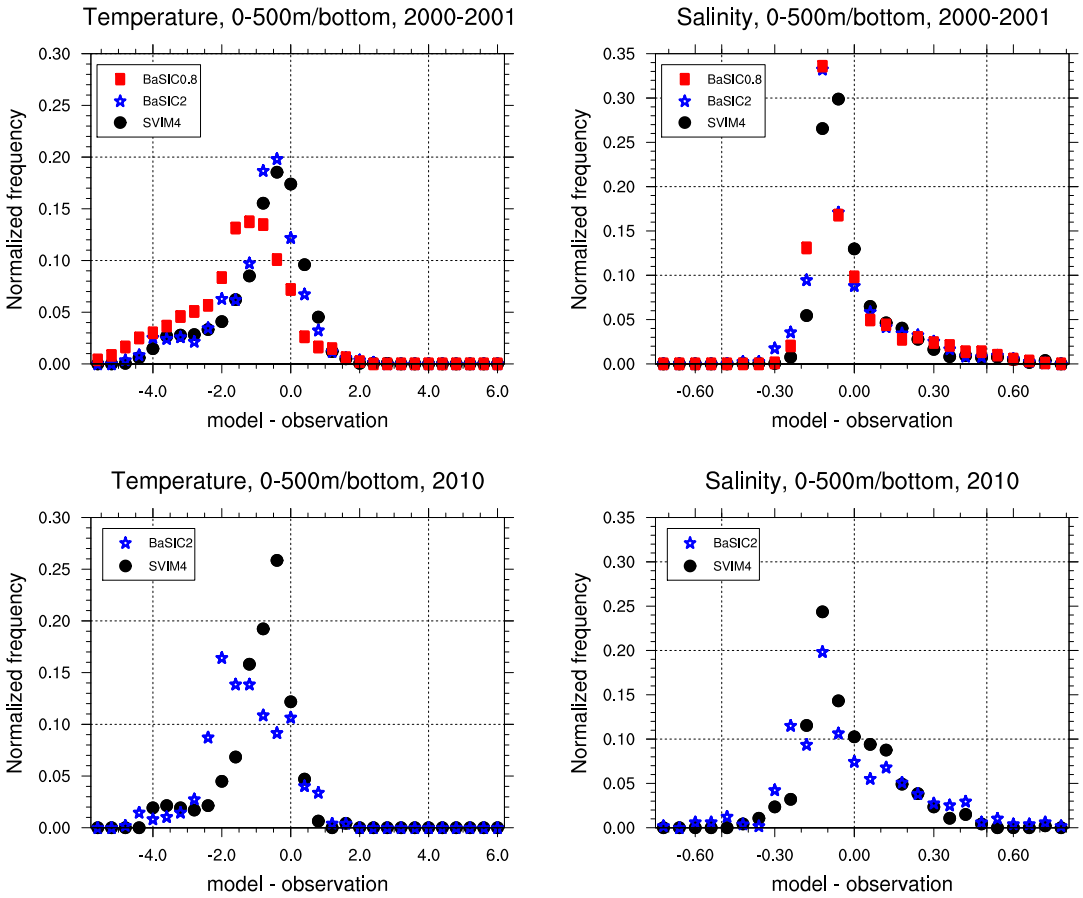

Figure 42: Distribution of differences between model results and observations during 2000-2001 (Standard hindcast, top row) and 2010 (EXP1 hindcast, bottom row), based on vertical means in the upper 500 m (top to bottom in shallower waters). Differences in temperature and salinity in the BaSIC0.8 domain are displayed in the left and right panels, respectively.

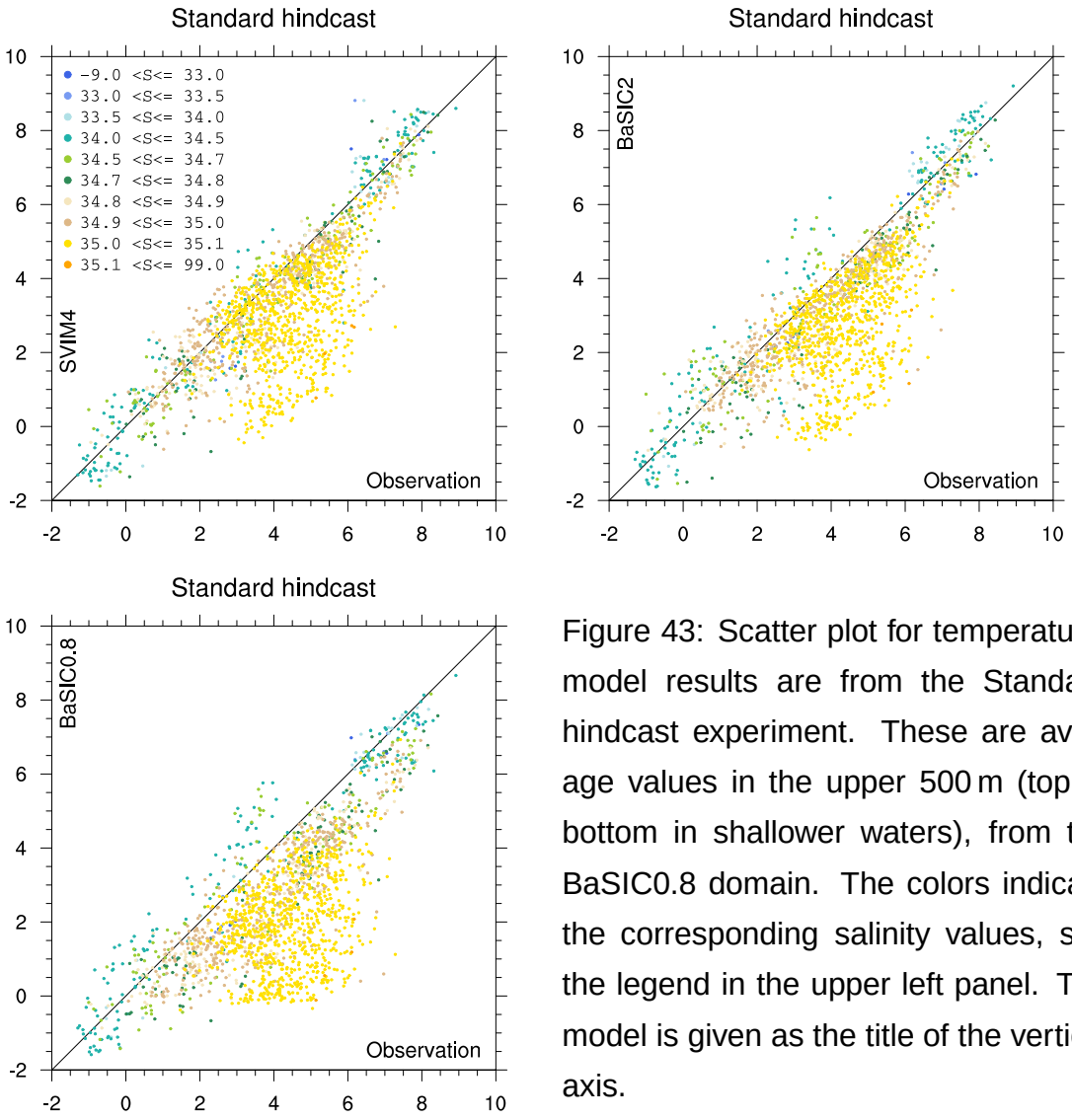

Figure 43: Scatter plot for temperature, model results are from the Standard hindcast experiment. These are average values in the upper 500 m (top to bottom in shallower waters), from the BaSIC0.8 domain. The colors indicate the corresponding salinity values, see the legend in the upper left panel. The model is given as the title of the vertical axis.

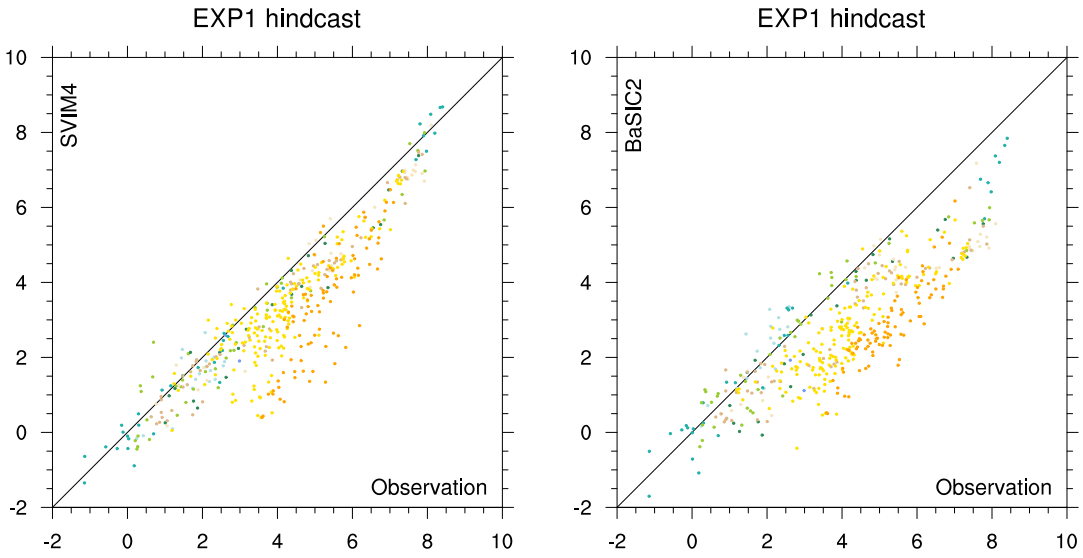

Figure 44: As Figure 43, but for results (EXP1 hindcast) and observations from 2010.

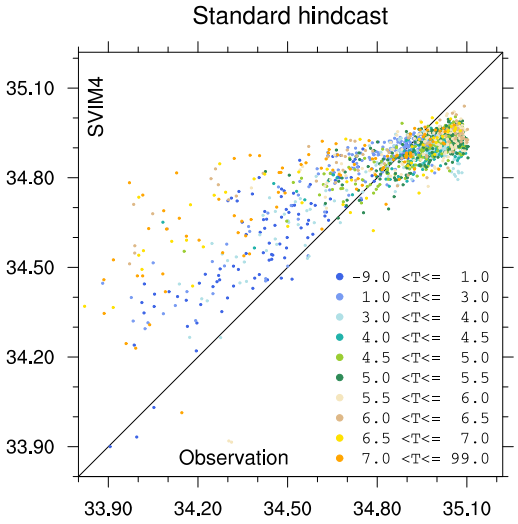

Figure 45: Scatter plot for salinity. These are SVIM4 Standard hindcast average values in the upper 500 m (top to bottom in shallower waters), from the BaSIC0.8 domain. The colors indicate the corresponding temperature values, as shown by the legend.

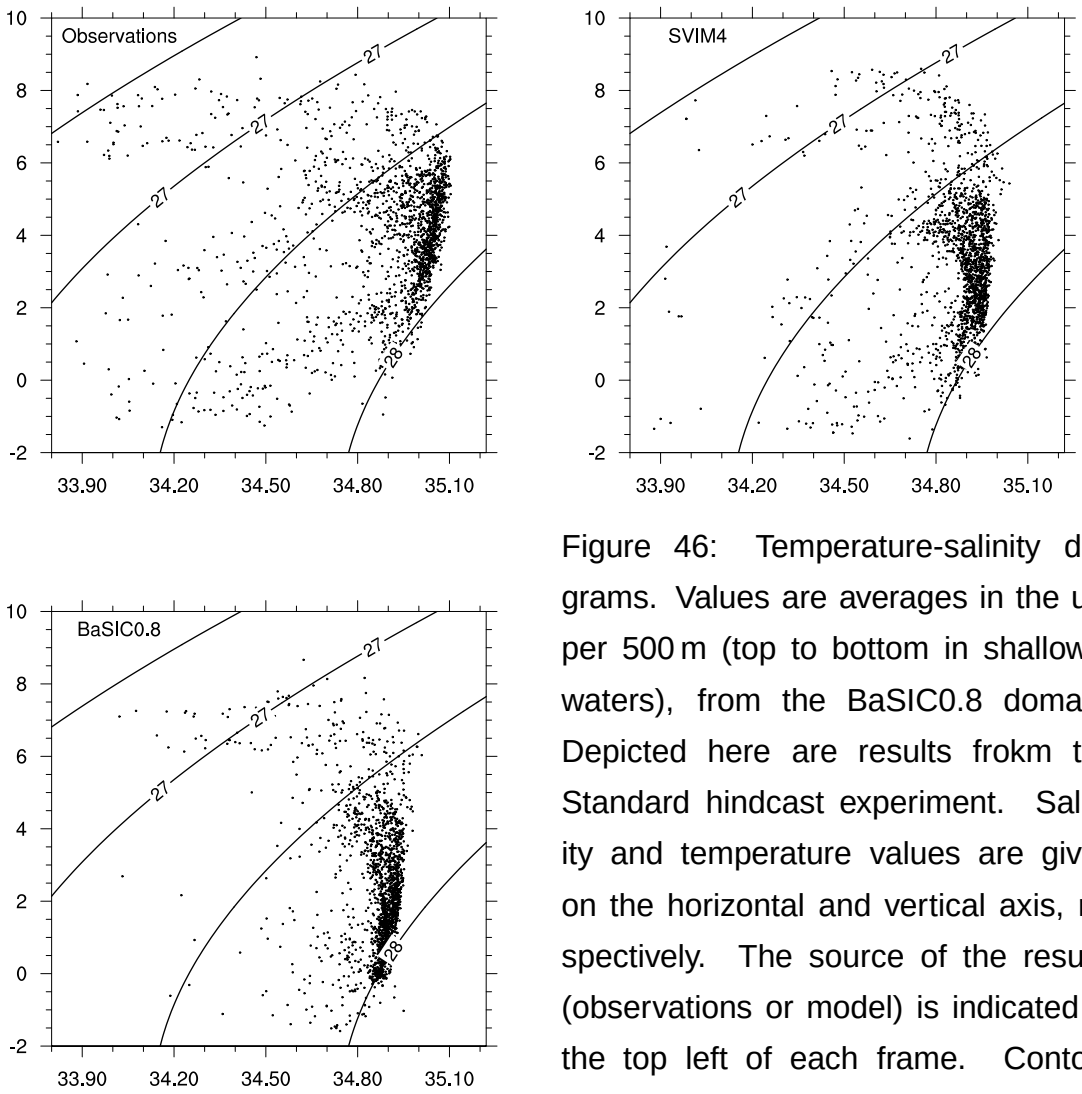

Figure 46: Temperature-salinity diagrams. Values are averages in the upper 500 m (top to bottom in shallower waters), from the BaSIC0.8 domain. Depicted here are results frokm the Standard hindcast experiment. Salinity and temperature values are given on the horizontal and vertical axis, respectively. The source of the results (observations or model) is indicated in the top left of each frame. Contour lines are included for densities $\sigma_0 = 26.5, 27, 27.5, 28\,\mathrm{kg\,m^{-3}}$.

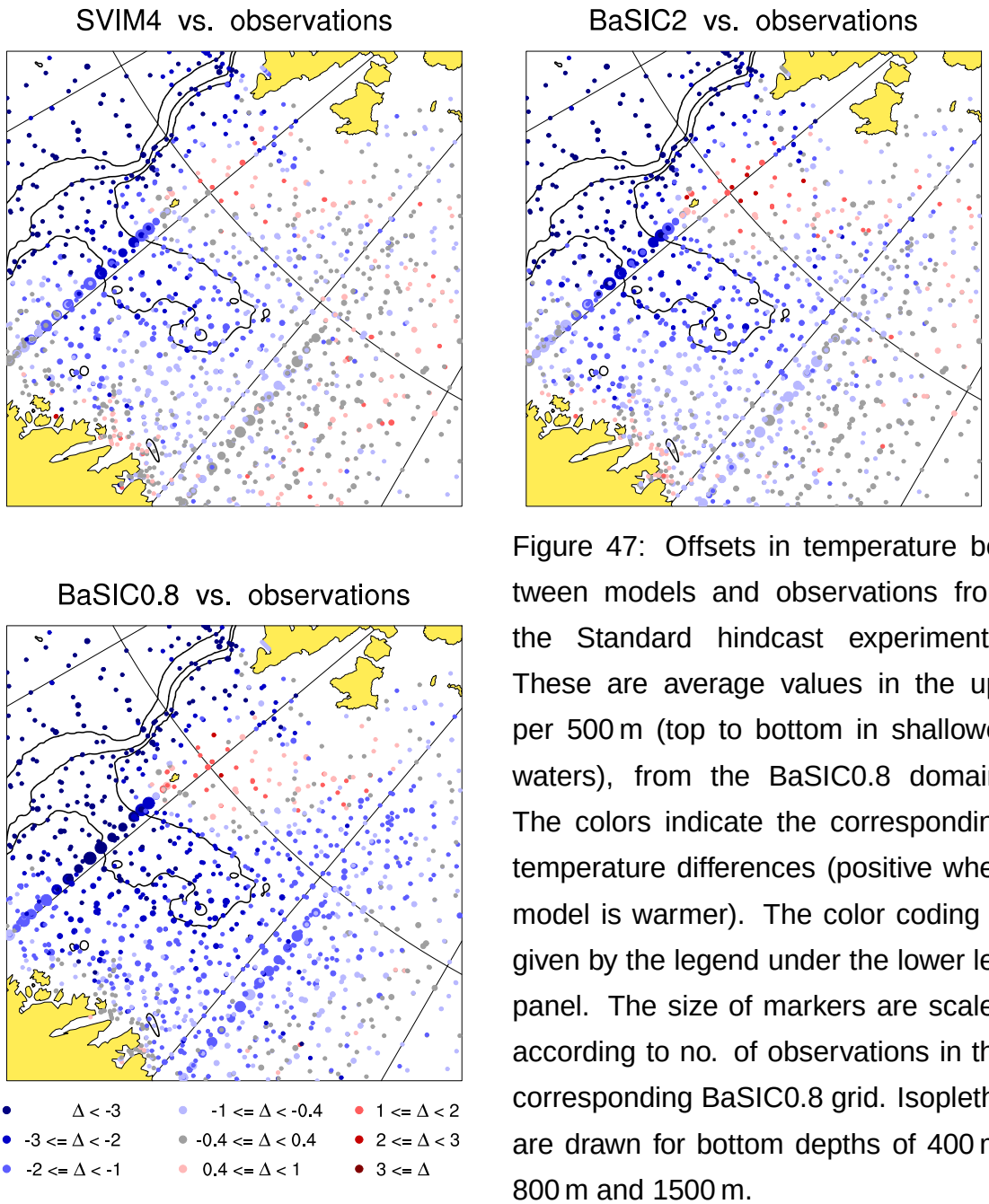

Figure 47: Offsets in temperature between models and observations from the Standard hindcast experiments. These are average values in the upper 500 m (top to bottom in shallower waters), from the BaSIC0.8 domain. The colors indicate the corresponding temperature differences (positive when model is warmer). The color coding is given by the legend under the lower left panel. The size of markers are scaled according to no. of observations in the corresponding BaSIC0.8 grid. Isopleths are drawn for bottom depths of 400 m, 800 m and 1500 m.

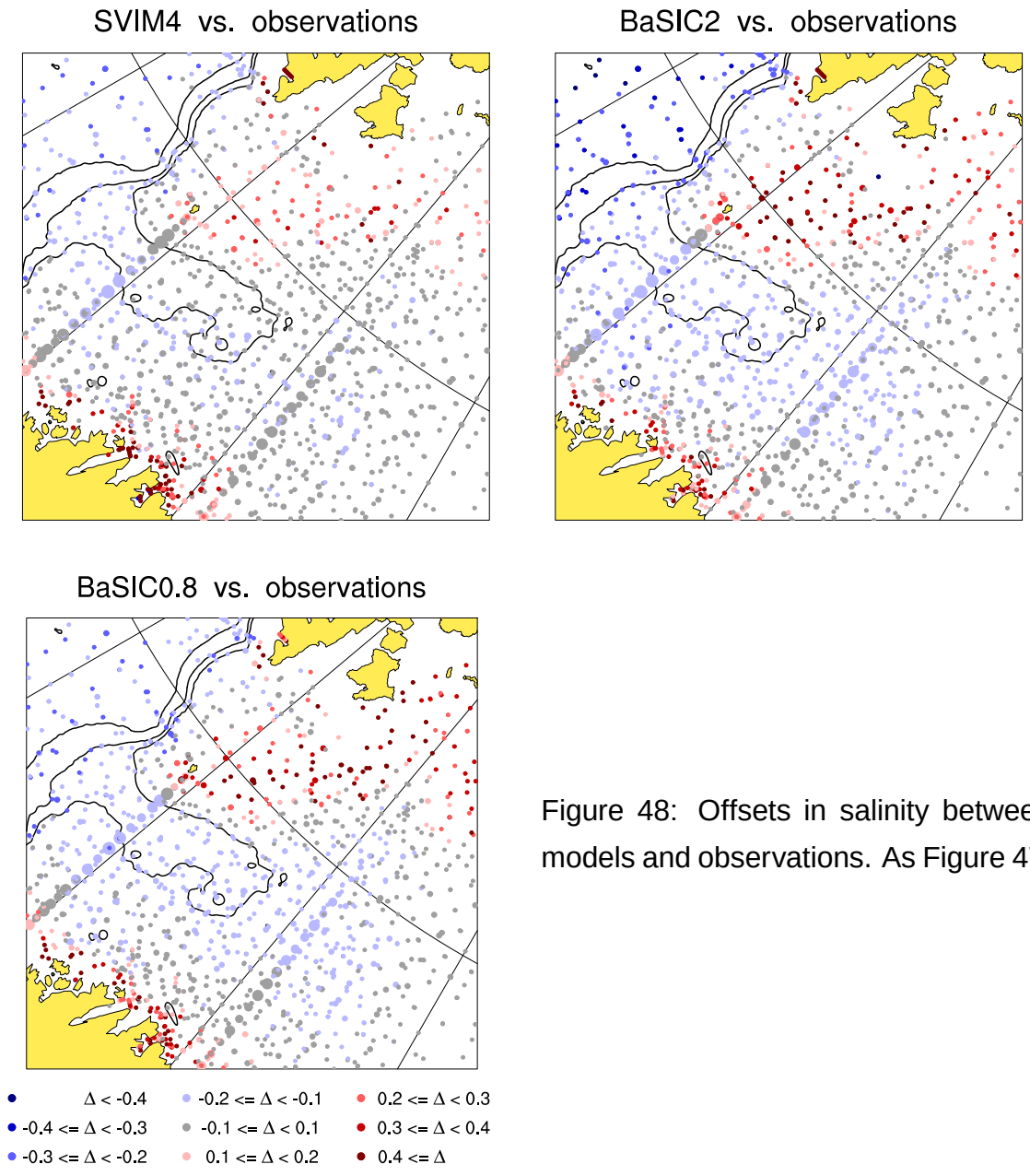

Figure 48: Offsets in salinity between models and observations. As Figure 47.

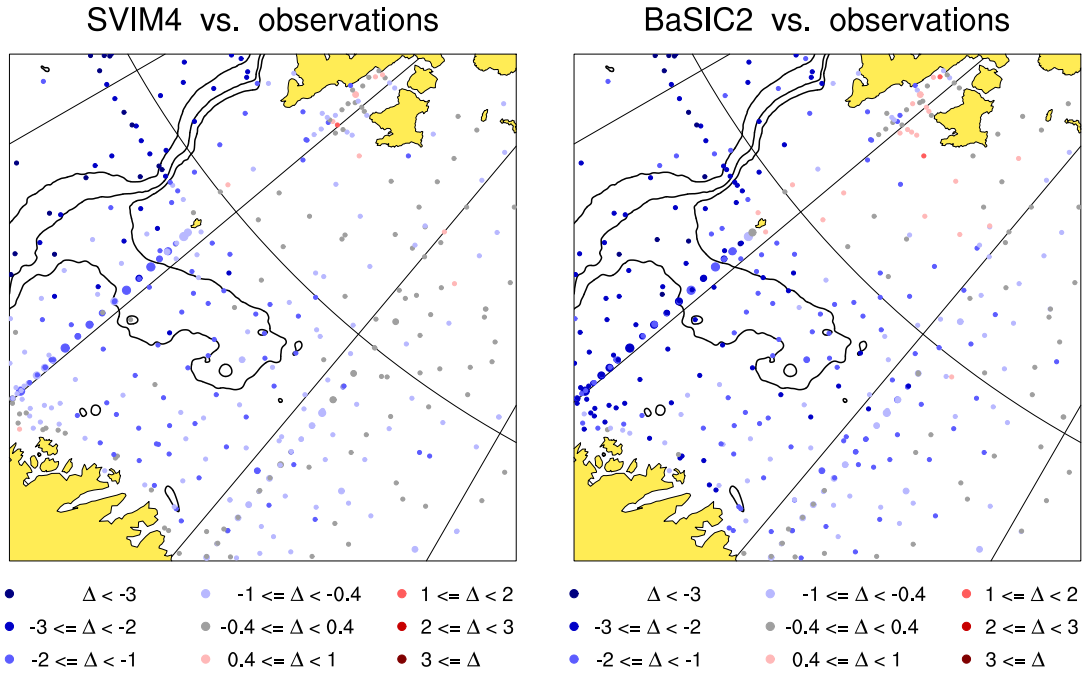

Figure 49: As Figure 47, but for results (EXP1 hindcast) and observations from 2010.

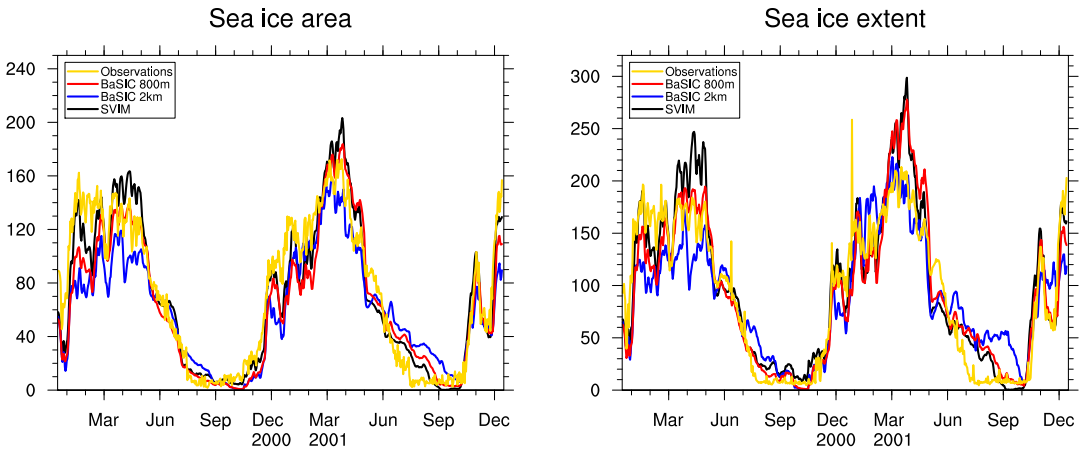

Figure 50: Time series of sea ice area (left panel) and sea ice extent (right panel), in the BaSIC0.8 domain. Areas are given in units of 1000 km^3.